Palmdale South Tangent Slab Built-In Curling and Cracking:

Preliminary Analysis Report

Draft Report Prepared for the California Department of Transportation

by:

Shreenath Rao and Jeff Roesler

University of Illinois
Urbana, IL 61801

Pavement Research Center
Institute of Transportation Studies
University of California Berkeley
University of California Davis

May 2004

TABLE OF CONTENTS

LIST OF FIGURES

LIST OF TABLES

1.0 INTRODUCTION

This report presents a preliminary analysis of slab cracking at the South Tangent sections tested at Palmdale, California using the Heavy Vehicle Simulator (HVS). The data collected on the South Tangent include corner and edge deflections, thermocouple data representing temperature distribution through the slabs, visual and photographic crack surveys, crack activity measurement data, multi-depth deflection data representing deflections at various depths beneath the pavement surface, slab strains measured at critical locations using strain gages, and falling weight deflectometer (FWD) data.

The primary focus of this report is the preliminary cracking analysis of the South Tangent slabs. The chief tool used in this analysis is the finite element program, ISLAB2000, which is used to estimate pavement responses for a given geometry under the influence of wheel loadings and layer temperature profiles. The key data used in the analysis include measured corner deflections, thermocouple data, and visual crack survey information along with geometry (slab dimensions) and layer information including FWD backcalculated elastic moduli and modulus of subgrade reaction, coring data, and laboratory measured flexural strength and thermal expansion data. The analysis focuses on the following objectives:

- Estimate an effective linear built-in temperature difference (EBITD) in the slab to simulate the effects of moisture shrinkage and construction temperature gradients.
- Calculate responses including deflections and stresses at critical locations at the top and bottom of the slab. The responses of the slab are significantly affected by moisture shrinkage and construction temperature gradients.
- Evaluate slab cracking by attempting to understand the stress state of the slab.

Note that the analyses of other collected data (such as crack activity measurements, multi-depth deflection data, and edge deflection data) are not included in this report. These data will be used in the development of the final comprehensive cracking and joint deterioration model following the analysis of the North Tangent sections.

1.1 Background

As part of the California Department of Transportation (Caltrans) Long Life Pavement Rehabilitation Strategies (LLPRS), a high early strength hydraulic cement was field tested using an HVS, shown in Figure 1. This fast-setting hydraulic cement concrete (FSHCC) is designed to gain enough strength to allow it to be opened to traffic within 4 hours of placement. The objective of the HVS tests was to evaluate the performance of this concrete under the influence of full-scale loads. The results of the field tests are expected to be utilized both in the assessment of the use of FSHCC and in the development of a mechanistic-empirical design procedure for

Figure 1. HVS with temperature control chamber at the Palmdale test sections.

California pavements. The details of the proposed evaluation plan were outlined in the *Test Plan for CAL/APT Goal LLPRS - Rigid Phase III* (*1*).

Two full-scale test pavements were constructed on State Route 14 approximately 5 miles south of Palmdale, California. One test pavement was located on the shoulder of northbound SR14 (North Tangent) and another on the shoulder of southbound SR14 (South Tangent), each approximately 210 m in length. The materials used consisted of an 80/20 blend of Ultimax® and Type II PCC. Various test sections, consisting of combinations of concrete slab thickness (100, 150, and 200 mm), tied concrete shoulders, doweled transverse joints, and widened lanes, were constructed and evaluated using the HVS over a 2-year period.

The main objective South Tangent tests was the evaluation of the fatigue behavior of 100-, 150-, and 200-mm thick FSHCC on an aggregate base under the influence of bi-directional wheel loads, dry conditions, and a temperature control box around the tested area (not used on all sections). This report is a preliminary analysis of the South Tangent test sections. A subsequent report includes in-depth analysis of fatigue for both the North and South Tangent sections, and incorporates the analysis presented herein as well as the analysis presented in Reference (*2*).

1.2 Section Layout and Details

The South Tangent includes three test sections of 100-, 150-, and 200-mm nominal thickness concrete. None of the pavement structures on the South Tangent had dowel bars, tie bars, or widened lanes. The slab widths were 3.7 m with joint spacing varying between 3.7 m and 5.8 m. All the test sections in the South Tangent had 150-mm thick Class 2 aggregate base resting on a compacted granular subgrade and perpendicular transverse joints. Figure 2 shows the pavement structure diagram for the South Tangent sections. Details of the layout and material descriptions of the Palmdale test sections are included in Reference (*3*).

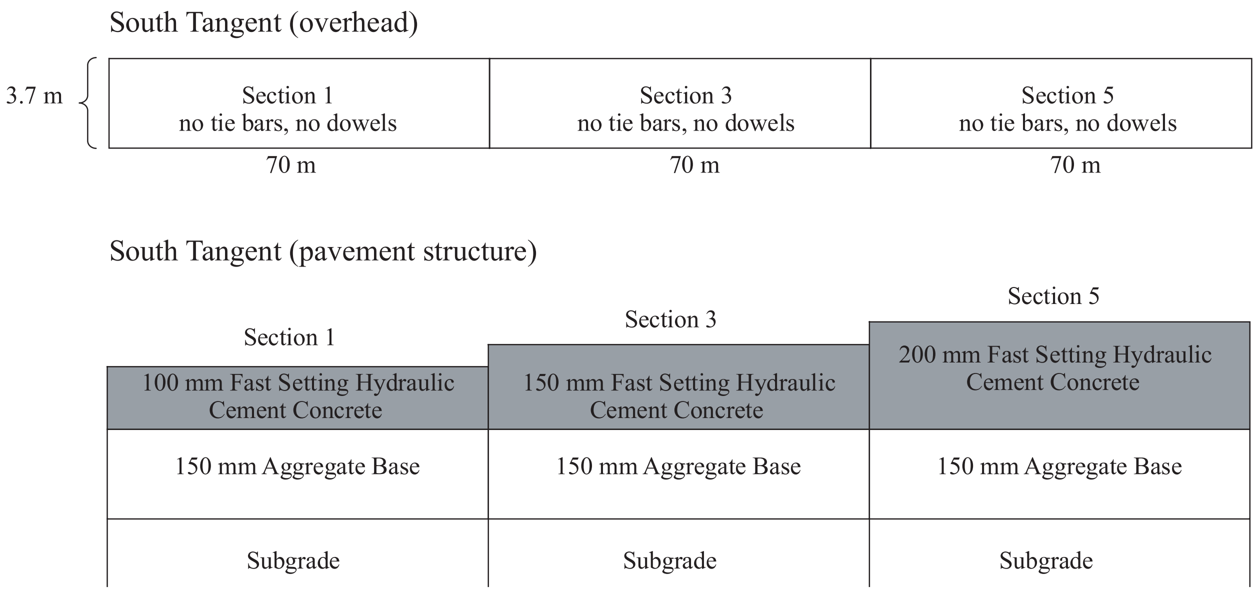

Figure 2. South Tangent pavement structure diagram.

2.0 TESTING, DATA COLLECTION, LOADING, AND INSTRUMENTATION PLANS

All dynamic data were collected while running the HVS wheel at creep speed (2 km per hour) in both directions along the test carriage. For fatigue analysis purposes, the appearance of a crack on the middle slab signified fatigue failure. Cracking on either of the two adjacent slabs was not considered failure due to the HVS wheeling changing direction on those sections, and it is established practice to ignore pavement behavior in the HVS "turnaround zones."

The HVS tests were run beyond the development of a crack in the middle slab in order to observe the performance of the slabs after the initial crack. The details of the testing, data collection, loading, and instrumentation plan, as well as post-testing forensic evaluation, materials testing, and first level analysis are included in Reference (*4*).

2.1 HVS Loading Plan

The thickness of the slab varied over the lengths of the various sections [see Reference (*4*) for details]. Due to these variations, some changes in the loading pattern were made from test to test. The actual loading pattern is shown in Tables 1, 2, and 3. Trafficking was done in the "channelized" bi-directional traffic mode in which the HVS outer wheel ran along the edge of the concrete slabs with the full load on the slabs and without side-to-side wheel wander. Wander was not introduced since it would have prolonged the time required to achieve fatigue cracking on each test section.

2.2 HVS Instrumentation Plan

In order to monitor the functional and structural behavior of the pavement under accelerated loading, various instruments were used. The instrumentation plan is summarized

Table 1 Loading Plan for HVS Tests 519FD to 521FD (100 mm Nominal Thickness)

Traffic Load (kN)	HVS Repetitions on Section		
	Section 519FD	Section 520FD	Section 521FD
20			0 – 157,719
25	0 – 55,448		
35		0 – 51,290	
50	55,448 – 56,432		
80			157,719 – 168,319
100	56,432 – 60,163	51,290 – 74,320	

*Test 522FD was a static test.

Table 2 Loading Plan for HVS Tests 523FD to 527FD (150 mm Nominal Thickness)

Traffic Load (kN)	HVS Repetitions on Section				
	Section 523FD	Section 524FD	Section 525FD	Section 526FD	Section 527FD
35					0 – 723,438
40					723,438 – 1,233,969
45	0 – 151,151	0 – 119,784	0 – 5,000		
85				0 – 23,625	

Table 3 Loading Plan for HVS Tests 528FD to 531FD (200 mm Nominal Thickness)

Traffic Load (kN)	HVS Repetitions on Section			
	Section 528FD	Section 529FD	Section 530FD	Section 531FD
40	0 – 83,045	0 – 88,110	0 – 64,227	0 – 31,318
60		88,110 – 352,324	64,227 – 816,675	
70				31,318 – 65,315
90			816,675 – 846,845	

below for the instruments used in this analysis. Complete details of the various instruments, their recording mechanisms and outputs, are included in References (*3, 4*).

On each test section, two Joint Deflection Measuring Devices (JDMD) and one Edge Deflection Measuring Device (EDMD) were installed to record the surface deflections at the corners of adjacent slabs and at the middle edge of the test slab. A typical installation is shown in Figure 3. Surface deflections were also captured with the Road Surface Deflectometer (RSD) on certain sections. These results were used only for calibration purposes between the RSD, JDMDs and EDMDs.

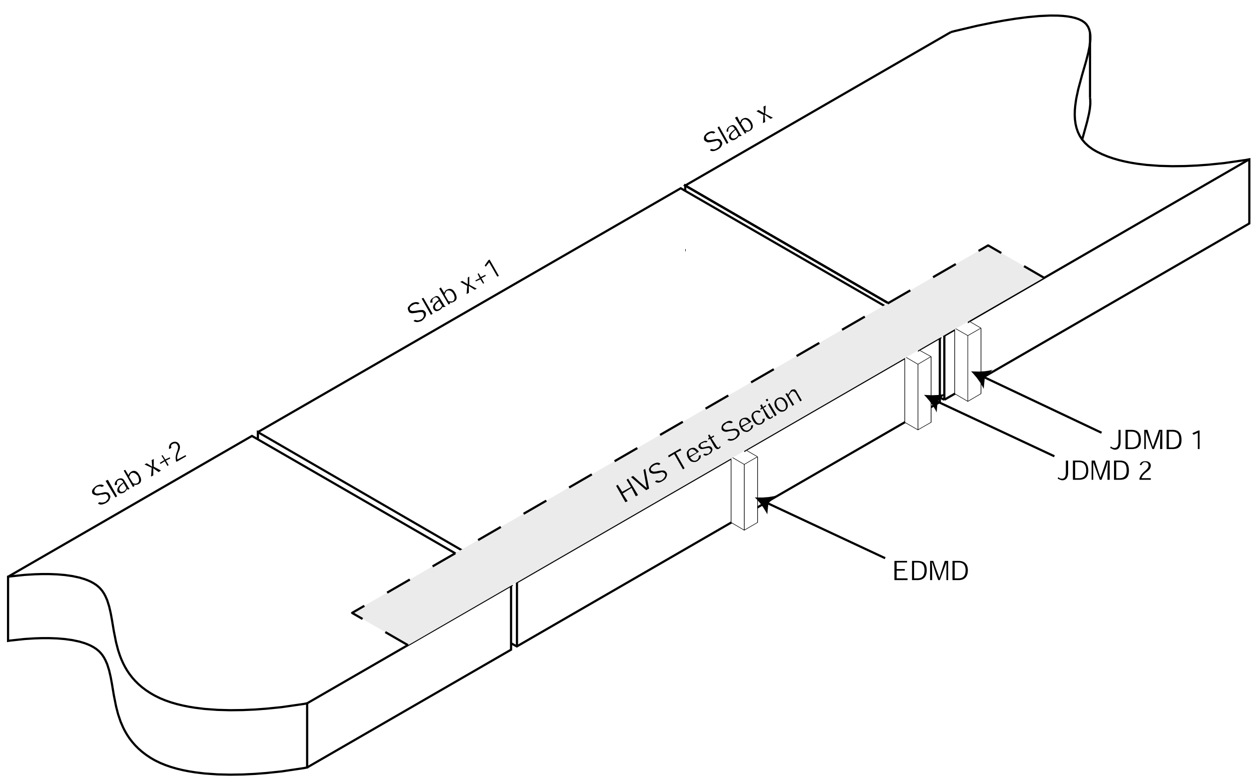

Figure 3. Illustration of the placement of the JDMDs and EDMD.

Test sections were also instrumented with thermocouples, which recorded the surface (0 mm) as well as the temperatures at 50-mm intervals at depth to the bottom of the slab:

Slab thickness:	Thermocouples Located at:
100 mm	Surface (0 mm), 50 mm, 100 mm
150 mm	Surface (0 mm), 50 mm, 100 mm, 150 mm
200 mm	Surface (0 mm), 50 mm, 100 mm, 150 mm, 200 mm

Other environmental data, such as rainfall, wind direction, and wind speed were continuously recorded using a Davis automatic weather station. Environmental data for all test sections on the South Tangent are included in Reference (*4*).

3.0 FIRST LEVEL DATA ANALYSIS

The performances of the different sections have to be evaluated in the context of their relative properties such as slab dimensions (joint spacing and thicknesses) and material properties (layer moduli, FSHCC strength, modulus of subgrade reaction). In addition, the loading conditions varied from one section to another. Details of section performances, deflection data, forensic evaluation, and first level data analysis are included in Reference (*4*). For the first level analysis of data, the sections are placed into three groups – 100-mm nominal slab thickness sections, 150-mm nominal slab thickness sections, and 200-mm nominal slab thickness sections.

3.1 Slab Dimensions

Joint spacing and slab thicknesses for the South Tangent pavement test sections are summarized in Table 4. For analysis purposes and for a full understanding of section performance, dimensions of the adjacent slabs are also required and are included in the table. All of the slabs tested on the South Tangent were 3.66 m wide.

Four cores from each of the three slab thickness groups were taken to verify the thicknesses. The core was taken about 1 m from the non-loaded slab edge. Details of the coring are included in References (*3, 4*). The measured core thicknesses varied greatly from the target thicknesses. The average core thicknesses were between 7.3 and 13.0 percent greater than the design thicknesses. The coefficients of variation (COV) ranged from 6.5 percent to 17.2 percent, with higher COVs for the 100-mm and 150-mm nominal thickness sections. It should be noted that cores were not taken on all of the loaded test slabs and significant slab thickness variability can exist between slabs and even within the same slab. The cores were also used to measure the average slab density.

Table 4 Joint Spacing and Slab Thickness Summary for South Tangent Pavement Sections

HVS Test Section	Center Test Slab Number	Thickness Information (mm)	Joint Spacing (m)	Adjacent Slabs Joint Spacings (m)	
519FD	4	Nominal: 100.0 Mean: 107.3 Std. Dev.: 18.4 COV: 17.2%	5.80	5.41	3.96
520FD	8		5.77	5.46	4.02
521FD	12		5.76	5.50	3.78
522FD	14		3.69	3.99	5.50
523FD	17	Nominal: 150.0 Mean: 163.0 Std. Dev.: 27.6 COV: 17.0%	5.47	3.62	5.81
524FD	20		5.77	5.55	3.97
525FD	23		3.91	5.77	3.58
526FD	27		4.00	5.79	3.54
527FD	22		3.58	3.91	5.55
528FD	35	Nominal: 200.0 Mean: 211.4 Std. Dev.: 13.8 COV: 6.5%	4.03	5.70	3.59
529FD	31		3.94	5.84	3.65
530FD	39		3.95	5.77	3.66
531FD	42		3.70	3.92	5.39

3.2 FSHCC Flexural Strength

The FSHCC used for the Palmdale test site construction was an 80/20 blend of Ultimax® and Type II PCC. The consistency of the concrete mix varied considerably from one truck to another. Many of the mixes arriving at the site were fairly inconsistent and often required the addition of water. Each of the three nominal thickness groups required approximately 10 truckloads of concrete. Two of these trucks were selected at random to cast beams for 8-hour, 7-day, and 90-day flexural strength tests. Two beams were tested at each of these ages for each of the two randomly selected truckloads. The details of the early flexural strengths for all of the sections are included in Reference (*3*). The long term flexural strength data is included in Reference (*4*).

The average flexural strength increased over 90 percent from the 8-hour to the 7-day test. From day 7 to day 90, average flexural strength gain was 30 percent. The variability in the 90-day flexural strength for the South Tangent sections ranged from 11 to 22 percent. However, much of the variation in test sections was due to the variation in strengths between beams taken from two separate trucks.(*3*) Since several different truckloads were used for each of the three nominal thickness groups, and only two trucks were tested for flexural strength, it is not possible to ascertain the flexural strength characteristics for each section on an individual basis. Because the variation in strength between trucks is higher than (or of the order of) the variation in strength between sections of different nominal thicknesses, the average flexural strength value representative of all South Tangent test sections is used in the analysis. The average flexural strength of the beam specimens tested is summarized in Table 5.

The strength gain curve based on the average for all South Tangent sections is shown in Figure 4. This strength gain curve is used to estimate the expected average strength for the South Tangent sections at the time of HVS testing based on age during testing.

A strength gain model developed using the average laboratory flexural strength data is shown in Equation 1.

$$FSHCC\ Flexural\ Strength\,(MPa) = 0.075A^3 - 0.2562A^2 + 1.4812A + 2.8582 \qquad \textbf{(1)}$$

where
A = Log(Age since construction, days)

Based on the strength gain model, the estimated expected flexural strength for each of the South Tangent test sections is shown in Table 6. For simplicity of analysis, because of the high variability in FSHCC strength between different truckloads relative to the effect of average

Table 5 Average Flexural Strengths for South Tangent Sections

Nominal Thickness (mm)	8 hours		
	Mean (MPa)	**Std. Dev. (MPa)**	**COV (%)**
100	1.87	0.14	7
150	1.92	0.60	31
200	2.45	0.16	7
All Sections	*2.08*	*0.39*	*19*
	7 Days		
100	3.48	3.48	3.48
150	3.86	3.86	3.86
200	4.48	4.48	4.48
All Sections	*3.94*	*3.94*	*3.94*
	90 days		
100	4.34	0.50	11
150	4.92	1.10	22
200	5.31	0.97	18
All Sections	*4.85*	*0.90*	*19*
	575 days (North Tangent)		
All Sections (200 mm)	*5.18*	*0.25*	*5*

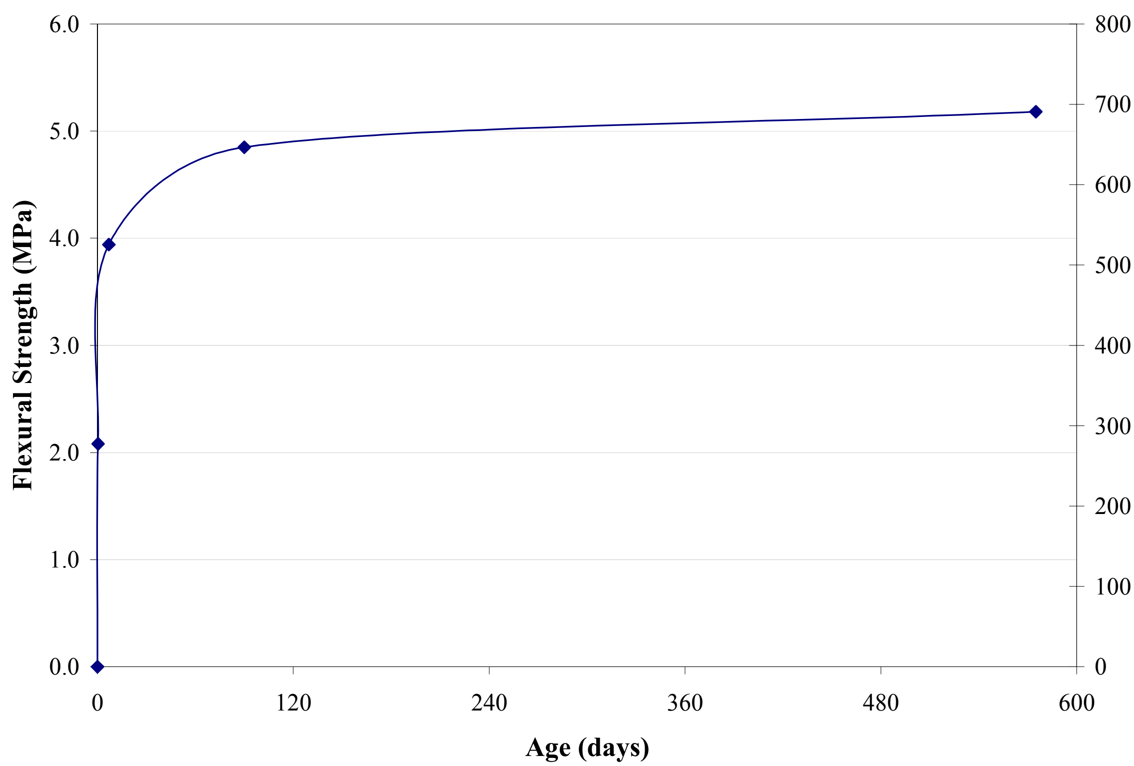

Figure 4. Average flexural strength gain curve for South Tangent test sections.

Table 6 Estimated Expected Average Flexural Strength for South Tangent Sections

Section	Nominal Thickness, mm	Average Age During HVS Testing (days)	Flexural Strength, MPa	Average Flexural Strength, MPa
519FD	100	30	4.53	4.68
520FD		40	4.62	
521FD		63	4.76	
522FD		77	4.81	
523FD	150	97	4.87	4.92
524FD		113	4.90	
525FD		122	4.92	
526FD		126	4.93	
527FD		175	5.00	
528FD	200	227	5.05	5.08
529FD		248	5.06	
530FD		299	5.09	
531FD		337	5.11	

strength gain over time, and because the slabs were tested in order from the 100- to the 150- to the 200-mm thick sections, the FSHCC strengths are combined into the three groups based on the nominal thicknesses as shown in Table 6.

3.3 FSHCC Elastic Modulus

An earlier study included back-calculation of elastic moduli for FSHCC slabs using FWD (Falling Weight Deflectometer) deflections at the Palmdale test site on both the North Tangent and the South Tangent sections at various FSHCC ages (1 day, 7 day, 50 day, and 90 day) collected between 10:00 am and 1:00 pm.(*3*) The average elastic modulus of the concrete slabs on the North Tangent was approximately 42,500 MPa (6,100 psi). The elastic modulus backcalculated for the 200-mm (8-in.) sections on the South Tangent averaged 39,700 MPa (5,700 psi). Back-calculation for the 100-mm (4-in.) and 150-mm (6-in.) sections on the South Tangent produced unreliable results due to the thinness of the slabs. Because of the uniform FSHCC thickness on the North Tangent sections (nominally 200 mm [8 in.]), the FWD data for the North Tangent were more consistent than those for the South Tangent. The back-calculation was performed using the Dynatest ELCON program (*5*) and the results were reasonably consistent with other methods of back-calculation such as AREA7 (*6*). An elastic modulus of 42,500 MPa (6,100 psi) was used in the analysis because of the consistency of the North Tangent data. Longer term FWD data and the day versus night variation are included in Reference (*4*).

3.4 FSHCC Coefficient of Thermal Expansion

The average value for the coefficient of thermal expansion of the FSHCC was 8.14×10^{-6} mm/mm/ºC (4.52 in./in./ºF) as determined experimentally by Heath and Roesler (*7*). This value was used in the South Tangent analysis.

3.5 Crack Pattern and Visual Observation Comparisons

The following summary is based on detailed observations in Reference (*4*).

3.5.1 <u>100-mm nominal thickness sections</u>

The visual observations and crack patterns for the 100-mm nominal thickness sections are summarized below. Since there was no dynamic loading on Section 522FD, the corresponding visual observations are not included here.

3.5.2 Section 519FD

Load Timeline	Observation
Prior to Loading	Medium size corner break on the left adjacent slab
At 2,105 repetitions of 25-kN load	Longitudinal crack throughout the length of the test slab, about 1.1 to 1.4 m respectively from the left and right slab corners, as shown in Figure 5
At 25,186 repetitions of 25-kN load	Large corner breaks, one on each of the left and right adjacent slabs
From 25,186–37,819 repetitions of 25-kN load	Slab deterioration and more cracking of the test slab (transverse cracks and corner breaks) as testing progressed
At 37,819 repetitions of 25-kN load	After occurrence of the longitudinal crack, the slab edge sunk into the base layer and a total drop-off between the slab edge and the asphalt shoulder of around 20 mm was recorded

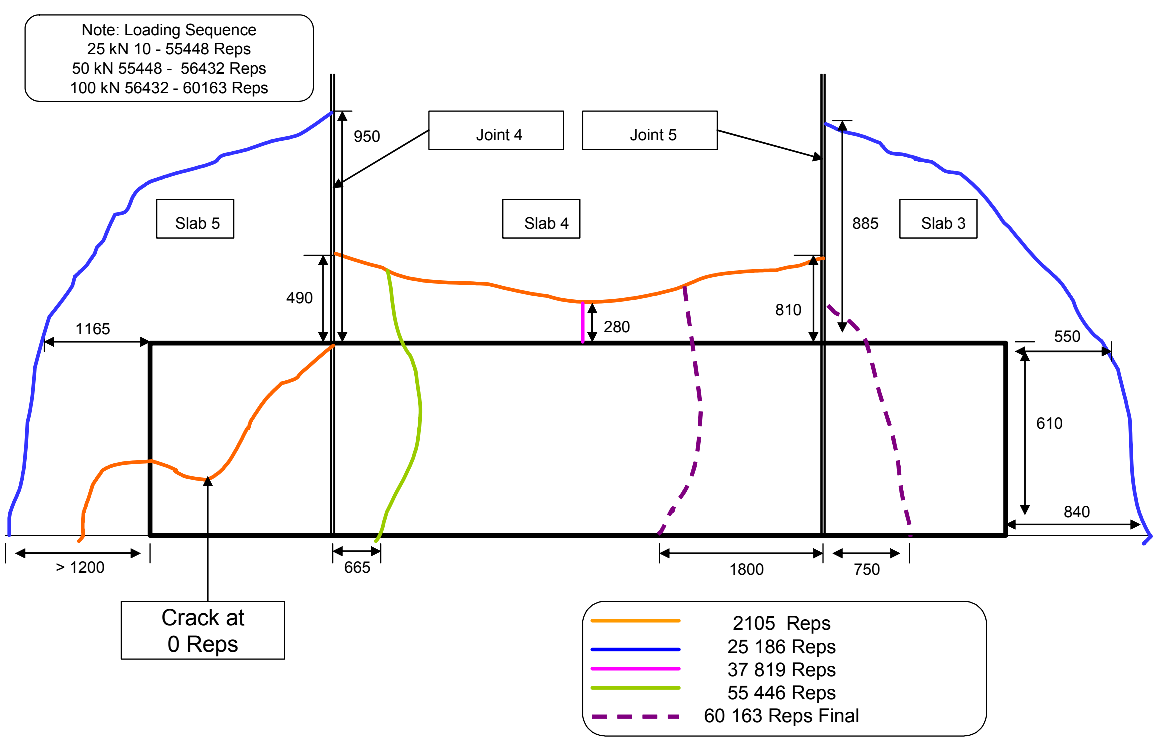

Figure 5a. 519FD: Schematic of crack development.(*4*)

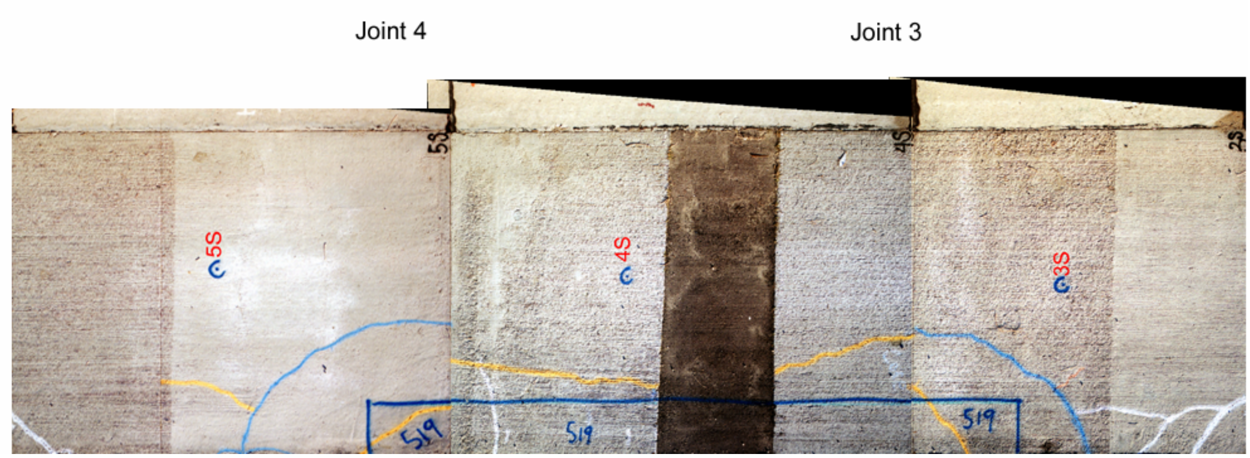

Note: asphalt was placed in cracked area after test completion.

Figure 5b. 519FD: Overhead photograph of tested section, 60,163 repetitions.

3.5.3 Section 520FD

Load Timeline	**Observation**
Prior to Loading	Medium size corner break on the left adjacent slab; Large corner break on the right adjacent slab
At 1,000 repetitions of 35-kN load	Longitudinal crack throughout the length of the test slab, about 1.1 m, from the left slab corner, as shown in Figure 6.
From 1,000 repetitions to end of test	Several transverse cracks and corner breaks occurred as testing progressed. Final crack pattern is shown in Figure 7.

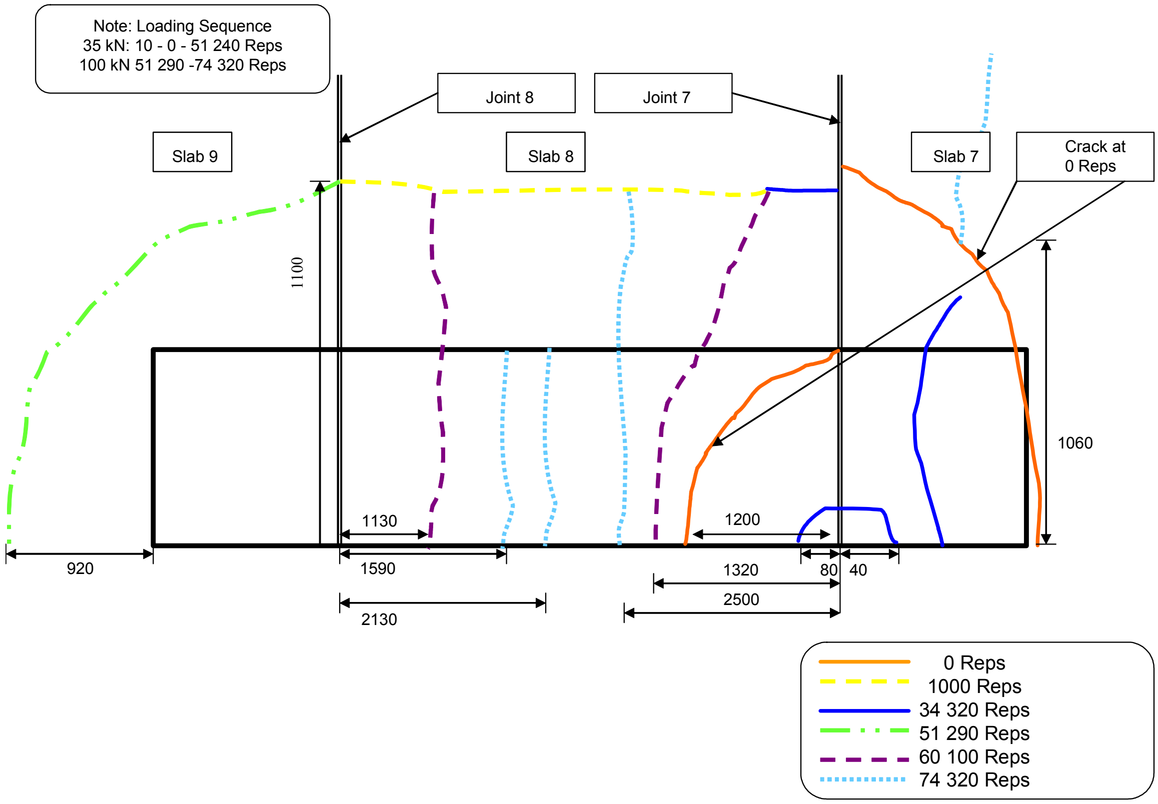

Figure 6a. 520FD: Schematic of crack development.(*4*).

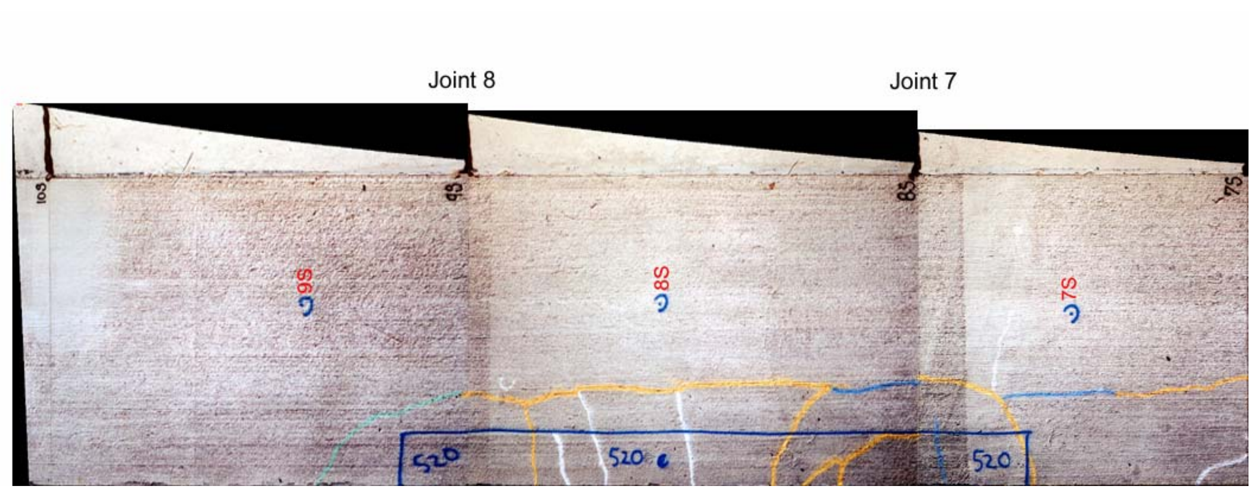

Figure 6b. 520FD: Overhead photograph of tested section, 74,320 repetitions.

Figure 7. 520FD: Final crack pattern after 74,000 repetitions (35 kN and 100 kN).

3.5.4 Section 521FD

Load Timeline	**Observation**
Prior to Loading	Very small corner crack on the left adjacent slab
At 500 repetitions of 20-kN load	Short longitudinal crack, about 1.4 m from the left slab corner, as shown in Figure 8..
At about 1,000 repetitions of 20-kN load	Corner break formed by progression of the short longitudinal crack towards the shoulder
At 142,072 repetitions of 20-kN load	Longitudinal crack between the corner break and the right joint, about 1.2 m from the right corner.
142,072 repetitions through end of test.	Several transverse cracks and corner breaks occurred as testing progressed. The final crack pattern is shown in Figure 9.

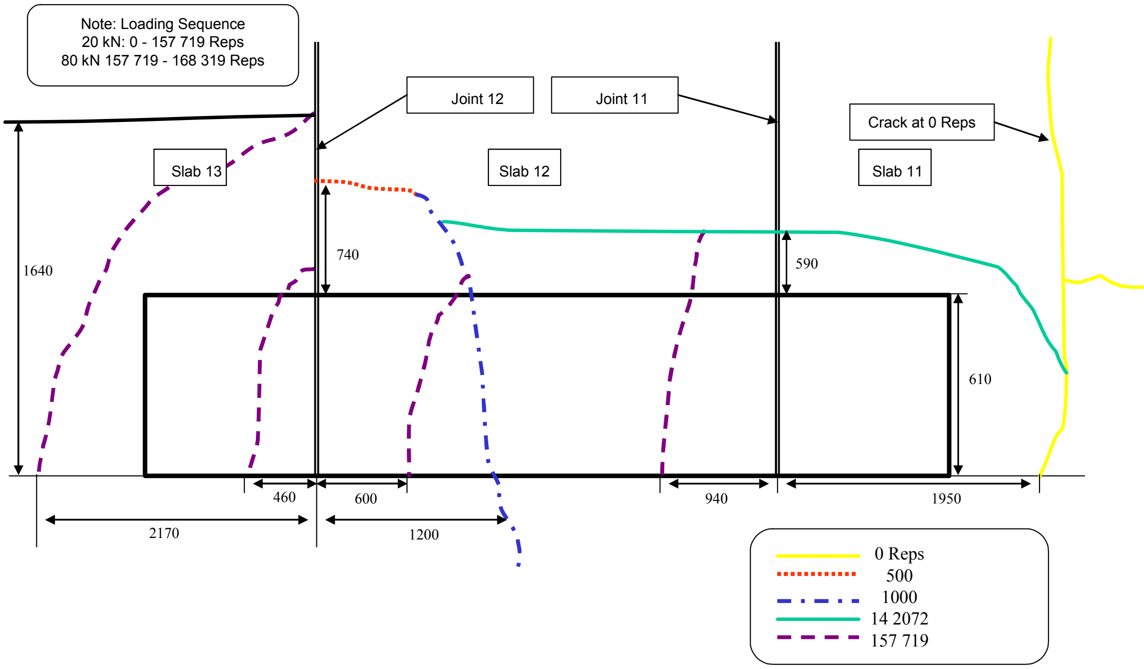

Figure 8a. 521FD: Schematic of crack development.(*4*)

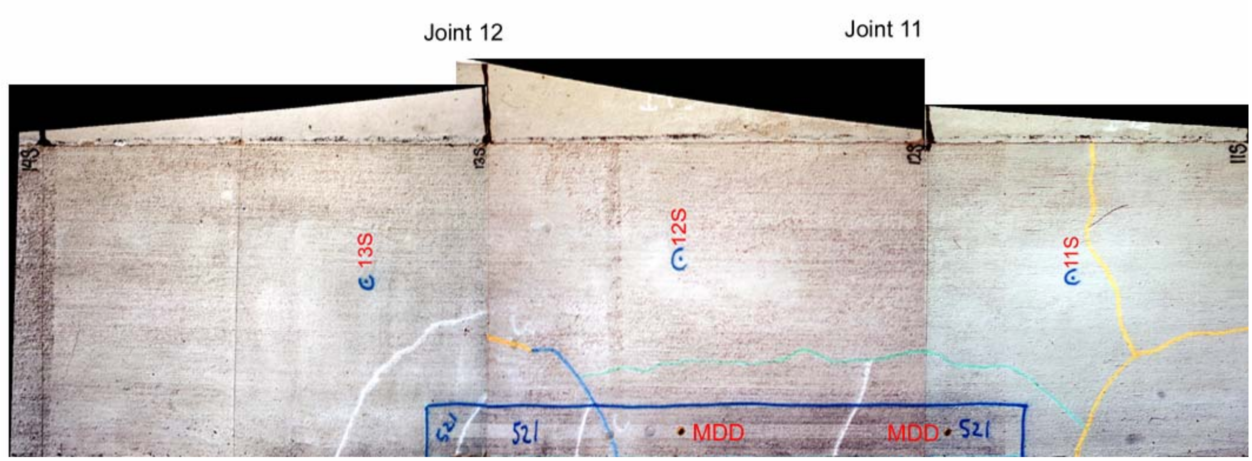

Figure 8b. 521FD: Overhead photograph of tested section, 168,319 repetitions.

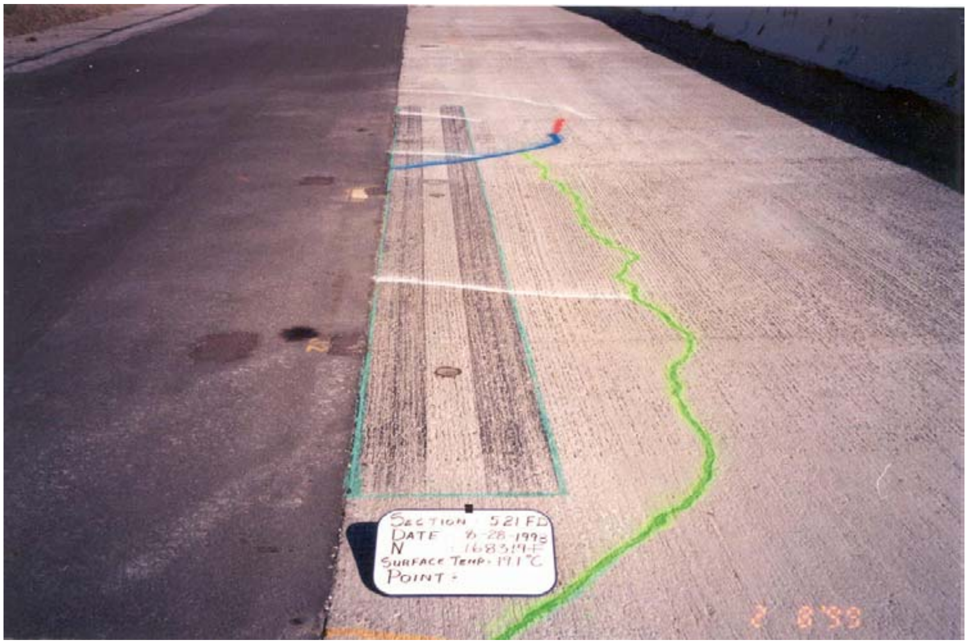

Figure 9. 521FD: Final Crack pattern after 168,319 repetitions (20 kN and 80 kN).

3.5.5 <u>100-mm nominal thickness section cracking summary</u>

All three sections had corner breaks or cracks on adjacent slabs prior to HVS loading. In addition, Section 520FD had a corner crack on the leave end of the test slab prior to loading. However, the first crack to occur on all of the 100-mm test slabs after HVS loading was a longitudinal crack at a distance of between 1.1 and 1.4 m from the slab corners. The associated load and number of repetitions for these longitudinal cracks is summarized in Table 7.

Table 7 Summary of Longitudinal Cracks for 100-mm Nominal Thickness Test Sections

Section	Load, kN	Repetitions	Distance from Corner 1, m	Distance from Corner 2, m
519FD	25	2,105	1.10	1.42
520FD	35	1,000	1.10	1.10
521FD	20	500	1.35	-

3.6 150-mm nominal thickness sections

The visual observations and crack patterns for the 150-mm nominal thickness sections are summarized below.

3.6.1 Section 523FD

Load Timeline	**Observation**
Prior to Loading	Several cracks on left adjacent slab.
Prior to Loading	Full length transverse crack on test slab approximately 300 mm from the left corner, as shown in Figure 10. The effect length of this slab is therefore approximately 5.10 m.
At 89,963 repetitions of 45-kN load.	The first crack after the HVS loading. This was a longitudinal crack that turned into a corner break on the test slab and remained a longitudinal crack on the adjacent slab, as shown in Figure 11. The distance of the longitudinal crack was 1.58 m from the right slab corner. The corner break intersected the slab-shoulder joint at a distance of 2.0 m from the right slab corner. The schematic of crack development is shown in Figure 12.

Figure 10. 523FD: Crack at transverse joint at start of test.

Figure 11. 523FD: Crack pattern after 89,963 repetitions of 45 kN.

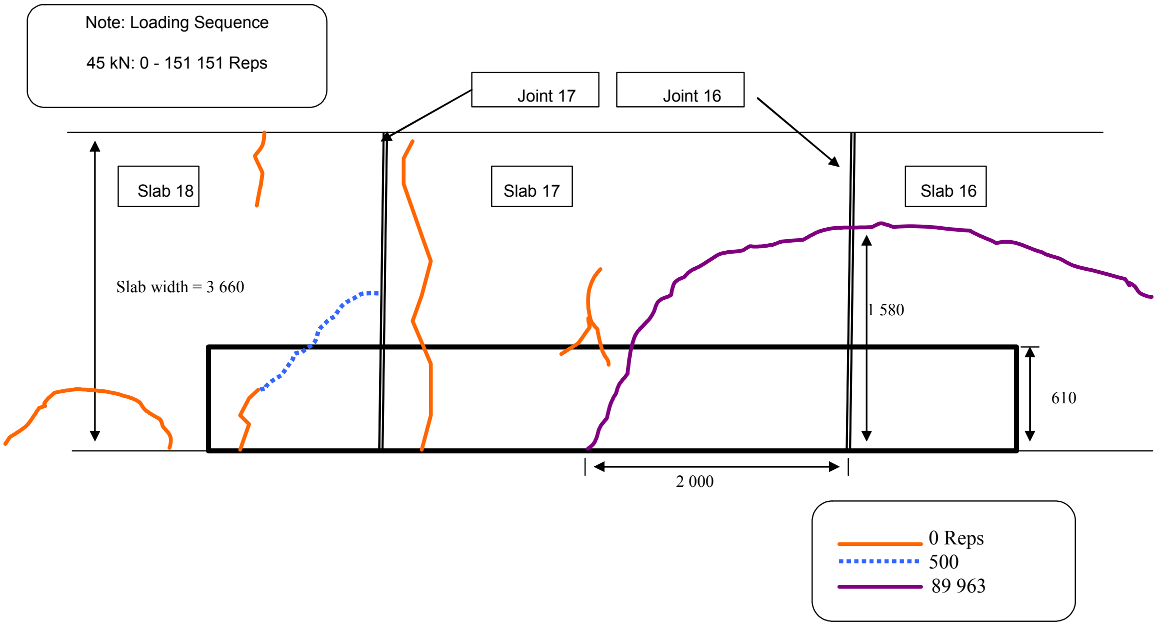

Figure 12a. 523FD: Schematic of crack development.(*4*)

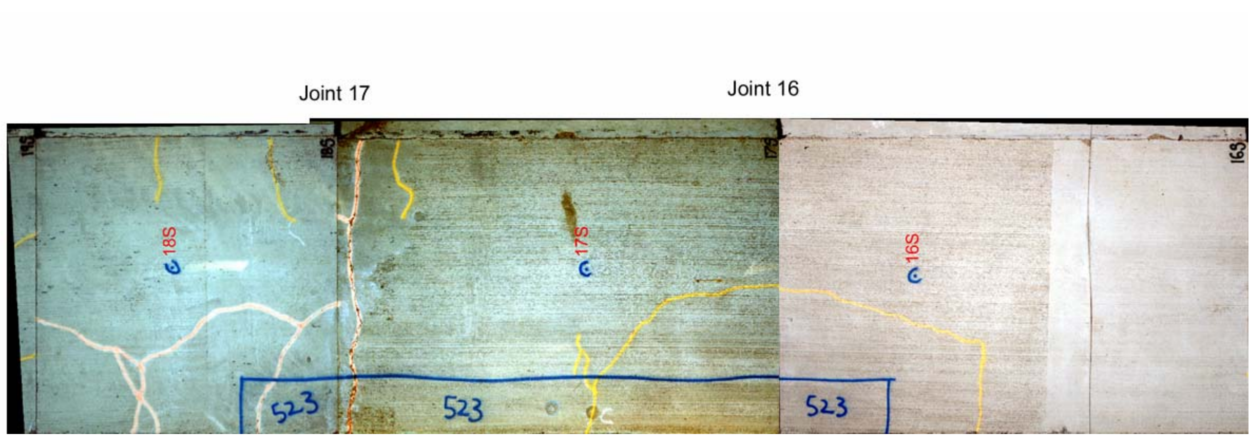

Figure 12b. 523FD: Overhead photograph of tested section, 151,151 repetitions.

3.6.2 Section 524FD

Load Timeline	Observation
At 30,000 repetitions of 45-kN load	Corner break on right adjacent slab after 30,000 repetitions of 45 kN
At 64,000 repetitions of 45-kN load.	Short longitudinal crack on right joint of test slab at a distance of 1.6 m from right slab corner, as shown in Figure 13.
At 102,935 repetitions of 45-kN load.	The longitudinal crack progressed into a corner break, as shown in Figure 14.

3.6.3 Section 525FD

Load Timeline	Observation
At 1,000 repetitions of 45-kN load	Corner break on test slab at a transverse distance of 1.66 m from the right slab corner, as shown in Figure 15. The longitudinal distance of this corner break was 1.7 m from the right slab corner as measured along the length of the slab. The schematic of crack development is shown in Figure 16.

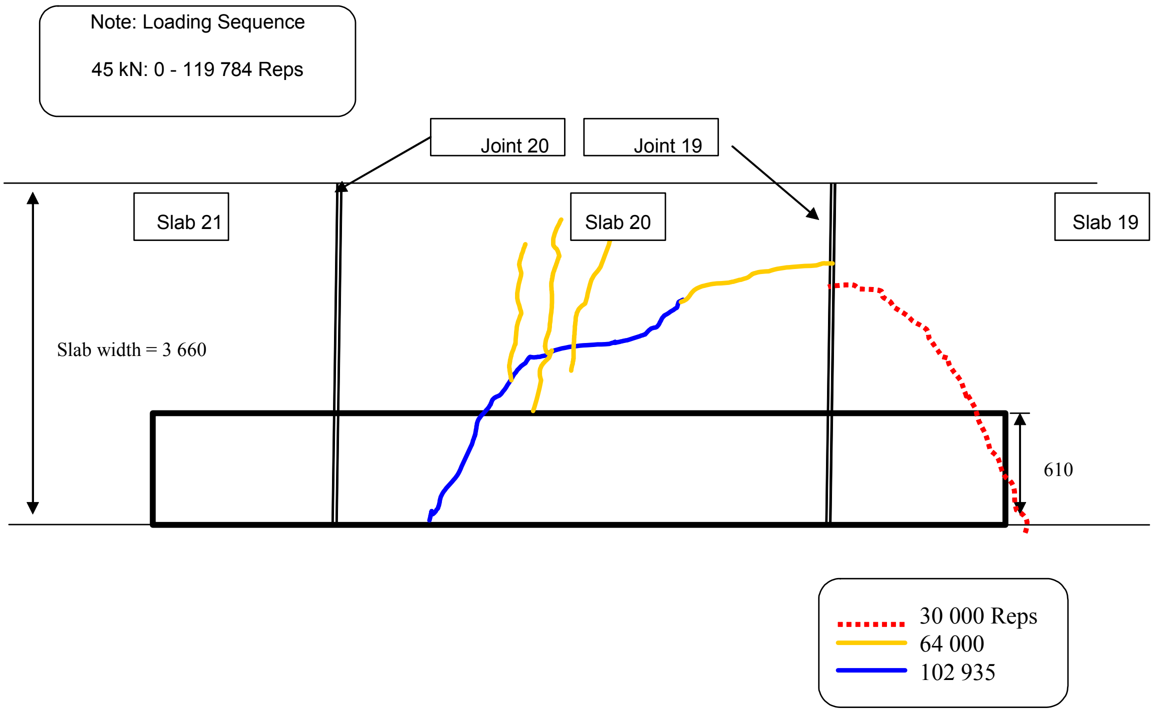

Figure 13a. 524FD: Schematic of crack development.(*4*)

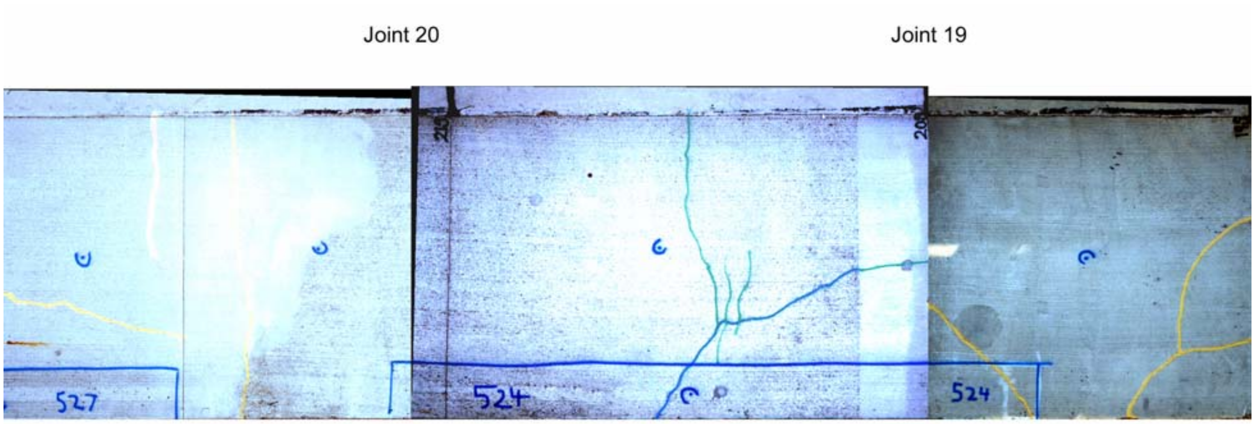

Figure 13b. 524FD: Overhead photograph of tested section, 119,784 repetitions.

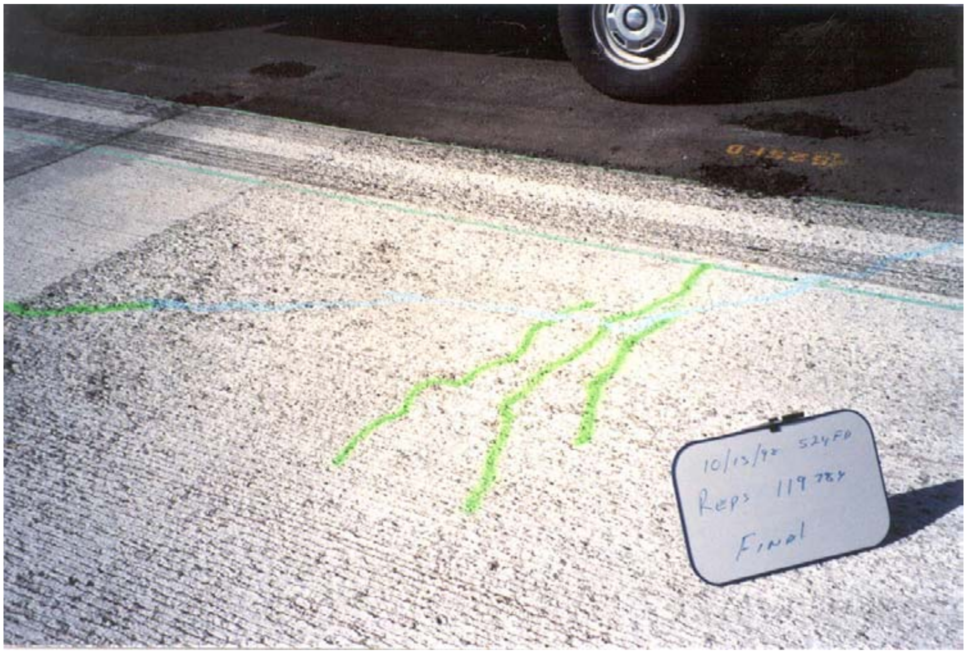

Figure 14. 524FD: Final crack pattern after 119,784 repetitions of 45 kN.

Figure 15. 525FD: Corner crack after 1,000 repetitions of 45 kN.

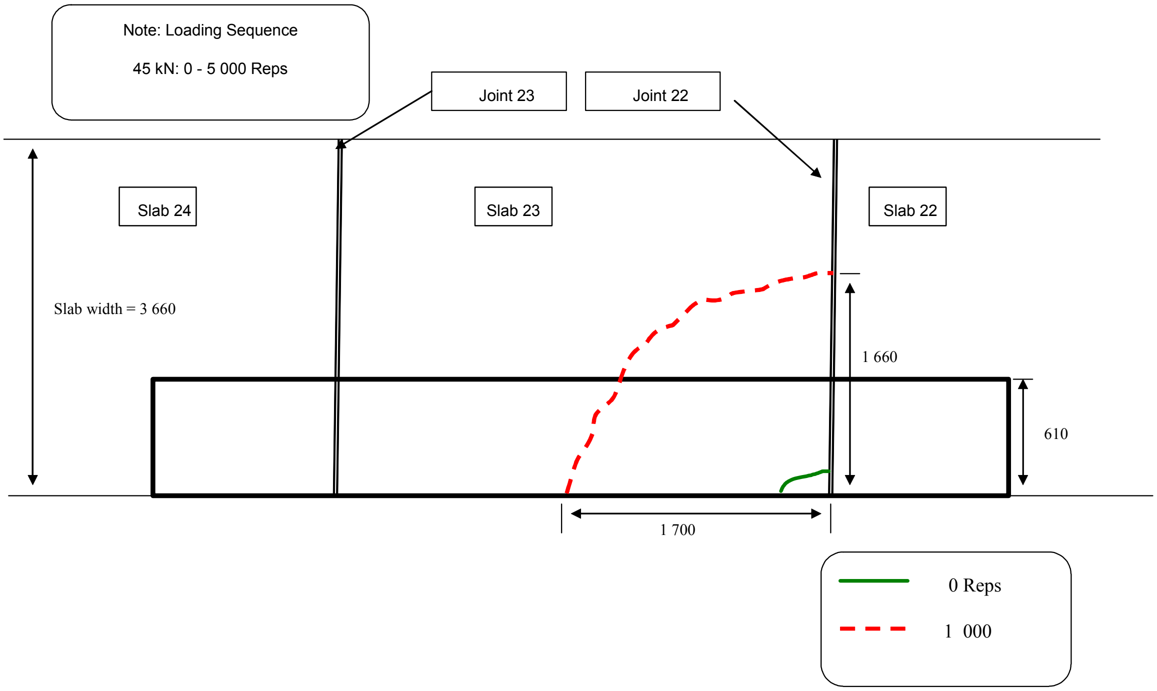

Figure 16a. 525FD: Schematic of crack development.(*4*)

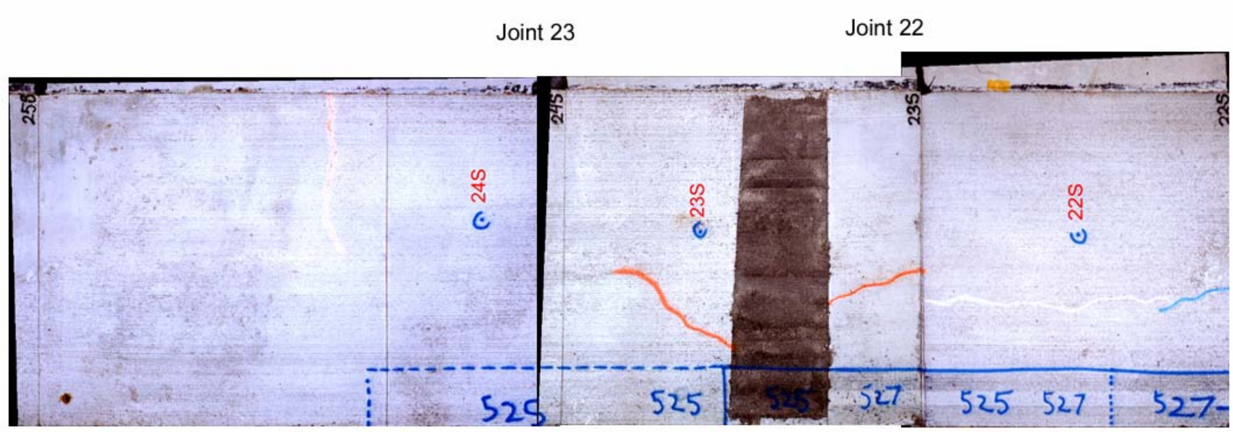

Note: Asphalt was filled into cracked area at completion of testing.

Figure 16b. 525FD: Overhead photograph of tested section, 5,000 repetitions.

3.6.4 Section 526FD

Load Timeline	**Observation**
Prior to loading.	Transverse crack on left adjacent slab
At 100 repetitions of 85-kN load.	Corner breaks on test slab and right adjacent slab, as shown in Figure 17. The transverse distance of the corner break was approximately 1.5 m and the longitudinal distance as measured along the length of the slab was approximately 1.6 m.
At 500 repetitions of 85-kN load	Longitudinal crack on test slab from left joint after. This crack intersects the existing corner break on the test slab as shown in Figures 18 and 19. Transverse cracks on both the test slab and right adjacent slab. Corner break on the left adjacent slab.

Figure 17. 526FD: Corner cracks after 100 repetitions of 85 kN.

Figure 18. 526FD: Crack pattern after 500 repetitions of 85 kN.

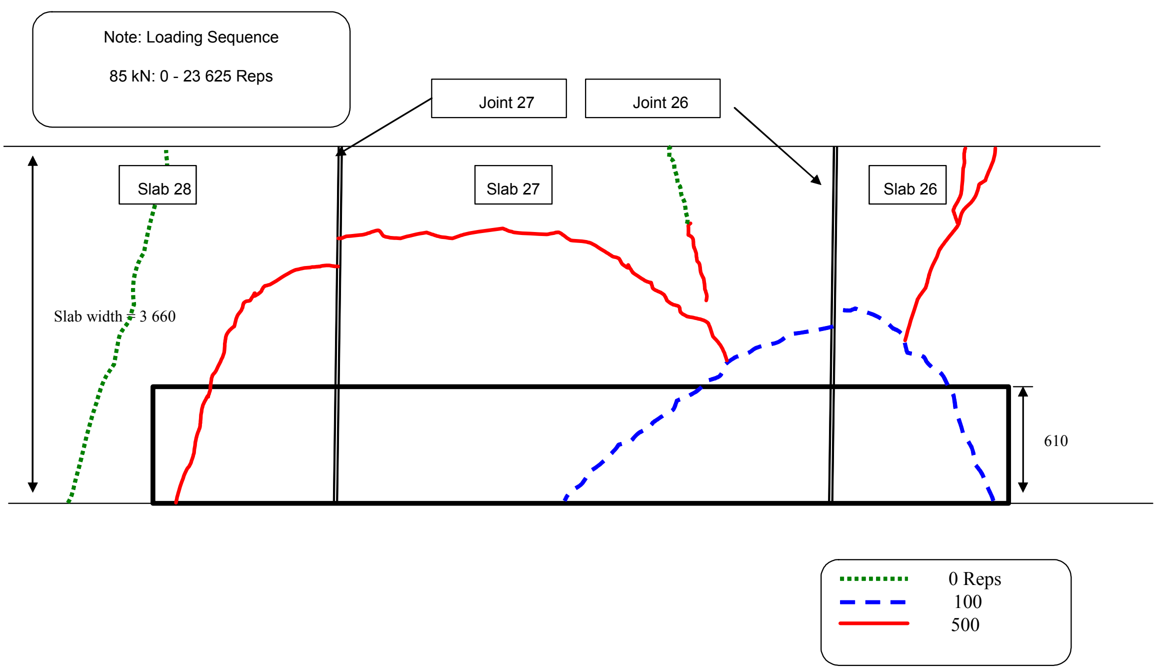

Figure 19a. 526FD: Schematic of crack development.(*4*)

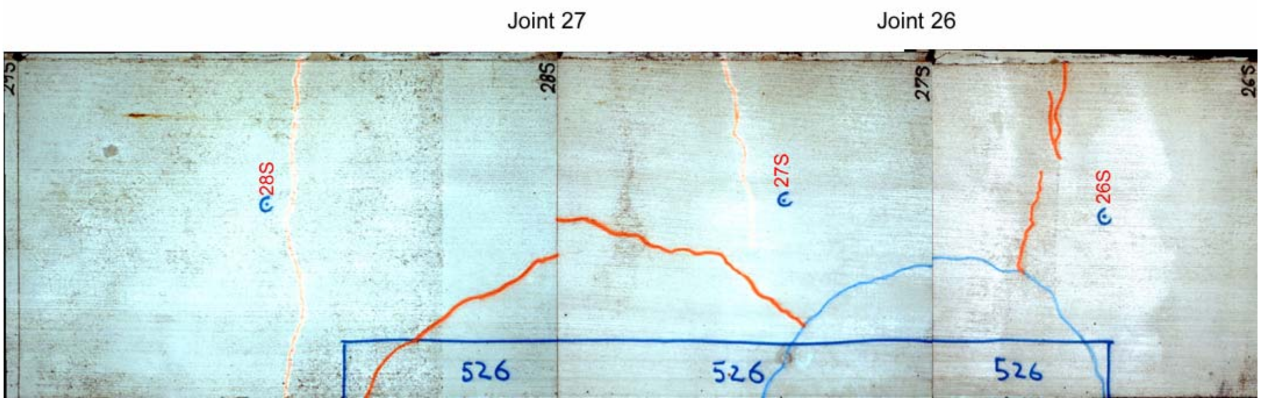

Figure 19b. 526FD: Overhead photograph of tested section, 23,625 repetitions.

3.6.5 <u>Section 527FD</u>

Load Timeline	**Observation**
Prior to loading	Large corner break on left adjacent slab
At 129,805 repetitions of 35-kN load.	Partial longitudinal crack at a transverse distance of 1.5 m from the left slab corner, as shown in Figure 20.
At 890,000 repetitions of 35-kN load	Short longitudinal crack at a transverse distance of 1.5 m from the right slab corner. This crack progressed into a full length crack on the right adjacent slab.

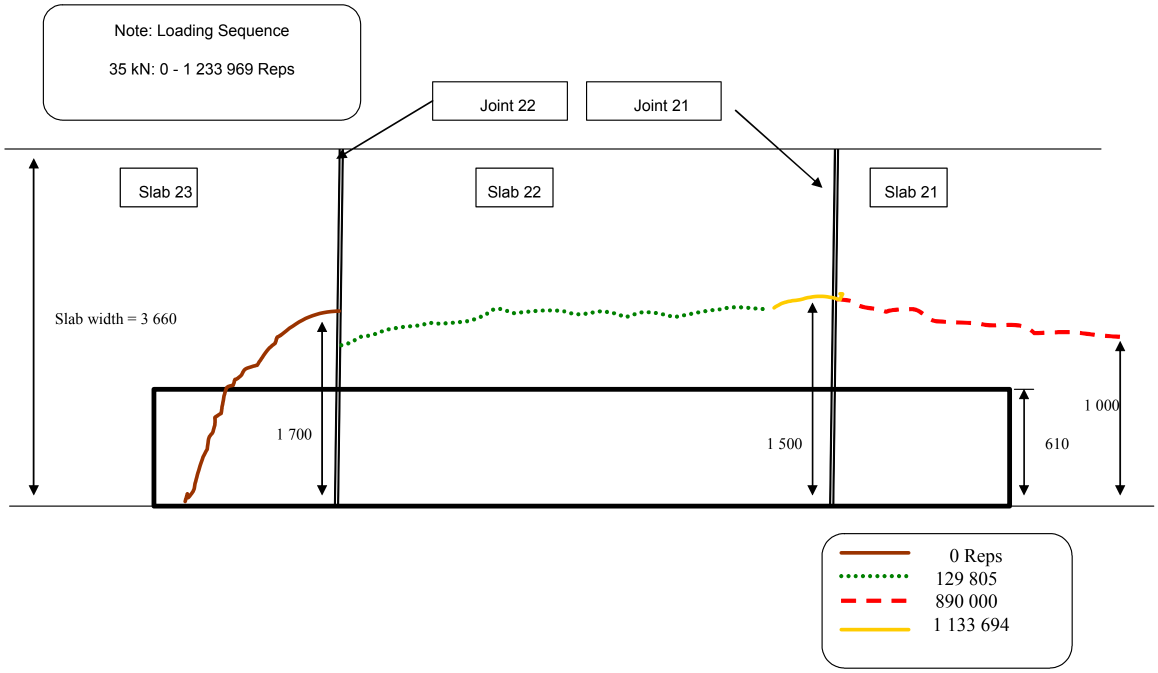

Figure 20a. 527FD: Schematic of crack development.(*4*)

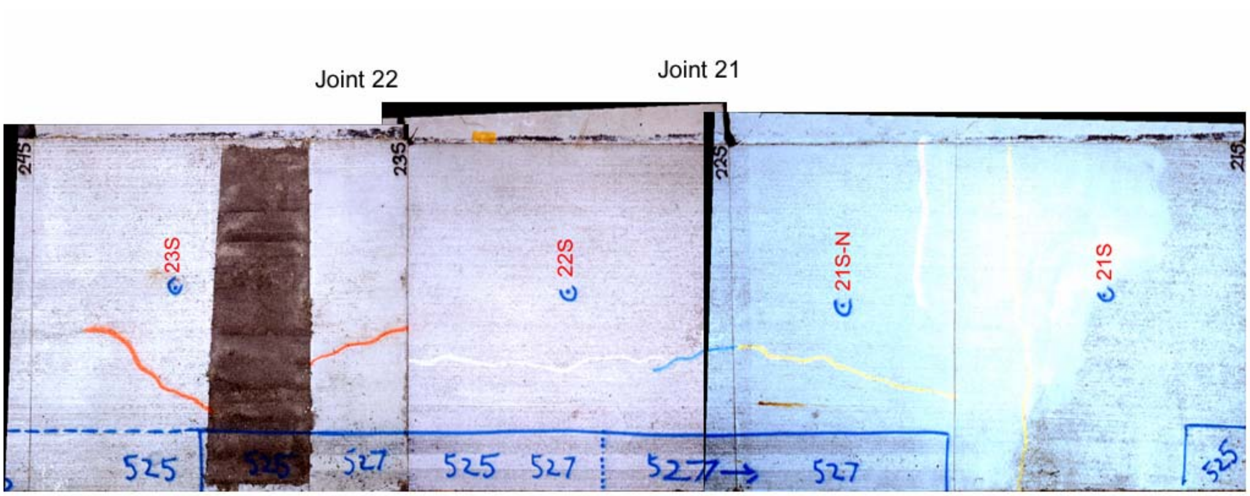

Note: Asphalt was placed in the cracked area at the completion of testing.

Figure 20b. 527FD: Overhead photograph of tested section, 1,233,969 repetitions.

3.6.6 150-mm nominal thickness section cracking summary

Some of the test sections had corner breaks or cracks on adjacent slabs prior to HVS loading. However, the first crack to occur on all the 150-mm test slabs after HVS loading was a longitudinal crack or a corner break at a transverse distance of between 1.5 and 1.7 m from the slab corners. The associated load and number of repetitions for cracks is summarized in Table 8.

Table 8 Summary of First Crack Occurrence for 150-mm Nominal Thickness Test Sections.

Section	Crack Type	Load, kN	Repetitions	Transverse Distance from Corner, m	Longitudinal Distance from Corner, m
523FD	corner break	45	89,963	1.6	2.0
524FD	Longitudinal crack*	45	64,000	1.6	2.1
525FD	Corner break	45	1,000	1.7	1.7
526FD	Corner break	85	100	1.5	1.6
527FD	Longitudinal Crack	35	129,805	1.5	-

*Progressed after additional loading to corner break.

3.7 200-mm nominal thickness sections

The visual observations and crack patterns for the 200-mm nominal thickness sections are summarized below.

3.7.1 Section 528FD

Load Timeline	**Observation**
At 56,912 repetitions of 40-kN load	Midslab transverse crack, as shown in Figure 21.
56,912 repetitions of 40-kN load to end of test.	The midslab transverse crack extended with additional load applications but did not extend to the full length of the slab or did not become a corner break.

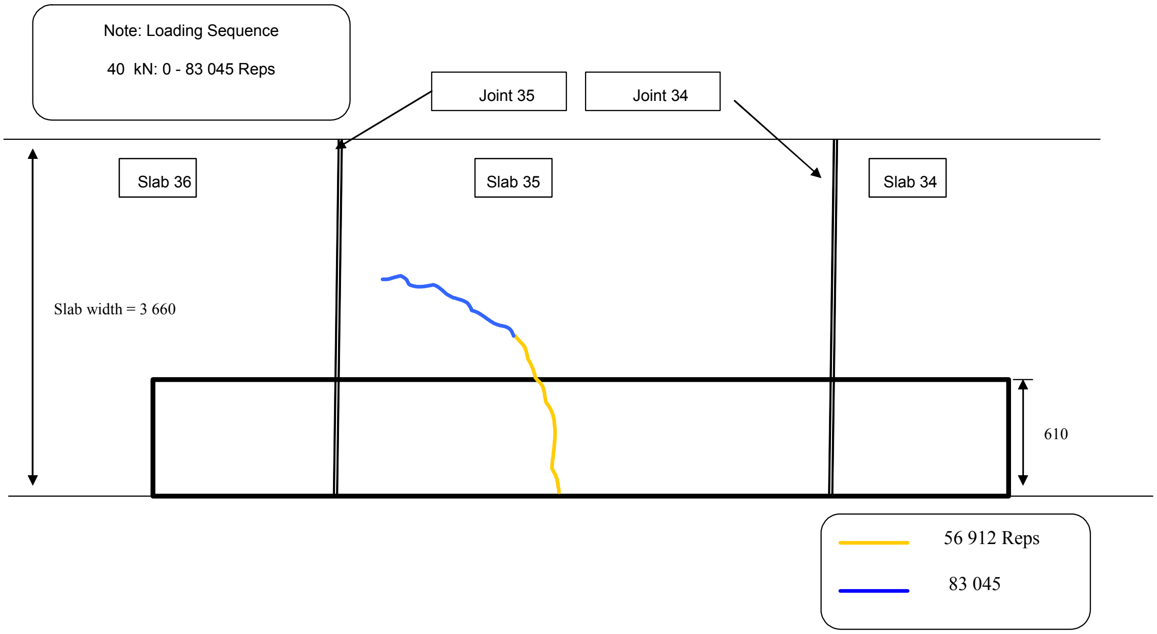

Figure 21a. 528FD: Schematic of crack development.(*4*)

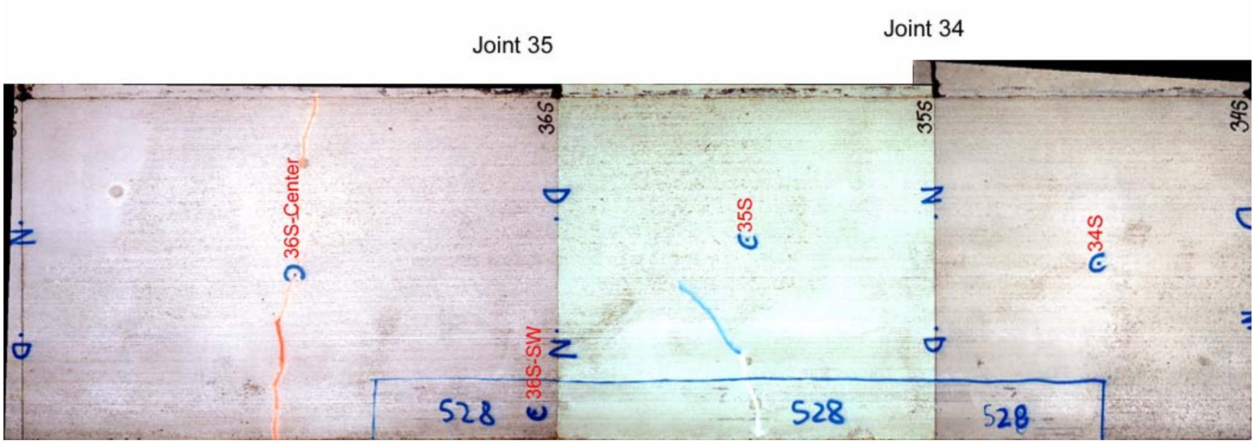

Figure 21b. 528FD: Overhead photograph of tested section, 83,045 repetitions.

3.7.2 Section 529FD

Load Timeline	**Observation**
At 230,130 repetitions (88,110 repetitions of 40-kN load and 142,020 repetitions of 60-kN load)	Corner break on right adjacent slab.
At 322,533 repetitions (88,110 repetitions of 40-kN load and 234,423 repetitions of 60-kN load)	Short longitudinal crack on test slab at a distance of 1.73 m from the right slab corner.
At 337,530 repetitions (88,110 repetitions of 40-kN load and 249,420 repetitions of 60-kN load)	Longitudinal crack propagated to corner break, as shown in Figure 22. The final crack pattern is shown in Figure 23.

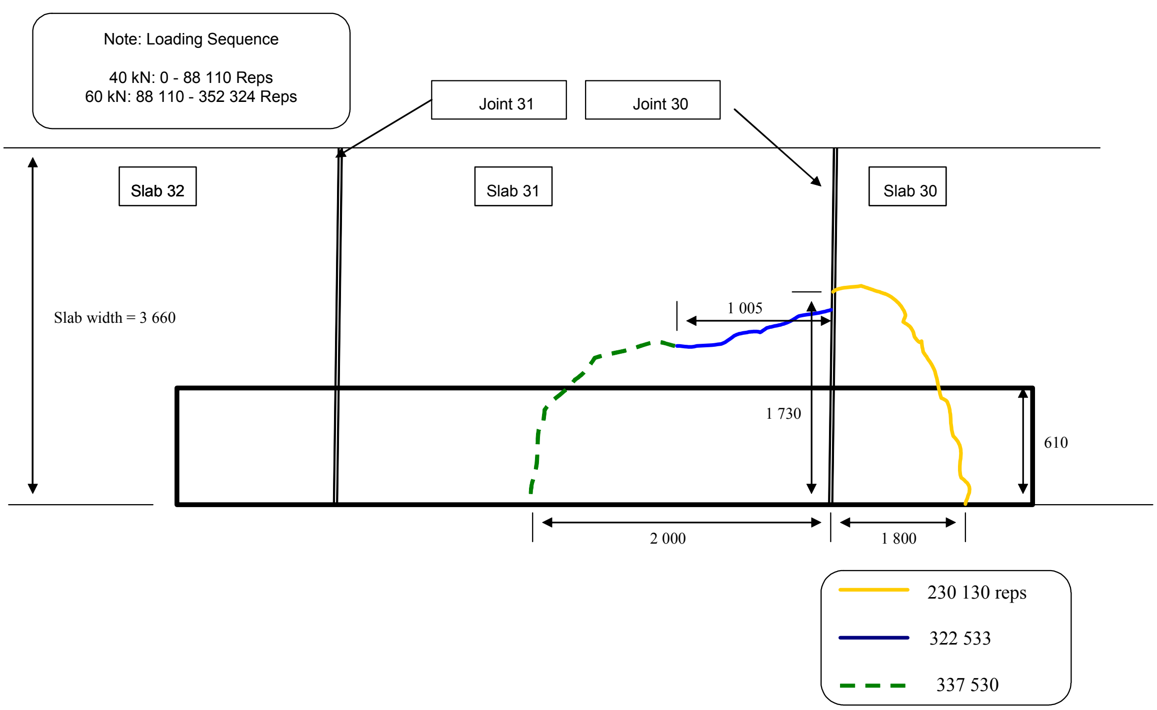

Figure 22a. 529FD: Schematic of crack development.(*4*)

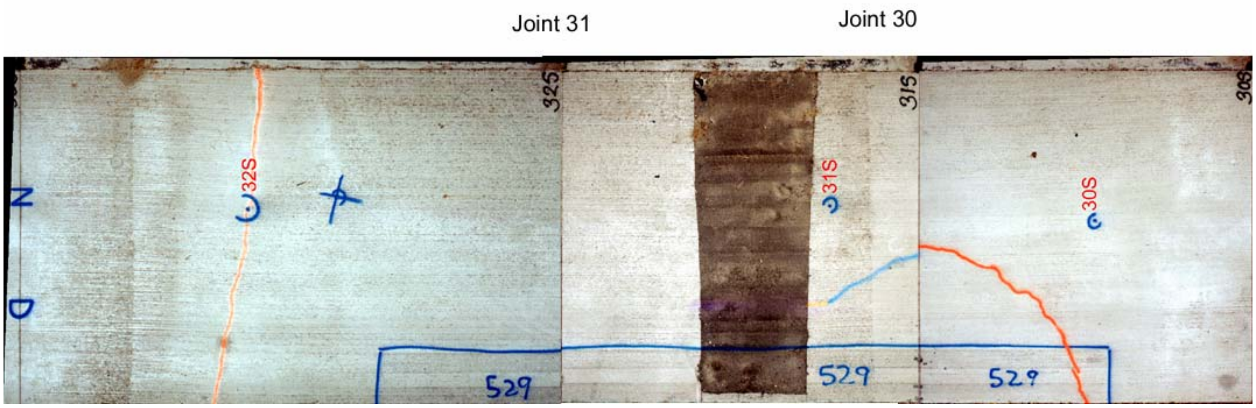

Note: asphalt was filled into cracked area at completion of testing.

Figure 22b. 529FD: Overhead photograph of tested section, 352,324 repetitions.

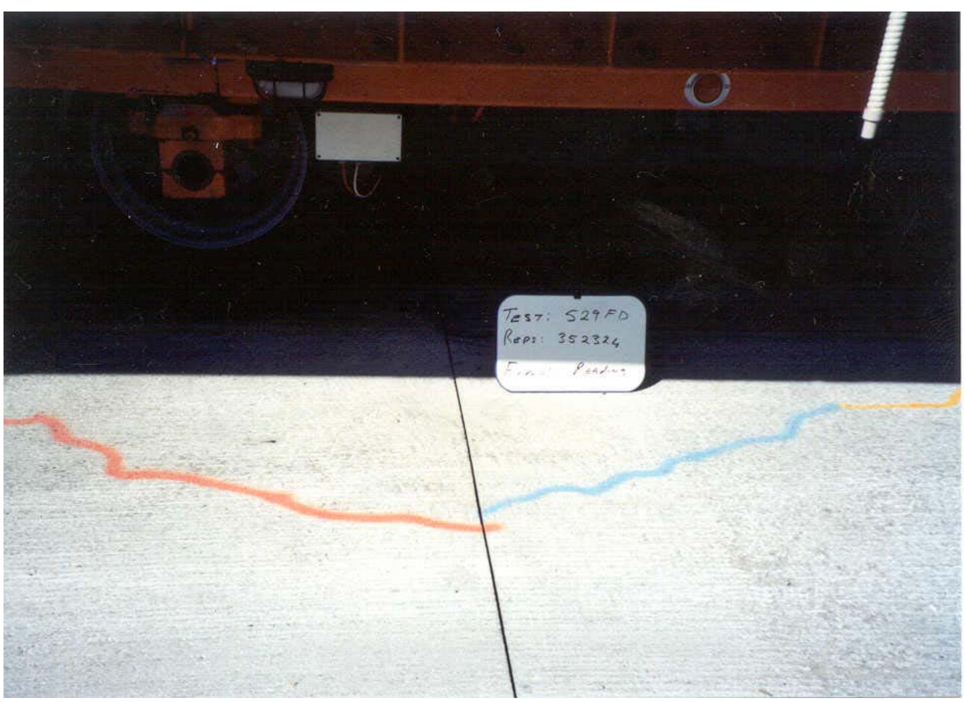

Figure 23. 529FD: Final crack pattern after 352,324 repetitions of 40 kN and 60 kN.

3.7.3 Section 530FD

Load Timeline	Observation
At 291,684 repetitions (64,227 repetitions of 40-kN load and 227,457 repetitions of 60-kN load)	Corner break on the right adjacent slab.
At 846,845 repetitions (64,227 repetitions of 40-kN load; 752,448 repetitions of 60-kN load; and 30,170 repetitions of 90-kN load)	Corner break on test slab, as shown in Figures 24 and 25. The transverse distance of the corner break was 1.44 m from the right slab corner and the longitudinal distance of the corner break as measured along the length of the slab was 1.34 m from the right slab corner.

Figure 24. 530FD: Final crack pattern after 846,844 repetitions of 40 kN, 60 kN, and 90 kN.

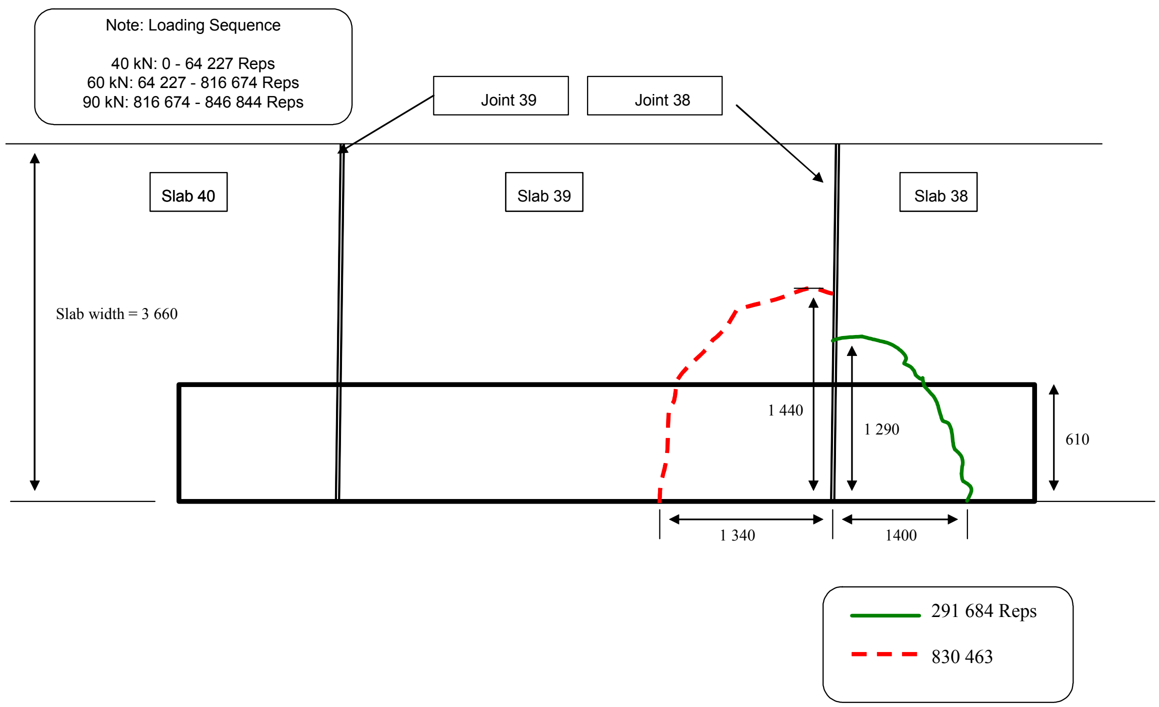

Figure 25a. 530FD: Schematic of crack development.(*4*)

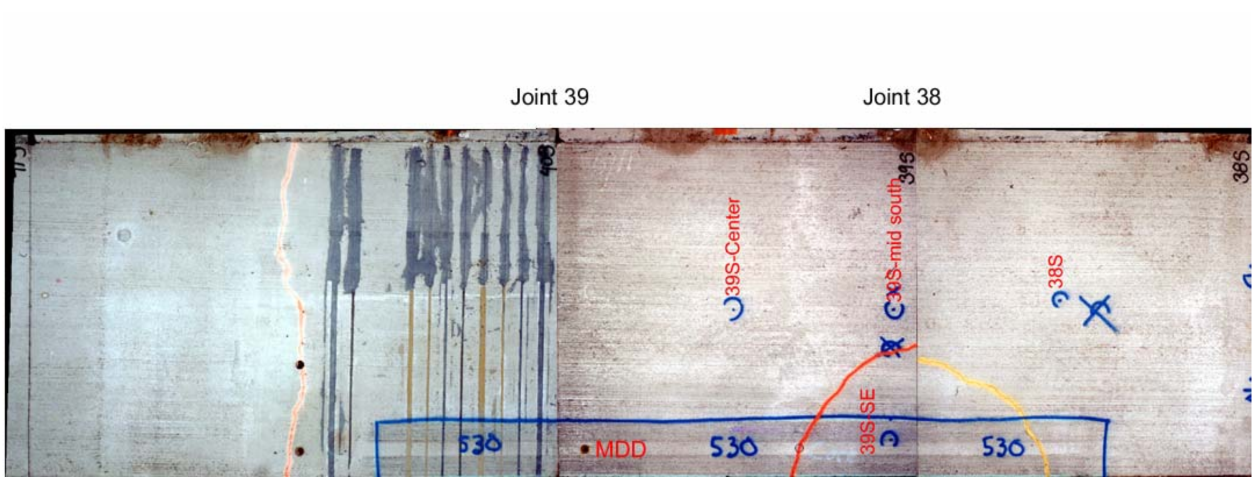

Figure 25b. 530FD: Overhead photograph of tested section. 846,844 repetitions.

3.7.4 Section 531FD

Load Timeline	**Observation**
At 62,813 repetitions (31,318 repetitions of 40-kN load and 31,495 repetitions of 70-kN load)	Longitudinal crack on left adjacent slab. Corner break on test slab, as shown in Figures 26 and 27. This corner break measures 1.7 m from the left slab corner in the transverse direction and 1.5 m from the left slab corner in the longitudinal direction as measured along the length of the slab.

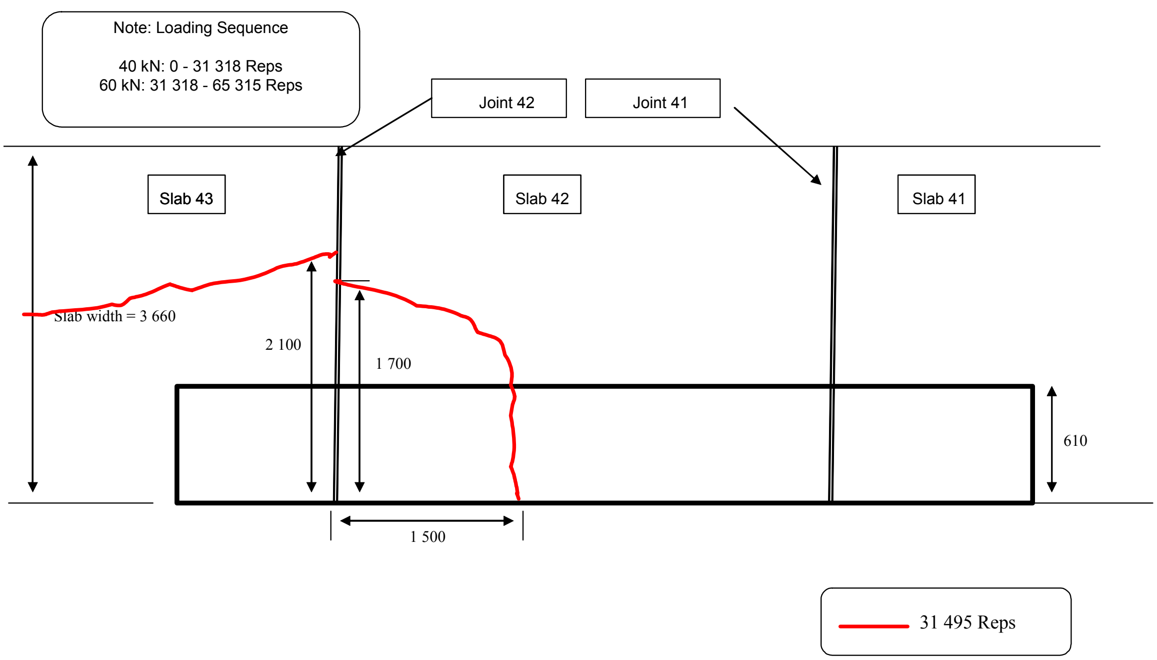

Figure 26a. 531FD: Schematic of crack development.(*4*)

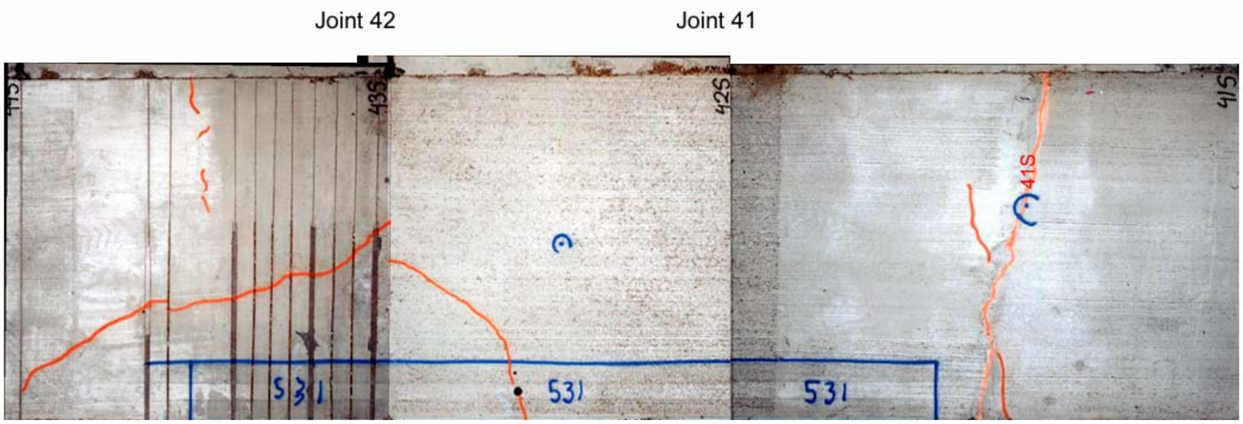

Figure 26b. 531FD: Overhead photograph of tested section, 65,315 repetitions.

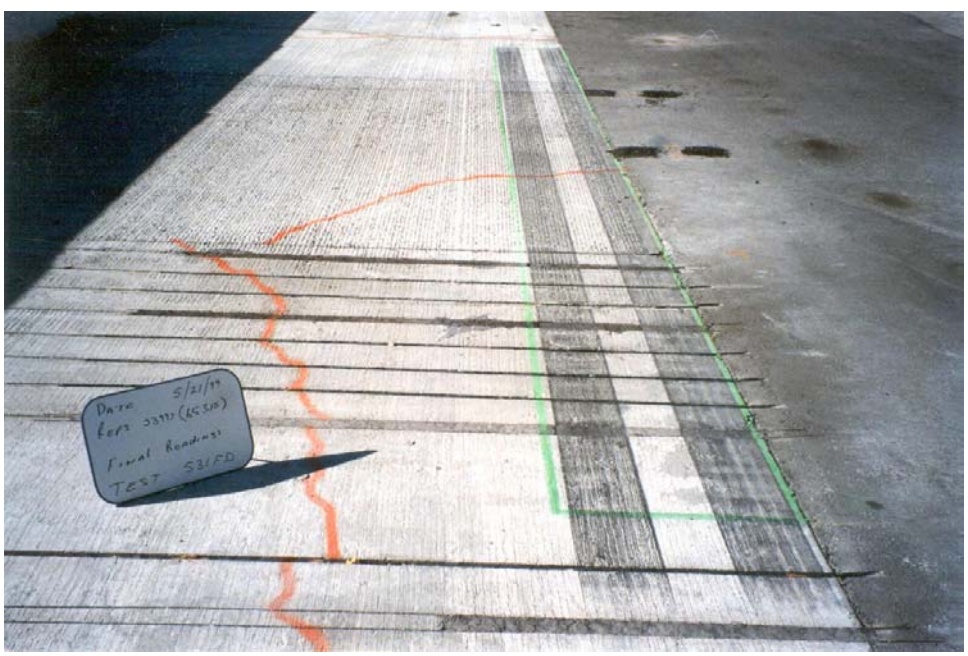

Figure 27. 531FD: Final crack pattern after 65,315 repetitions of 40 kN and 70 kN.

3.7.5 200-mm nominal thickness section cracking summary

None of the test sections or the adjacent slabs had any cracks prior to HVS loading. However, the first crack to occur on three of the 200-mm test slabs after HVS loading was a longitudinal crack (or a corner break) at a transverse distance of between 1.4 and 1.7 m from the slab corners. Section 528FD never developed a corner break or a longitudinal crack through the course of the HVS loading. The only crack on this section was a short transverse crack. The associated load and number of repetitions for first cracks on the test slab is summarized in Table 9.

Table 9 Summary of First Crack Occurrence for 200-mm Nominal Thickness Test Sections

Section	Crack Type	Load, kN	Repetitions	Transverse Distance from Corner, m	Longitudinal Distance from Corner, m
528FD	Transverse crack	40	56,912	-	2.0
529FD	Longitudinal crack*	40 60	88,110 234,423	1.7	-
530FD	Corner break	40 60 90	64,227 752,448 30,170	1.4	1.3
531FD	Corner break	40 70	31,318 31,495	1.7	1.5

*Progressed after additional loading to corner break.

4.0 TEMPERATURE CURLING AND MOISTURE WARPING ANALYSIS

The objective of the analysis is to estimate an effective linear built-in temperature difference (EBITD) in the slab to simulate the effects of moisture shrinkage and construction temperature gradients. This section includes:

- Discussion of thermal gradients in concrete pavements and construction curling and moisture warping resulting in an effective built-in temperature difference.
- Procedure for estimating effective linear built-in temperature difference using rolling wheel deflections and finite element analysis.
- Discussion of why unloaded slab deflections measured under ambient conditions cannot be used to estimate effective linear built-in temperature difference for slabs with high negative curl.

4.1 Thermal Gradients in Concrete Pavements

During daytime, the top of the concrete slab is warmer than the bottom, resulting in a positive thermal gradient through the slab. The result is an elongation of the top of the slab relative to the bottom of the slab and a convex curvature, as shown in Figure 28. This is effectively equivalent to a void beneath the middle of the slab. During nighttime, the top of the concrete slab is cooler than the bottom, resulting in a negative thermal gradient through the slab. This difference results in a concave curvature of the slab, as shown in Figure 29, that is effectively equivalent to voids beneath the edges and corners of the slab.

4.2 Construction Curling and Moisture Warping

Concrete paving is typically performed during the daytime in warmer months of the year. During daytime paving with rapid setting materials, the top of the slab is warmer than the bottom

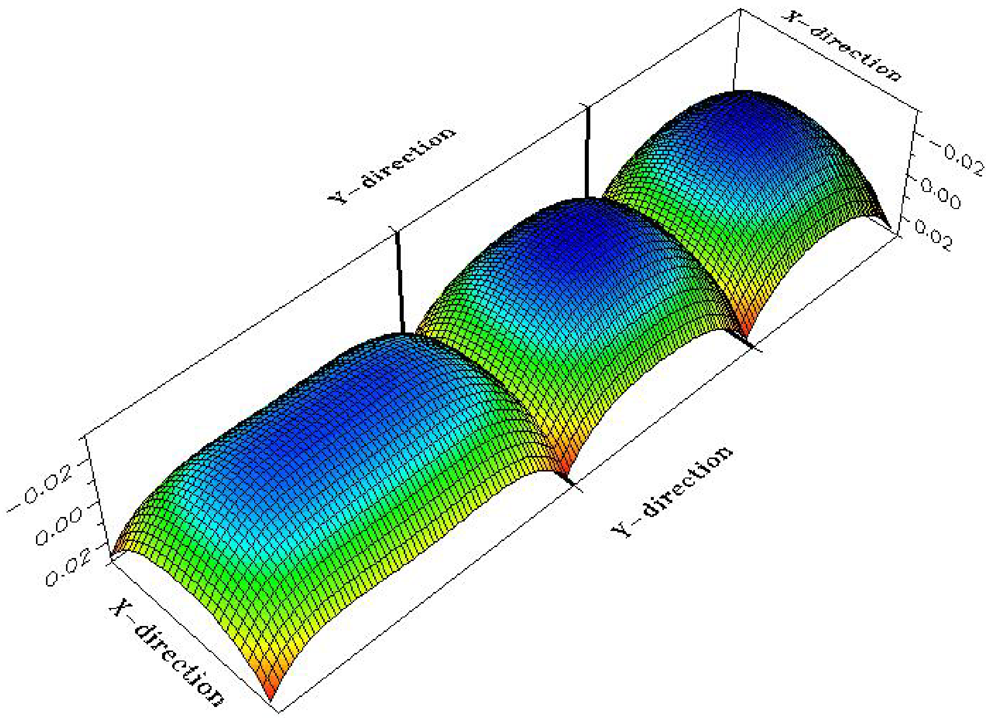

Figure 28. Downward (convex) curling of concrete slab due to daytime positive thermal gradient.

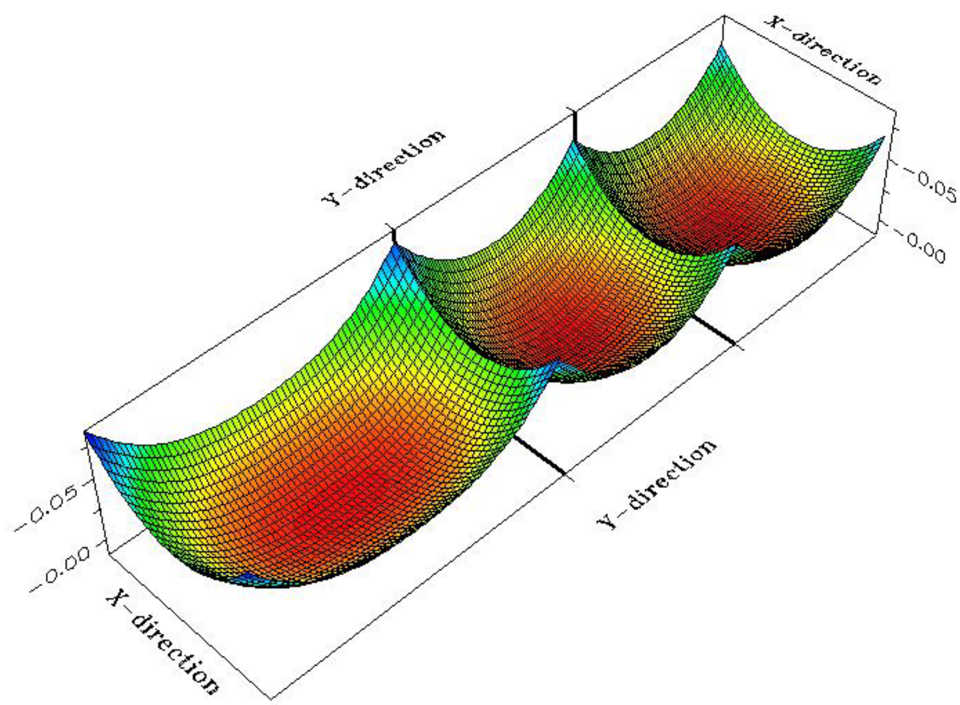

Figure 29. Upward (concave) curling of concrete slab due to nighttime negative thermal gradient.

at set time in many cases. Because the concrete slab sets under this condition, the flat slab condition is no longer associated with a zero temperature gradient. When the temperature gradient in the slab is zero, the slab curls upward at the corners toward a concave profile rather than remains flat. Thus, an effective negative temperature gradient is “built into” the slab, and is referred to as the built-in construction curling gradient.

After placement, water evaporates from the top of the slab and also to a lesser extent, from the bottom of the slab. Over time, the top of the slab shrinks more relative to the bottom of the slab. This results in a concave warping of the slab. As in the case of construction curling, an effect negative temperature is “built into” the slab, and this is called the built-in moisture warping gradient.

The combination of the construction curling and moisture warping effectively results in a void beneath the slab corners and to a lesser extent, beneath the slab edges. The net result of these effective voids beneath the slab is higher deflections in the slab under the influence of applied loads at the slab edge and corners. For the purposes of deflections, the combination of the construction curling and moisture warping can be modeled as an effective negative linear temperature difference between the top and the bottom of the slab.

Using Finite Element Analysis (FEM) software such as ISLAB2000, this effective linear built-in temperature difference in the slab can be estimated using the measured corner deflections. Note that the actual effective built-in temperature distribution in the concrete can be highly nonlinear. However, the equivalent linear difference that results in the same deflection as the actual nonlinear distribution can be estimated. The equivalent linear differences are easier to quantify, analyze, communicate, and compare as opposed to nonlinear temperature distributions, however the non-linear gradients produce higher stresses than the equivalent linear differences.

4.3 ISLAB2000 Requirements

The inputs required to run ISLAB2000 are listed below:

- Geometry – slab lengths and widths
- Mesh – finite element meshed required for the analysis
- Load – magnitudes, positions, and tire imprint dimensions assuming rectangular loads
- Subgrade – modulus of subgrade reaction (k-value)
- Temperature – type of temperature distribution through slab (linear, quadratic, and nonlinear) and corresponding temperatures
- Load Transfer Efficiency (LTE) – ratio of unloaded slab deflection to loaded slab deflection across a joint
- Slab thickness and base thickness
- Slab properties – elastic modulus, Poisson's ratio, unit weight, coefficient of thermal expansion
- Base properties – elastic modulus, Poisson's ratio, unit weight, coefficient of thermal expansion, bond type with slab

4.4 Estimation of Effective Linear Built-In Gradients based on Measured Corner Deflections

Using known values for the ISLAB2000 inputs (Section 4.3) for the South Tangent test sections, slab corner deflections are calculated as a function of vertical temperature difference in the slab. After taking into consideration the actual temperature difference in the slab during test conditions, the resulting temperature difference corresponding to the measured corner deflection is the effective linear built-in temperature difference.

The corner deflection data point was selected such that it satisfied the following criteria:

- Number of repetitions should not exceed load repetitions when first crack observed. The ISLAB2000 modeling used assumes that the slab is intact. Therefore, a cracked slab would negate the results.
- The first few data points typically had very high corner and edge deflections. These deflections settled down after 500 – 1000 load repetitions. The high deflections could have been due to the settling of slab in position resulting from base/subgrade irregularities that occurred during construction and during slab thermal movement prior to loading. Because the deflections were not representative, the first few data points were not used.
- The slab deflections were also affected by permanent deformation of the underlying base and subgrade layers which occurs over time. Therefore, the earliest stable corner deflection values were used.

For example, for Section 524FD, using known design inputs and ISLAB2000, corner deflections are calculated as a function of temperature differential in the slab, as shown in Figure 30. The HVS corner deflections for the section, measured at various load repetitions, are shown in Figure 31. The point on the graph, denoted by the darker black circle, was used as the data point for estimating effective linear built-in temperature difference. The measured corner deflection at this point is 3400 m $\times 10^{-6}$, which corresponds to a temperature differential of -30.2ºC, as shown in Figure 30. After accounting for the measured temperature differential in the slab, the effective linear built-in temperature difference for Section 524FD is estimated as -28.5ºC.

Using the above analysis technique, the effective linear built-in temperature difference for the South Tangent sections was calculated. The results are shown in Figure 32. Note that the

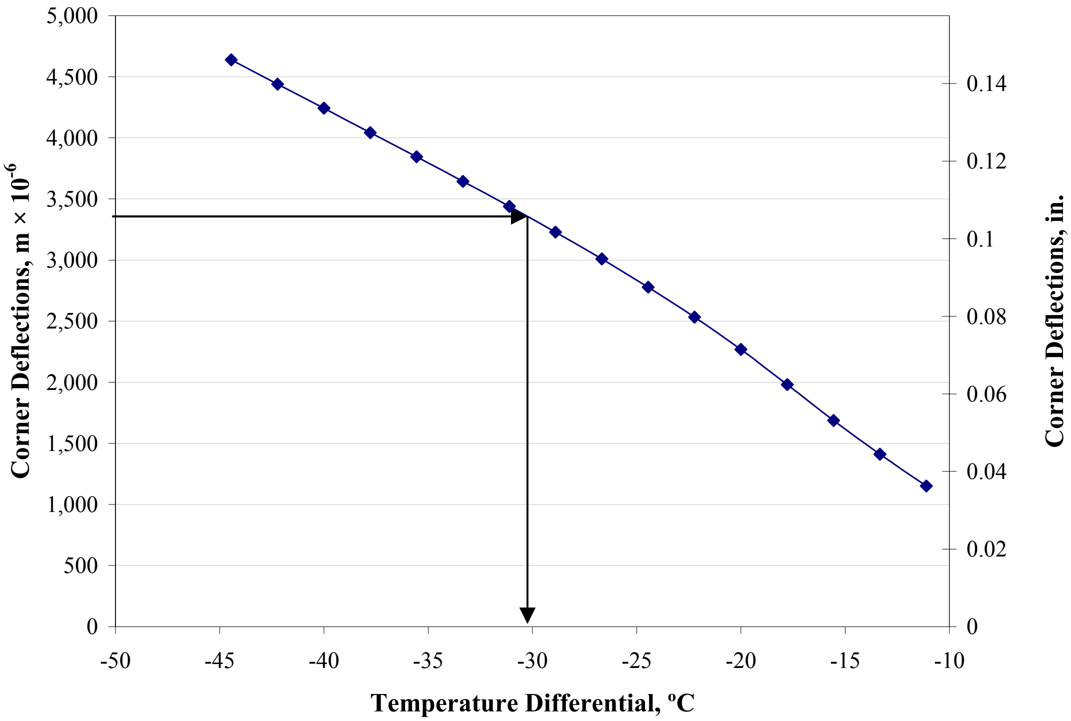

Figure 30. Predicted corner deflections as a function of slab temperature difference for Section 524FD.

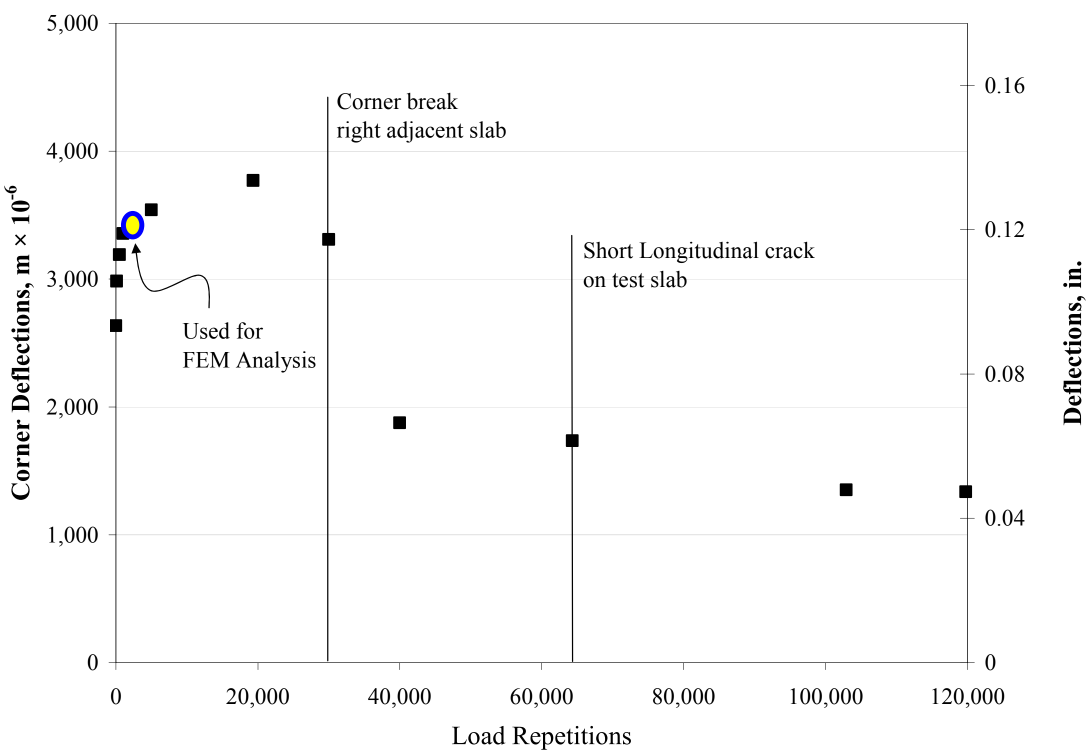

Figure 31. Measured corner deflections for Section 524FD.

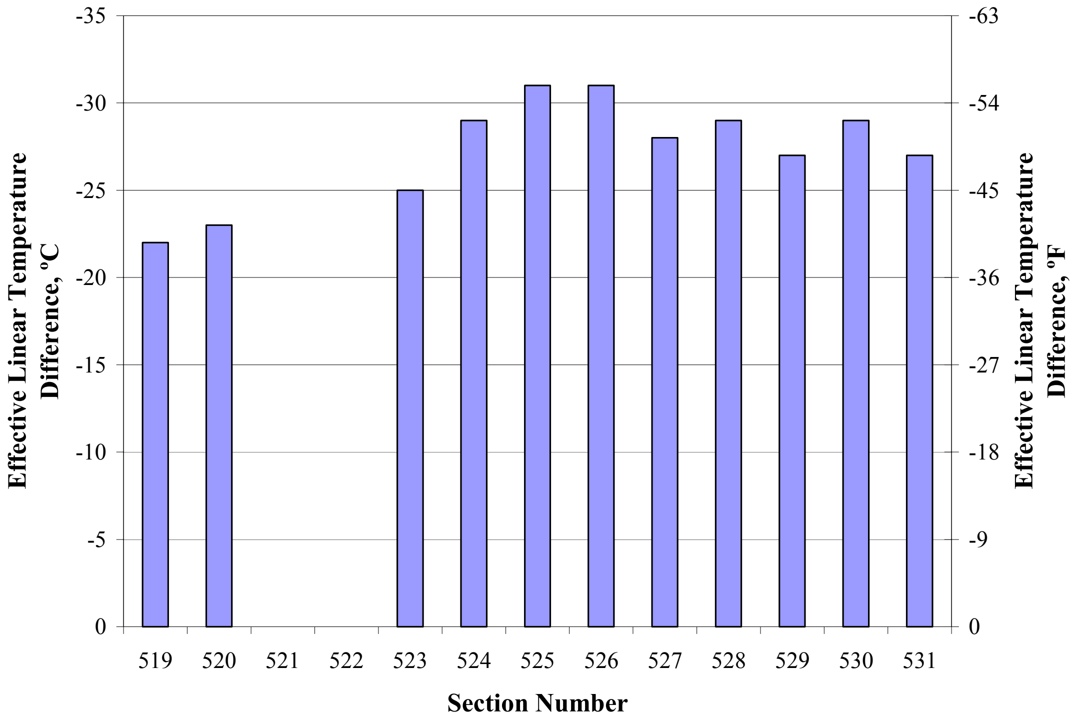

Section 521: Unusually high deflections
Section 522: Static edge loading (no corner loading)

Figure 32. Estimated effective linear built-in temperature difference for South Tangent sections.

FEM analysis assumes static loading whereas the South Tangent slabs were tested at creep speeds.

4.5 Curling of Unloaded Slab Due to Ambient Temperature

The 24-hour corner deflection of Slab 39 (Section 530FD) was measured using JDMDs over a period of several days under environmental loading conditions only. Thermocouples installed in the slab were used to measure the temperature distribution through the slab. Figure 33 shows the variation in slab temperature difference and corner deflections due to the daily fluctuation in ambient air temperature.

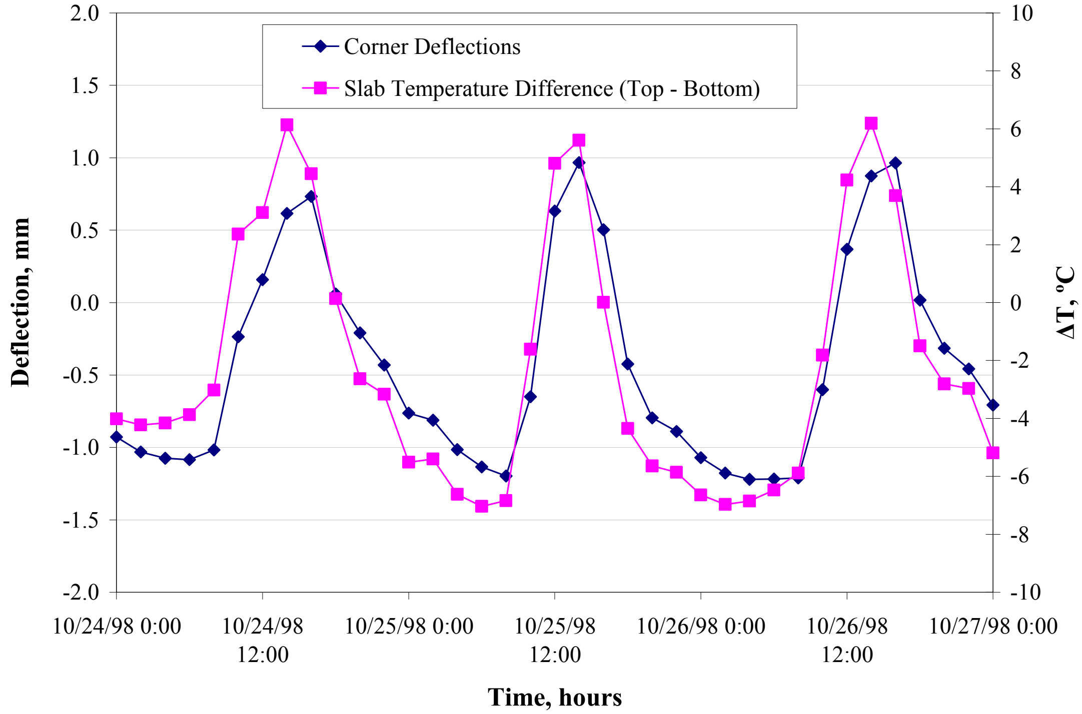

Figure 33. Cycling of slab temperature difference and corner deflections under ambient conditions.

Using a finite element analysis (FEM) program (ISLAB2000), the slab corner deflections due to temperature distribution only in the slab can be calculated. Figure 34 shows the results of this analysis assuming zero effective built-in temperature difference in the slab. Because the measured deflections do not have a reference value, it is important to compare the range of the measured deflections to the range of the prediction deflections rather than the actual values. As can be seen from the figure, the range of the measured deflections is significantly higher than that of the predicted deflections. The predicted deflections of the slab are low when a zero effective built-in gradient is assumed since the corners are initially supported. To match the range of the measured deflections, the FEM calculations should be performed with a negative effective built-in temperature difference, which is equivalent to a void beneath the slab corner resulting in higher deflections.

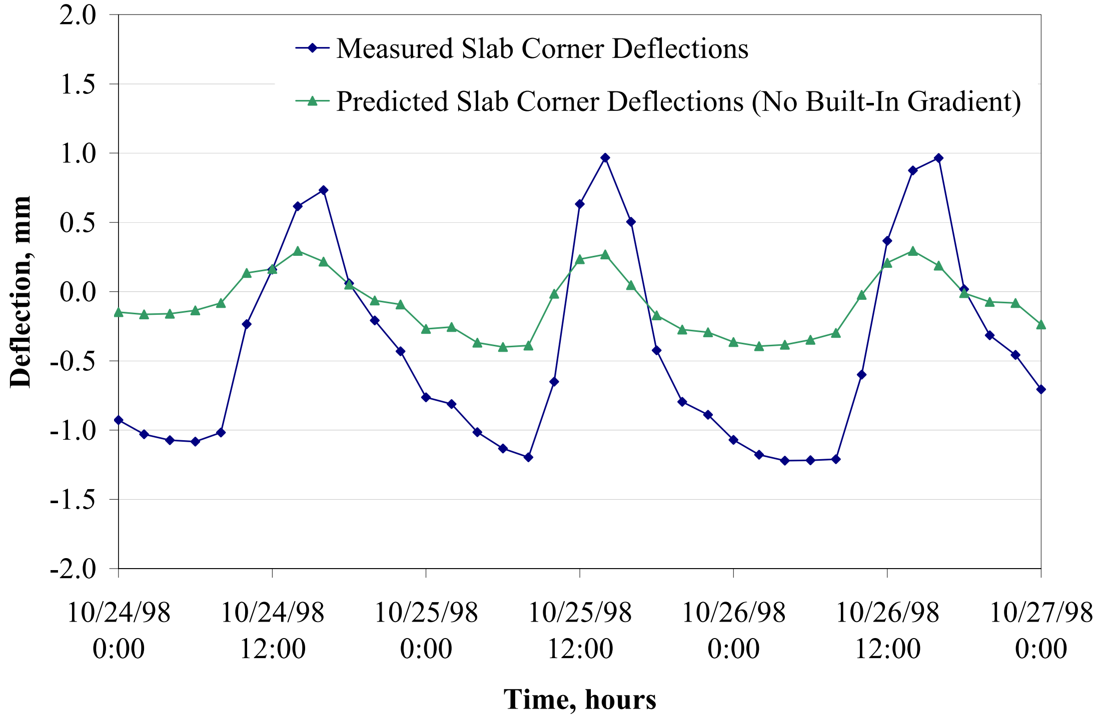

Figure 34. Predicted unloaded slab corner deflections assuming zero built-in temperature difference versus measured deflections under ambient conditions.

Because the thermocouple sensor was not located exactly on the surface of the slab, the thermocouple data has to be extrapolated to account for the difference in temperature between the sensor location and the surface of the slab. The temperature change in the top one inch of the slab can be highly nonlinear, particularly at the most critical times (when the surface of the slab is the hottest, typically around 2:00 p.m., and when the surface of the slab is the coldest, typically around 4:00 a.m.). As shown in Figure 35, this nonlinearity has a significant effect on the range of unloaded slab deflection. Figure 35 shows the effect of built-in slab curling on the range of slab movement under ambient conditions and various surface temperature nonlinearity gradient ratios. As shown in the figure, when the nonlinearity ratio is 4:1 (the rate of change of temperature on the top 25 mm [1 in.] of the slab is 4 times that of the next 50 mm [2 in.]), the range of the calculated deflections is equal to that of the measured JDMD deflections for effective built-in temperature differences less than –17ºC (–30ºF).

Note that the deflection range shown in Figure 35 is approximately the same for all built-in effective temperature differences less than –17ºC (–30ºF). This implies that for an unloaded slab under the influence of daily temperature cycling (as shown in Figure 33), it is not possible to determine effective linear built-in gradients of less than –17ºC (–30ºF) using deflection range only and without using a reference point relative to flat slab condition. This is because for built-in effective temperature differences more negative than–17 ºC (-30 ºF), the slab corners never come in contact with the base/subbase, even at the warmest temperatures (most positive thermal gradients) thus resulting in similar deflection ranges. This analysis suggests that the effective linear built-in gradient due to the combination of construction curling and moisture warping is more negative than –17ºC (–30ºF), but the precise value cannot be determined using unloaded slab deflection values.

Figure 36 shows the comparison of predicted unloaded slab corner deflections assuming –17ºC (–30ºF) built-in effective temperature difference versus measured deflections. Note that this figure is similar to those assuming –22ºC (–40ºF), –27ºC (–50ºF), or –33ºC (–60ºF) because of the similar deflection ranges for all built-in effective temperature differences more negative than –17ºC (–30ºF).

4.6 Effect of HVS Shading on Thermocouple Data

The measured slab temperature data used in the analysis is from the thermocouples that are installed in the test slab. The portion of the slab tested was enclosed in a temperature control box (excluding sections 522FD, 525FD, and 527FD). As a result, the slab temperatures measured using the thermocouples did not vary significantly from the top of the slab to the

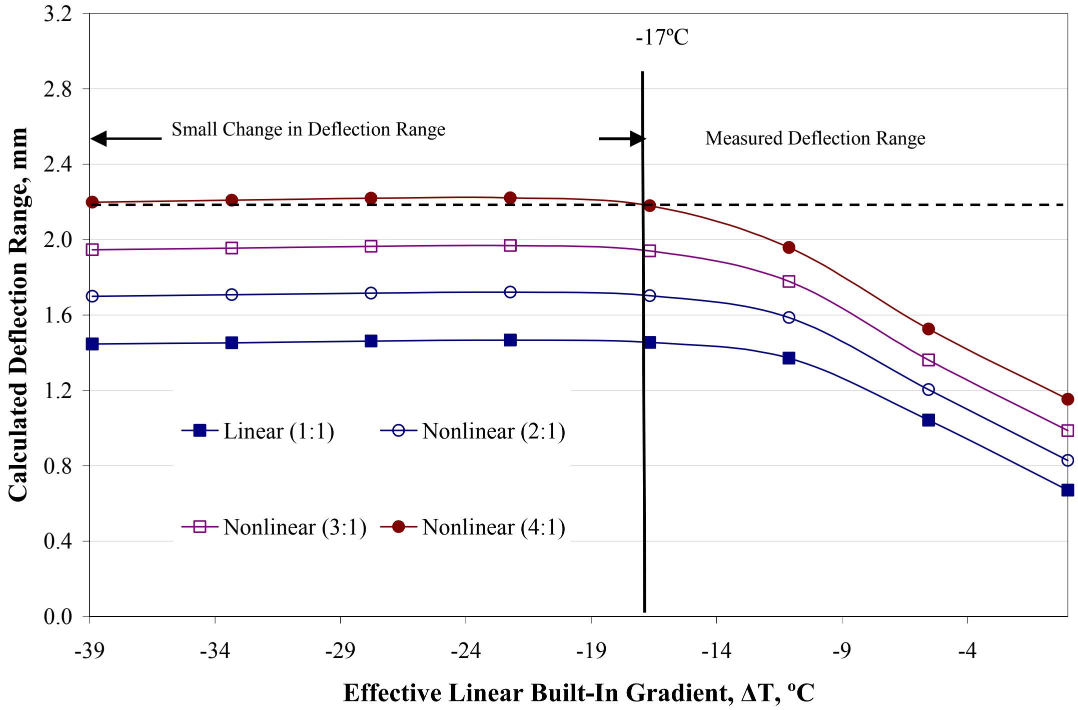

Figure 35. Effect of built-in gradient and slab surface nonlinearity ratio on predicted slab deflections.

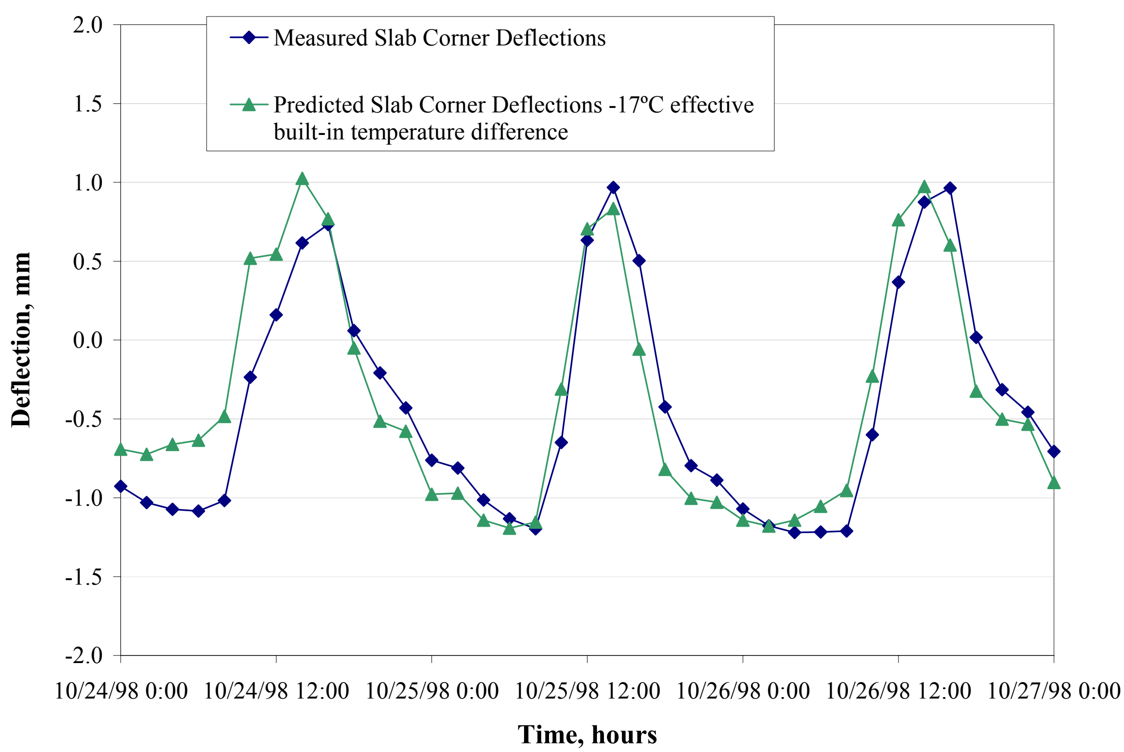

Figure 36. Predicted unloaded slab corner deflections assuming zero built-in temperature difference versus measured deflections under ambient conditions.

bottom of the slab. However, analyses of the North Tangent test sections show that the temperatures (air temperature, slab temperature, shade, etc.) that are outside the temperature control box affect slab responses measured inside the temperature control box. This is because a portion of the slab is exposed to ambient conditions outside the HVS and is subject to changes in weather, sunlight, HVS shadows, etc. These effects need to be accounted for in the analyses of the South Tangent test sections. This will be done after an extensive analysis of the North Tangent test sections, where more detailed and comprehensive information was collected.

5.0 CRACKING ANALYSIS

The objective of the cracking analysis is to evaluate slab cracking by attempting to understand the stress state of the slab. This section includes:

- Discussion of the mechanism of fatigue cracking and responses at critical locations.
- Influence diagrams for South Tangent sections representing the stresses at the top of the concrete slab simulating the effect of a load moving in a given direction (left to right) on a fixed point.
- Discussion of fatigue characterization of concrete pavements and various fatigue models.
- Calculation of fatigue damage to failure using various models for South Tangent sections.
- Comparison of predicted versus actual locations of critical damage for South Tangent sections.

5.1 Fatigue Cracking

Cracking in concrete pavements occurs as a result of either early-age environmental stresses with or without load stresses that exceed the concrete strength of the slabs or fatigue failure. The environmental stresses are caused by the combined effects of the restraint forces (the restraint against the contraction of concrete in response to either shrinkage or temperature change), thermal curling, and moisture warping. Most of the cracking from these mechanisms occurs soon after construction. Several slabs at the Palmdale test site cracked due to high stresses which occurred at early age and before the concrete had not gained adequate strength. Details of this type of early-age cracking at Palmdale are discussed in Reference (*7*).

Fatigue cracking is a key measure of concrete pavement performance and is caused by the repeated application of traffic and environmental loading at stress levels less than the cracking strength of the concrete. As the loadings are repeated over time, cracking can occur in the slab. Analysis of fatigue cracking includes determination of critical stresses in the slab (both traffic and environmentally induced) and the locations of these stresses. These stresses are used in a fatigue cracking model that relates stresses and number of load applications to damage at the location of critical stress.

5.2 Critical Stresses in Concrete Slabs

Each application of traffic and environmental load on a pavement results in stresses that occur in the concrete slab. The consequence of these stresses is an accumulation of damage in that portion of the concrete slab. After sufficient damage has accumulated in a region of the concrete slab, cracking will be visible on the surface of the slab. Fatigue cracking in jointed plain concrete pavement (JPCP) can be divided into four major categories depending on the location of the accumulated damage and can be further reviewed in References (*8, 9*):

- Bottom-up transverse cracks.
- Top-down transverse cracks.
- Longitudinal cracks.
- Corner breaks.

5.2.1 Mechanism of Bottom-Up Transverse Cracking

When loads are near the longitudinal edge of the slab, midway between the transverse joints, a critical tensile bending stress occurs at the bottom of the slab, as shown in Figure 37.

This stress increases greatly when there is a high positive thermal gradient through the slab (top of the slab is warmer than bottom of the slab). Repeated heavy loadings result in fatigue damage along the edge of the slab, which results in microcracks that propagate to the slab surface from the bottom and transversely across the slab.

5.2.2 Mechanism of Top-Down Transverse Cracking

When the load is near the transverse joints at the corner of the slab, a high tensile stress occurs at the top of the slab between the axles, some distance from the joint, as shown in Figure 38. This stress increases greatly when there is a negative thermal gradient through the slab, a built-in negative gradient from construction, and/or a significant drying shrinkage at the top of the slab. Repetitive loading results in fatigue damage at the top of the slab, which eventually results in micro-cracks that propagate downward through the slab and transversely or diagonally across the slab. As in the case of bottom-up cracking, these micro-cracks join and result in a transverse crack that is visible on the surface of the slab.

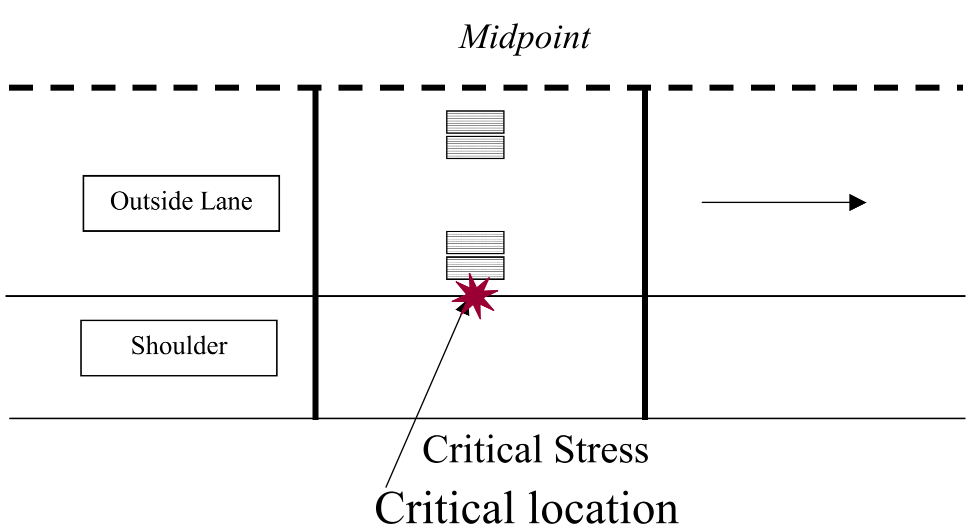

Figure 37. Critical load and structural response location for JPCP bottom-up transverse cracking.

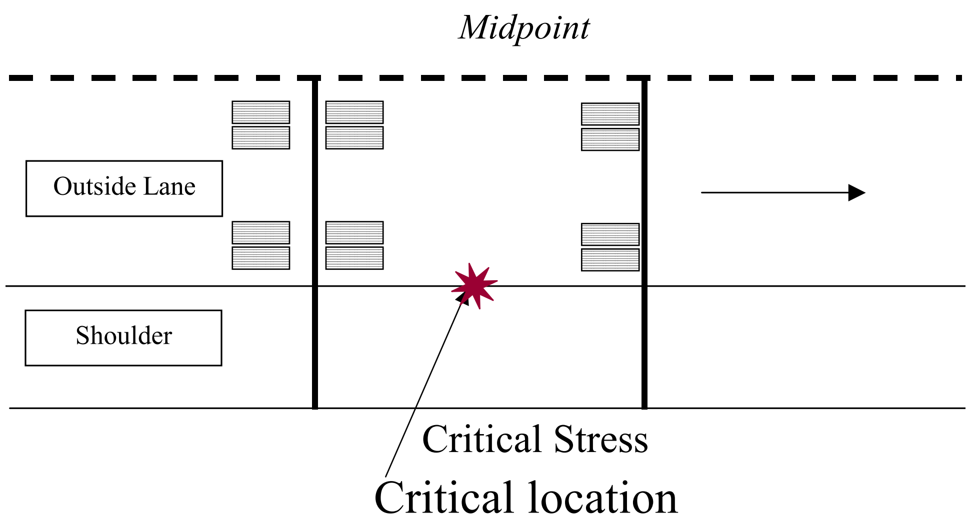

Figure 38. Critical load and structural response location for JPCP top-down transverse cracking.

5.2.3 Longitudinal Cracks and Corner Breaks

One mechanism for longitudinal cracks and corner breaks with edge loading conditions caused by fatigue is similar to that for top-down cracking; the difference is the location of the critical stress, as shown in Figures 39 and 40. A high tensile stress occurs at the top of the slab, which increases greatly when there is a negative thermal gradient through the slab, a built-in negative gradient from construction, or significant drying shrinkage at the top of the slab. Repeated heavy loading results in fatigue damage at the top of the slab at a transverse joint, which eventually results in micro-cracks that propagate downward through the slab and longitudinally or diagonally across the slab. Note that longitudinal cracks can also originate from the bottom of the slab; however, this is not typical for the half-axle HVS edge load.

5.3 Responses at Critical Locations

All of the slabs on the South Tangent had very high effective linear built-in temperature differentials due to high differential shrinkage occurring within the concrete slab.(*4, 7*) In

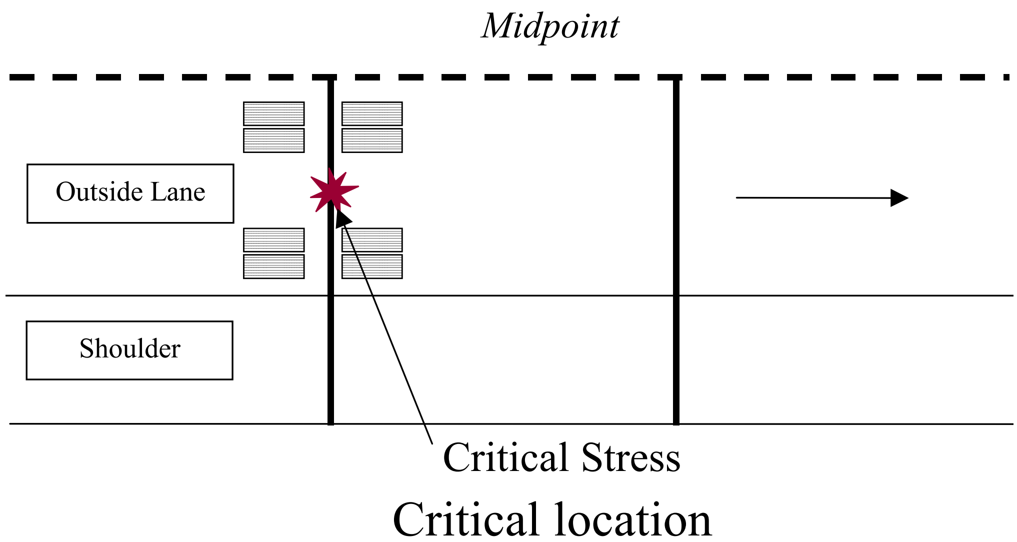

Figure 39. Critical load and structural response location for JPCP longitudinal cracking.

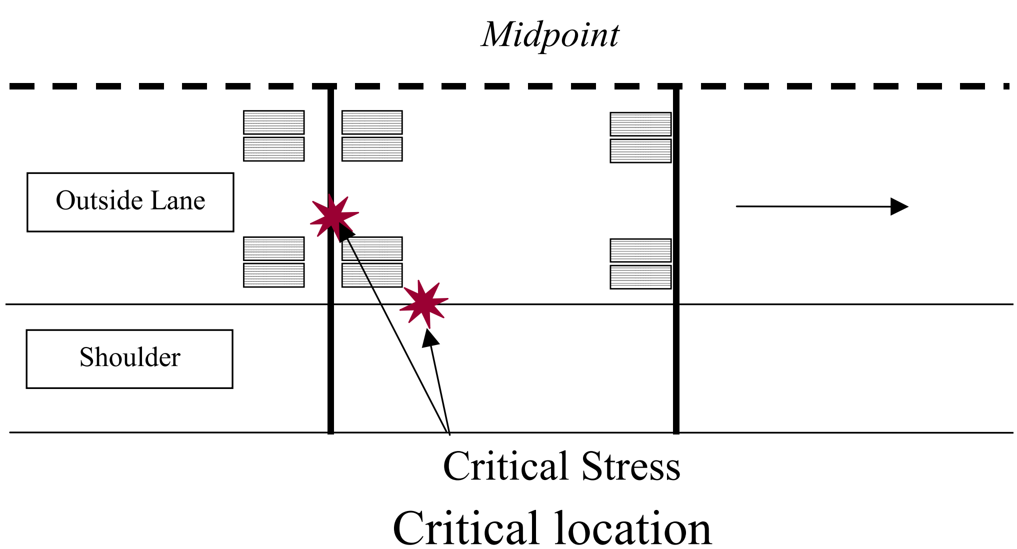

Figure 40. Critical load and structural response location for JPCP corner breaks.

addition, the HVS loading was performed with the slab covered in a temperature box for a majority of the sections, which resulted in very small temperature differentials between the surface of the slab and the base. As a result, throughout the loading cycles, the slabs had a high effective temperature difference, resulting in an upward (concave) curl of the slab. Therefore for the South Tangent test sections at Palmdale, only stresses at the top of the slab are critical and the most likely failure modes will be corner breaks and longitudinal cracks.

Figure 41 shows the transverse stress distribution (responsible for longitudinal cracking) due to a 25-kN (5,600-lb.) load at the top of Section 520FD calculated using a finite element program, ISLAB2000. Figure 42 shows the transverse stress distribution for the same section without the load. The longitudinal stress distributions (responsible for transverse cracking) are shown in Figures 43 and 44. The loaded and unloaded deflections are shown in Figure 45 and 46.

5.4 Early-Age Cracking

Figures 41 through 44 show that the midslab tensile stresses at the top of the slab are very high, both in the case of the loaded slab and the unloaded slab. These high tensile stresses that occur without any load are responsible for the early-age cracking of several of the Palmdale test sections.

Two competing factors affect early-age slab cracking. Immediately after construction, concrete gains strength rapidly. However, the rate of strength gain diminishes over time as shown in Figure 4. At the same time, differential shrinkage from the top of the slab relative to the bottom of the slab causes the slab to warp. This warping results in an effective negative temperature gradient through the slab. The warped slab has higher stresses at the top of the slab

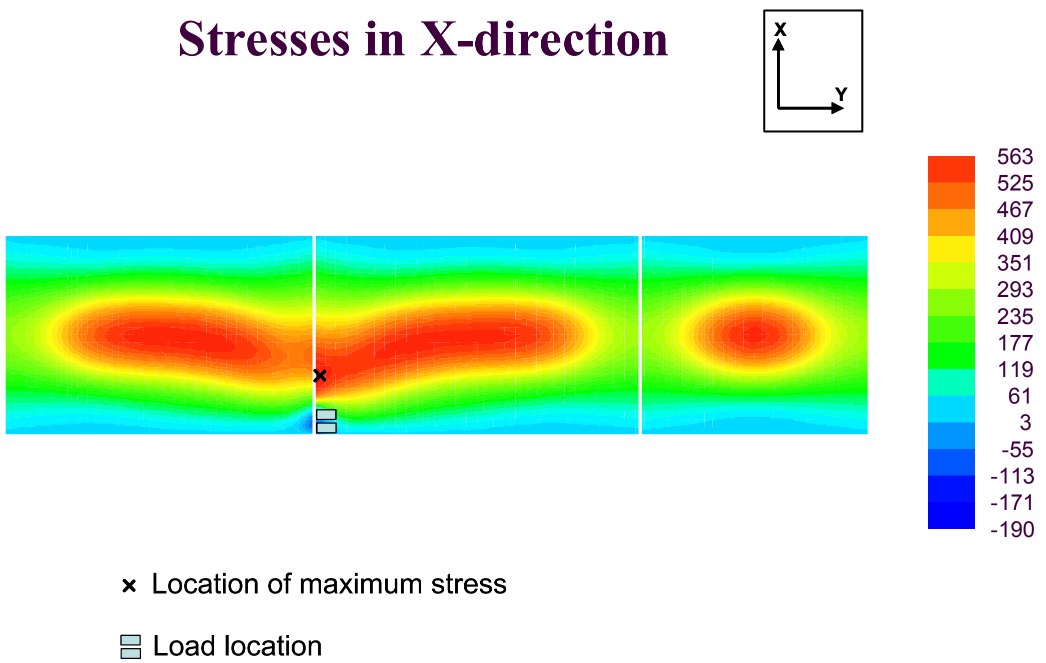

Figure 41. Transverse stress (psi) distribution at top of slab (25-kN [5,600-lb.] load) – Section 520FD.

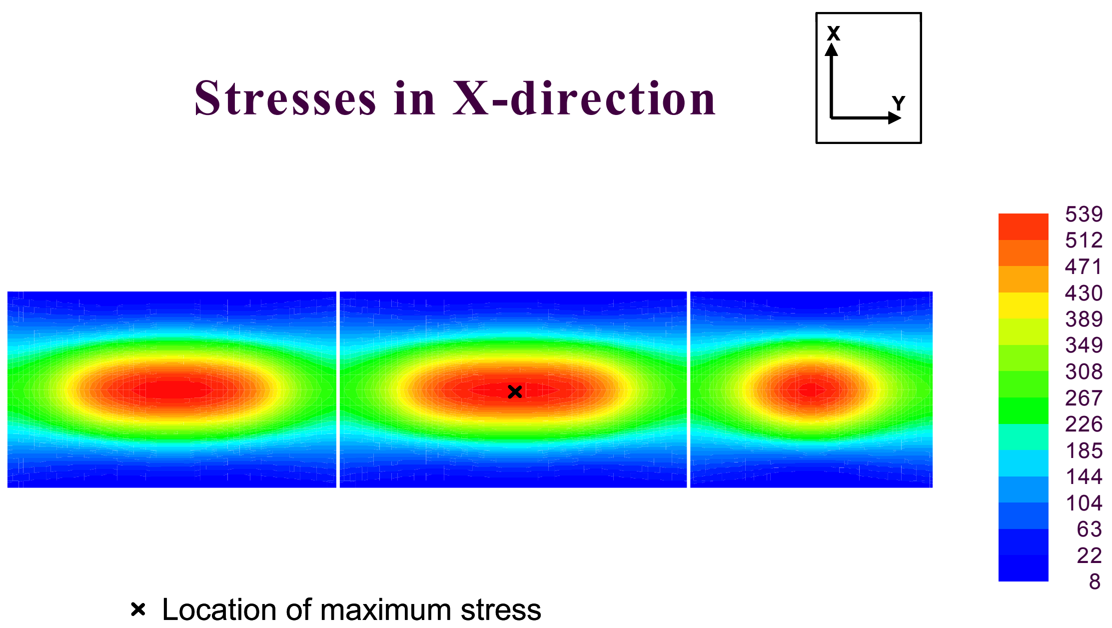

Figure 42. Transverse stress (psi) distribution at top of slab (no load) – Section 520FD.

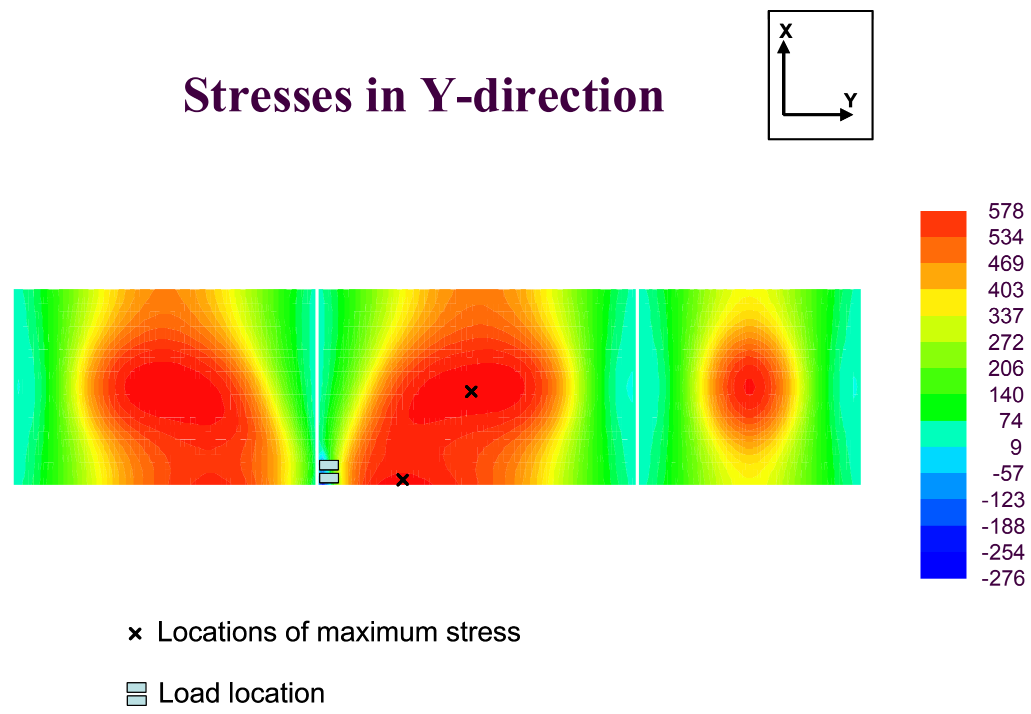

Figure 43. Longitudinal stress distribution (psi) at top of slab (25-kN [5,600-lb.] load) – Section 520FD.

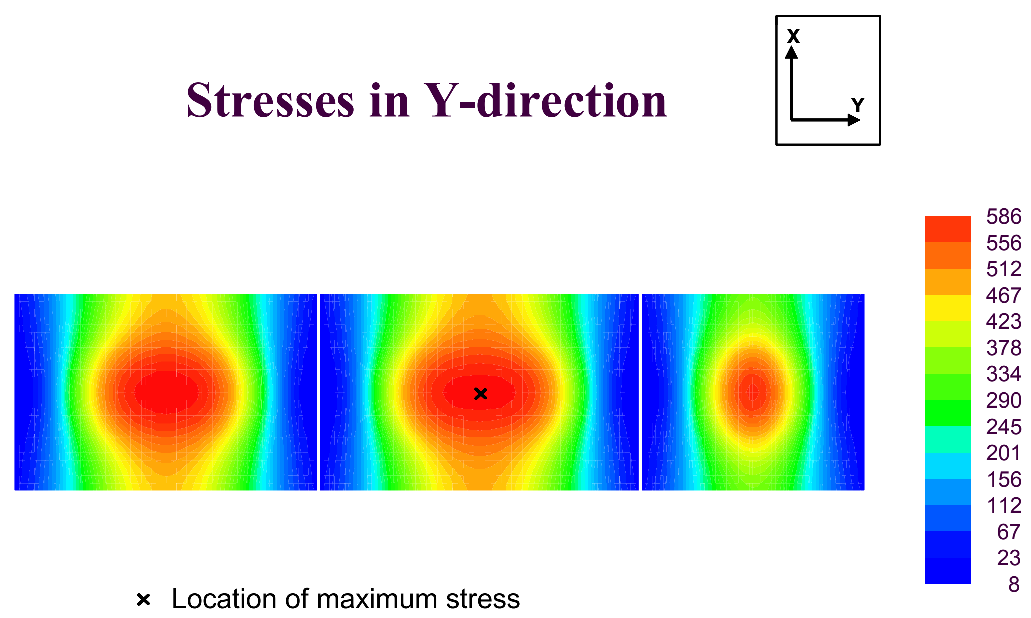

Figure 44. Longitudinal stress distribution at top of slab (no load) – Section 520FD.

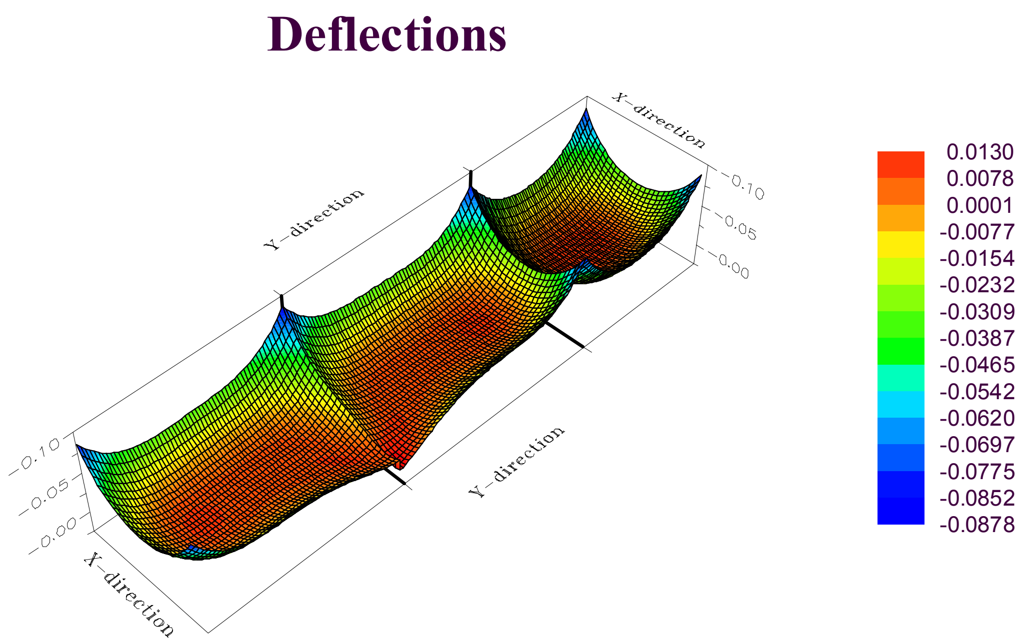

Figure 45. Slab deflection (in.) (25-kN [5,600-lb.] load) – Section 520FD.

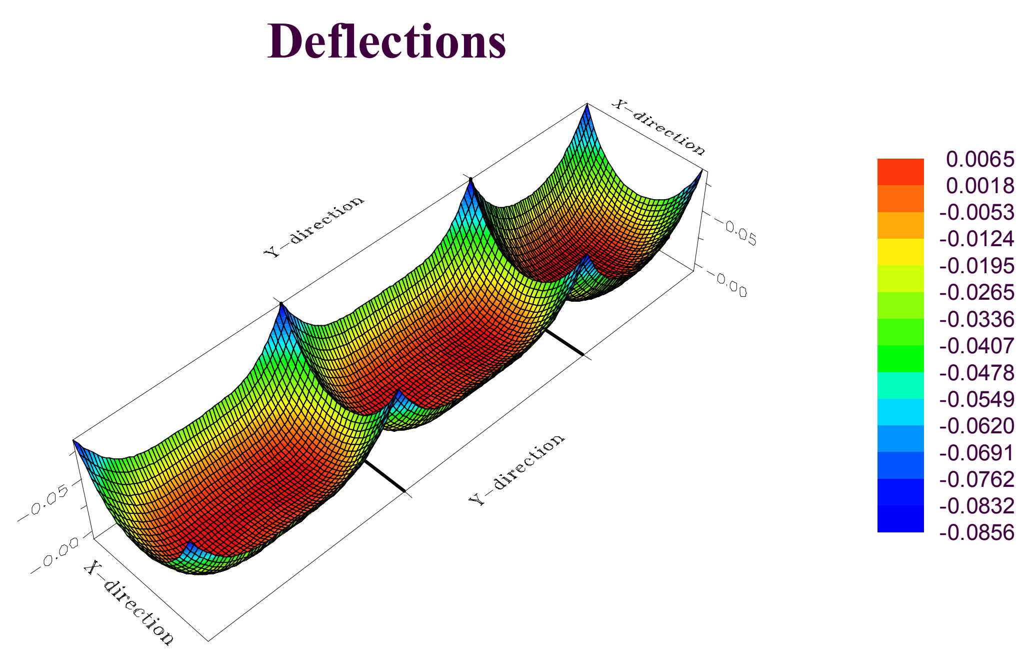

Figure 46. Slab deflection (in.) (no load) – Section 520FD.

caused by the weight of the lifted slab corners (and edges). This is shown in Figures 42 and 44, where high stresses at the midslab location exist without any applied load. If during the early-age development of the concrete, these warping stresses exceed the strength of the concrete, the slab cracks even before any load is applied.

5.5 Influence of Moving HVS Load

Under the application of the HVS load, the midslab stresses do not change significantly and therefore do not affect the fatigue behavior of the slab. This is illustrated in Figure 47, which shows the influence chart for a moving HVS load applied at the edge of the slab for the 100-mm nominal thickness section, 520FD. An influence chart is a graphic representation of a response (stress) at a fixed point due to placement of a load at several different points thus simulating the effect of a load moving in a given direction (left to right) on that fixed point.

Figure 47 shows 4 influence lines denoting stresses at the top of the slab as predicted at 4 locations on the slab including:

- Transverse stress (at critical location on transverse joint) responsible for longitudinal fatigue cracking and corner breaks originating from the transverse joint (A).
- Longitudinal stress (at critical location on slab edge) responsible for transverse fatigue cracking and corner breaks originating from the lane-shoulder joint (B).
- Transverse stress (at midslab location) responsible for early-age cracking (C).
- Longitudinal stress (at midslab location) responsible for early-age cracking (D).

Note that the midslab stresses are not significantly affected by the movement of the load (or by the presense/absence of the load). However, the transverse stresses measured at the transverse joint and the longitudinal stresses measured at the slab edge can vary considerably

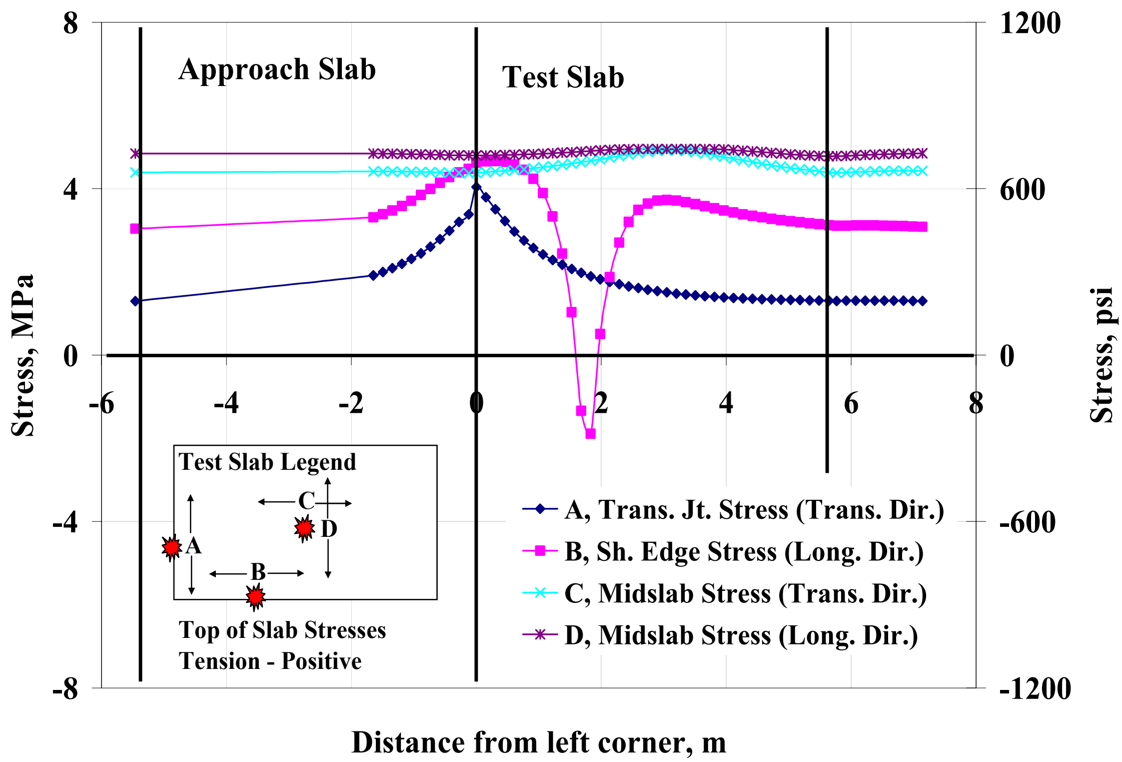

Figure 47. Influence diagram showing effect of 35-kN moving load on stresses at critical locations on the concrete slab (Section 520FD – 100 mm slab).

relative to the unloaded slab as shown in Figure 47. It is assumed that stress changes cause fatigue as opposed to peak tensile stress.

Figures 48 through 65 show the influence lines denoting the following stresses at the top of the slab with positive values representing tensile stresses and negative values representing compressive stresses:

- Transverse stress (at critical location on transverse joint) responsible for longitudinal fatigue cracking and corner breaks originating from the transverse joint (A) for three values of effective linear temperature difference in the slab.
- Longitudinal stress (at critical location on slab edge) responsible for transverse fatigue cracking and corner breaks originating from the lane-shoulder joint (B) for

three values of effective linear temperature difference in the slab. Note that each influence line corresponding to each of the three effective linear temperature difference taken at different points on the slab. This is because the critical point (point with the greatest tensile stress) changes depending on the magnitude of the effective linear temperature difference.

The influence lines are shown for Sections 520FD (100-mm nominal thickness), 524FD (150-mm nominal thickness), and 530FD (200-mm nominal thickness), for three different load levels, 35 kN (7,875 lbs.), 20 kN (4,500 lbs.), and 60kN (13,500 lbs.), and three effective temperature differences, 100 percent of estimated built-in curl, 50 percent of estimated built-in curl, and zero (no slab temperature difference). The following conclusions can be drawn from these influence lines:

- The effective temperature difference in the slab has a significant effect on the peak stress for both the critical transverse joint location (A) and the critical slab edge location (B). However, the exact location of the peak stress depends on the magnitude of the temperature difference (Figures 48 and 49). The larger the temperature difference, the greater the uplift at the slab corners, and farther away from the corner and closer to the midslab edge is the location of the peak stress.
- Depending on the magnitude of the temperature difference, the location of the peak stress can vary up to 2 m relative to the peak stress location during flat slab (zero temperature difference) condition (Figures 49, 51, and 53). This variation is smaller along the transverse joint (A) and larger along the slab edge (B).

- The critical location on the slab edge (B) typically experiences a stress reversal, i.e. the stress changes from tension to compression and back to tension under the influence of a moving load (Figures 49, 51, and 53).
- The magnitude of the stress reversal depends on the slab thickness and the magnitude of the applied load. In cases when the load is small or the slab thickness is large, there is no stress reversal (Figure 57).
- Both the magnitude of the applied load and the thickness of the slab significantly affect stresses in the slab, but not the shape of the stress influence line.

The results of the influence chart analysis for the three sections are summarized in Tables 10 and 11.

5.6 Fatigue Characterization of Concrete Pavements

5.6.1 Miner's Hypothesis and Damage Accumulation

Miner's fatigue damage accumulation hypothesis is empirically based and is given as follows (*10*):

$$Fatigue\,Damage = \sum \frac{n_i}{N_i} \tag{2}$$

where

n_i = Number of actual load applications of under conditions represented by i.

N_i = Number of allowable load applications until failure under conditions represented by i.

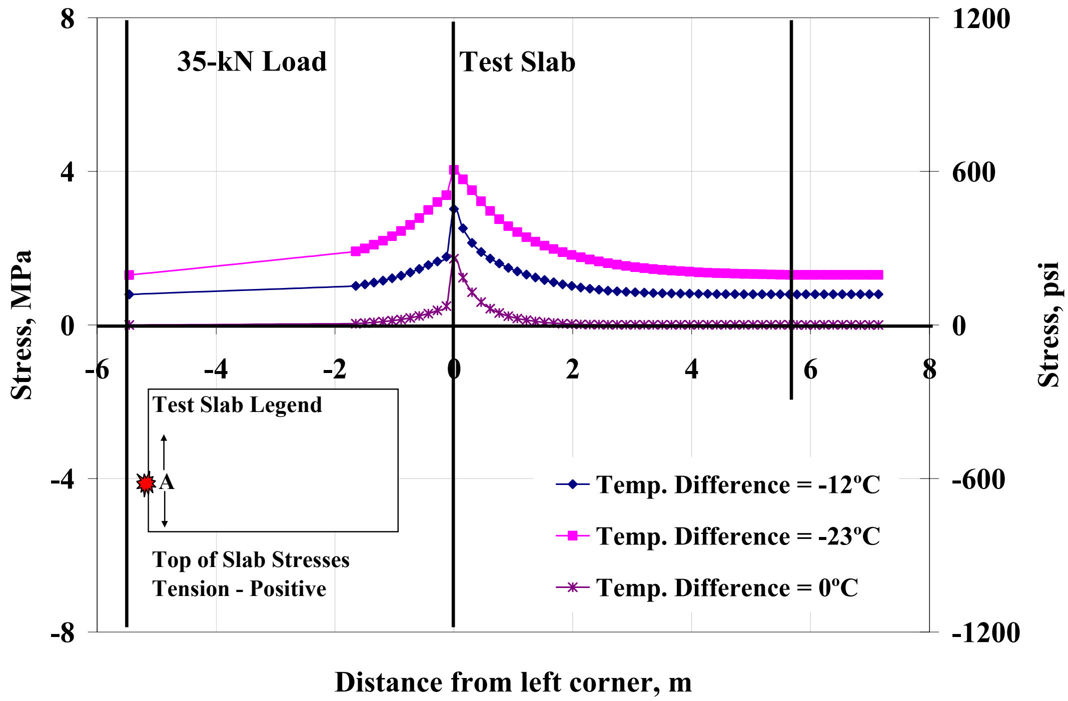

Figure 48. Influence diagram showing effect of 35-kN moving load on transverse stresses at the transverse joint (Section 520FD – 100 mm slab).

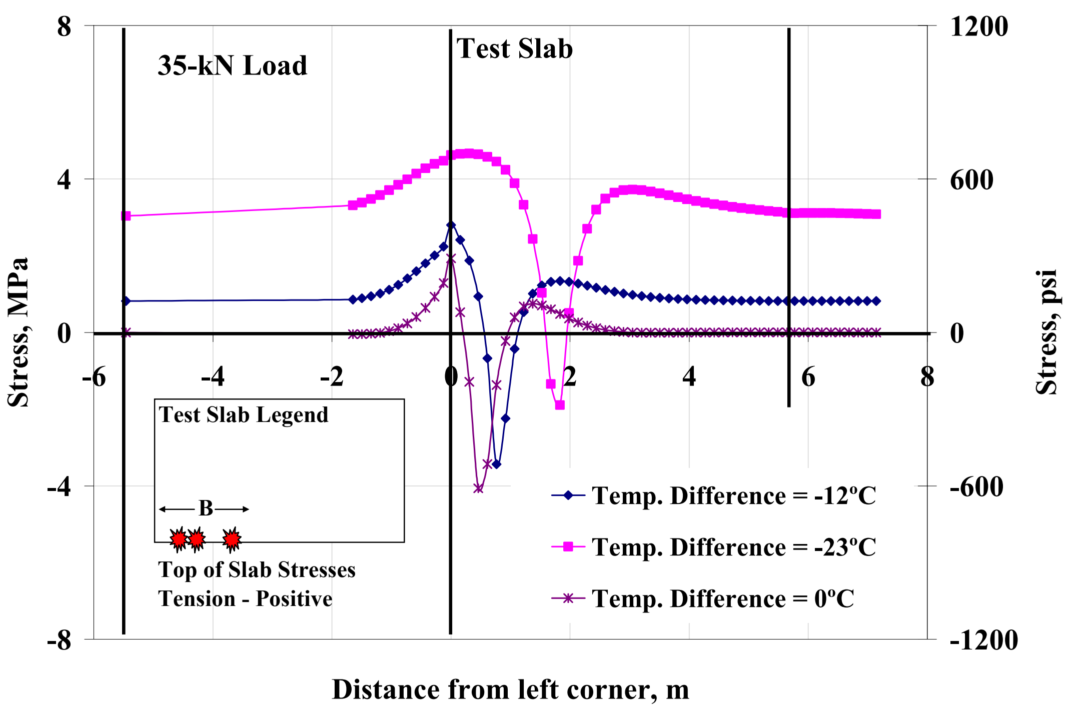

Figure 49. Influence diagram showing effect of 35-kN moving load on longitudinal stresses at the lane-shoulder joint (Section 520FD – 100 mm slab).

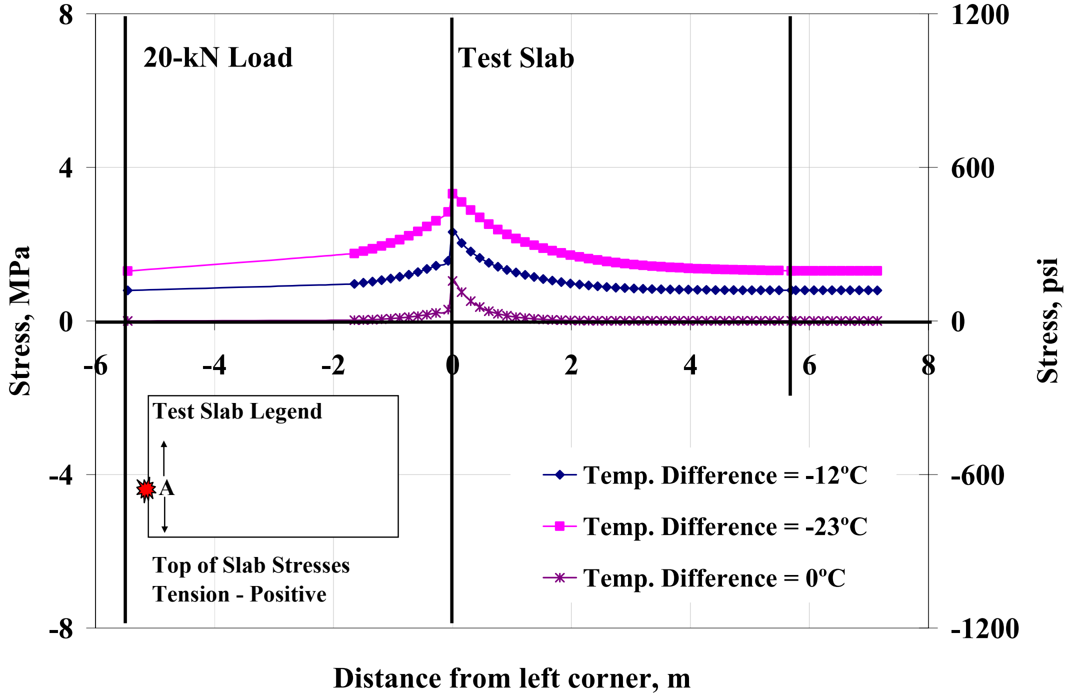

Figure 50. Influence diagram showing effect of 20-kN moving load on transverse stresses at the transverse joint (Section 520FD – 100 mm slab).

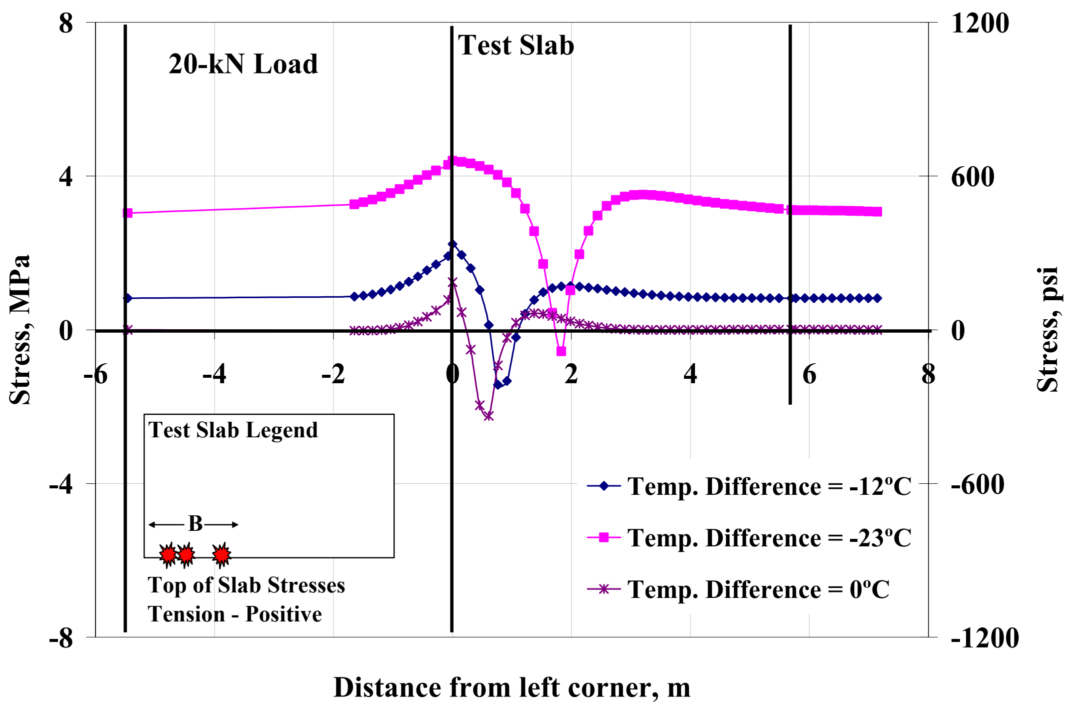

Figure 51. Influence diagram showing effect of 20-kN moving load on longitudinal stresses at the lane-shoulder joint (Section 520FD – 100 mm slab).

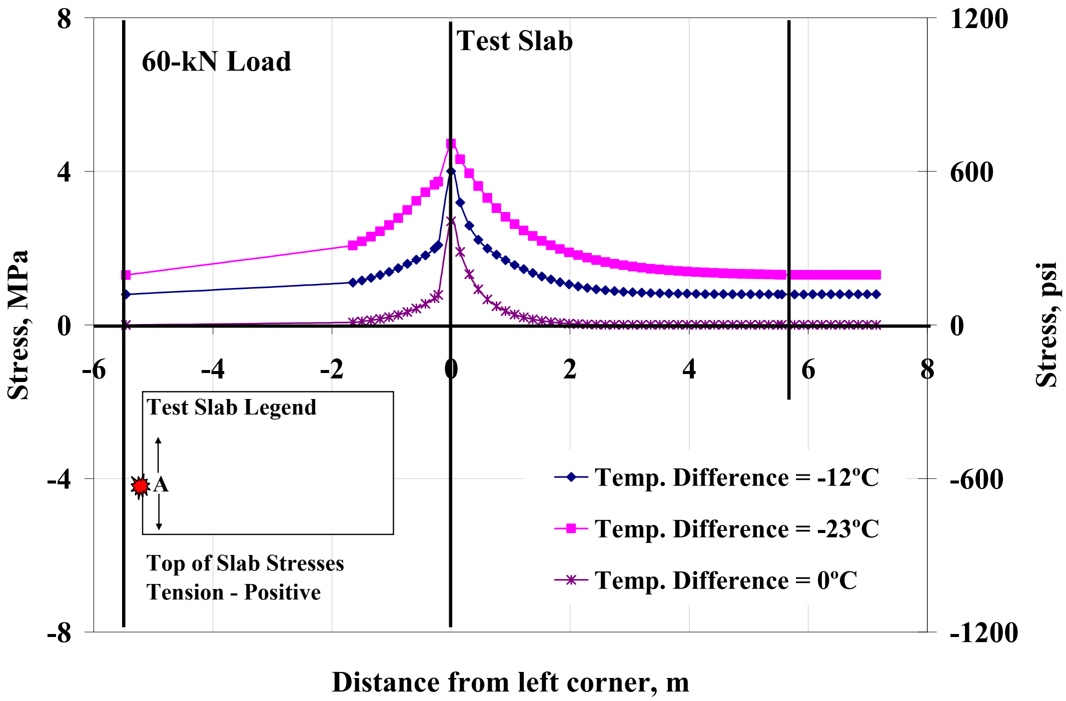

Figure 52. Influence diagram showing effect of 60-kN moving load on transverse stresses at the transverse joint (Section 520FD – 100 mm slab).

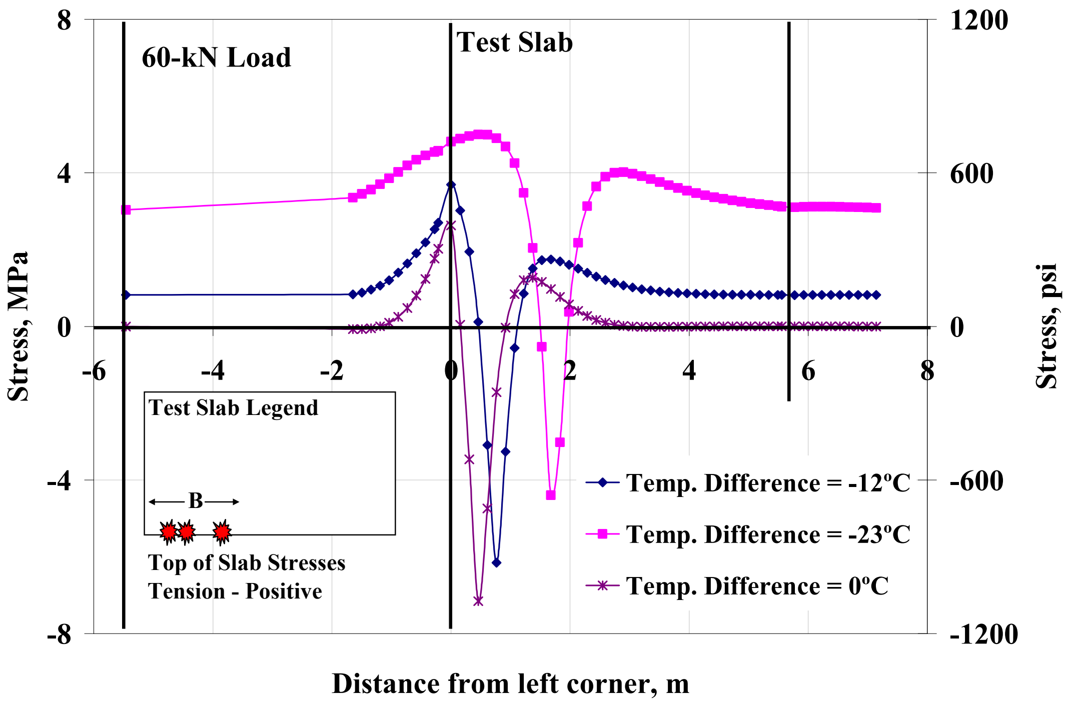

Figure 53. Influence diagram showing effect of 60-kN moving load on longitudinal stresses at the lane-shoulder joint (Section 520FD – 100 mm slab).

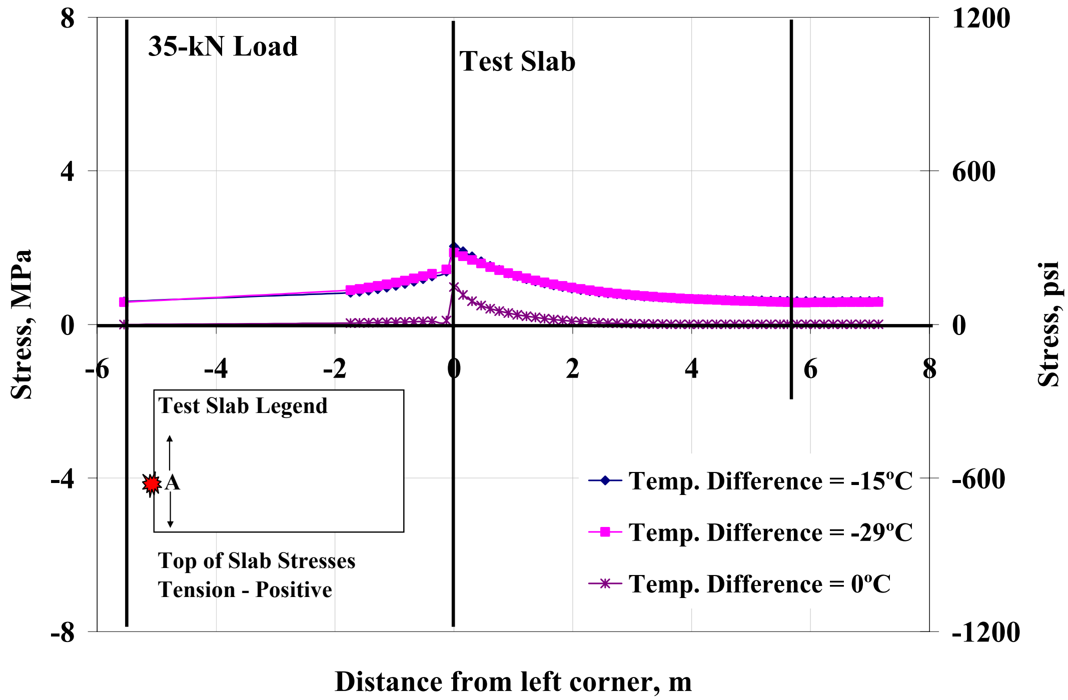

Figure 54. Influence diagram showing effect of 35-kN moving load on transverse stresses at the transverse joint (Section 524FD – 150 mm slab).

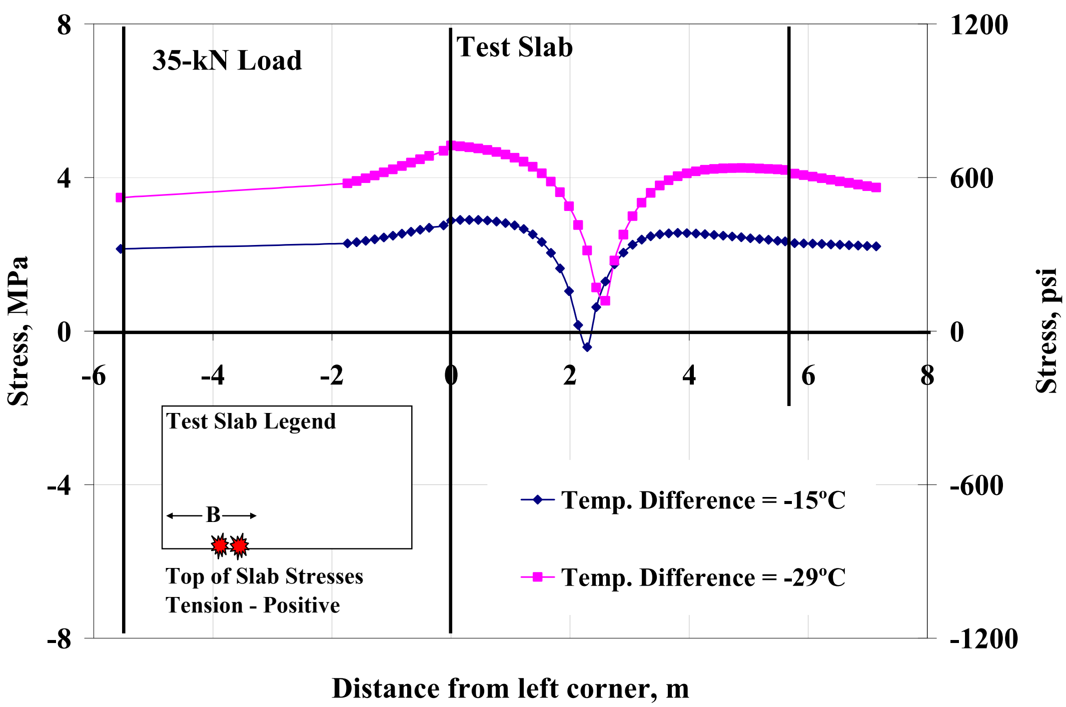

Figure 55. Influence diagram showing effect of 35-kN moving load on longitudinal stresses at the lane-shoulder joint (Section 524FD – 150 mm slab).

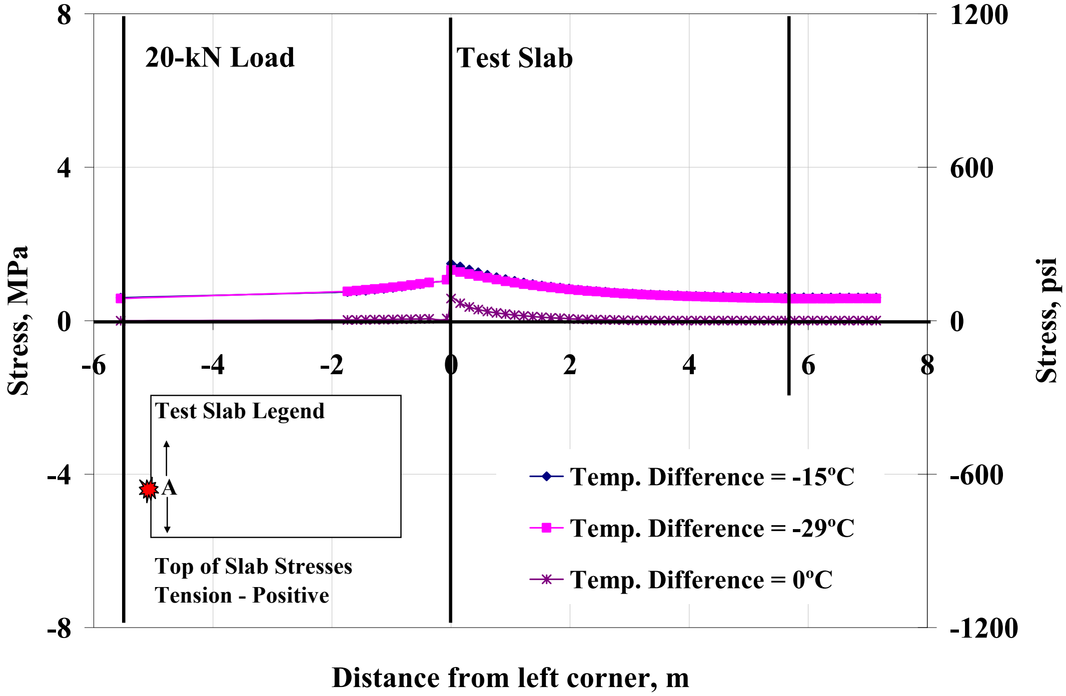

Figure 56. Influence diagram showing effect of 20-kN moving load on transverse stresses at the transverse joint (Section 524FD – 150 mm slab).

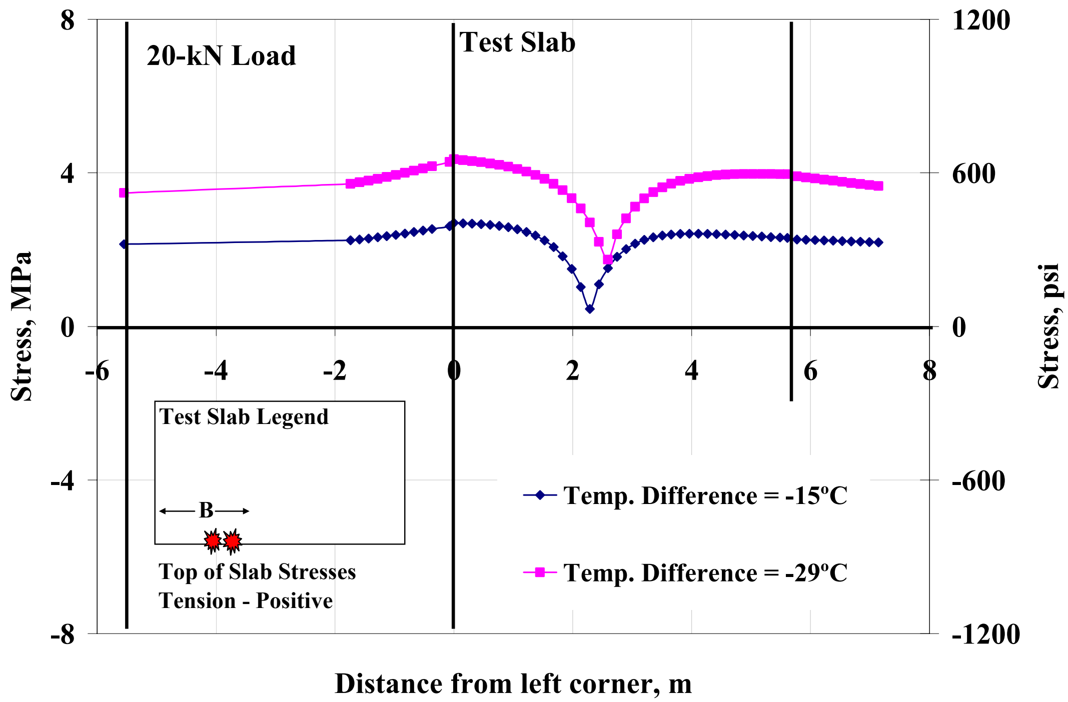

Figure 57. Influence diagram showing effect of 20-kN moving load on longitudinal stresses at the lane-shoulder joint (Section 524FD – 150 mm slab).

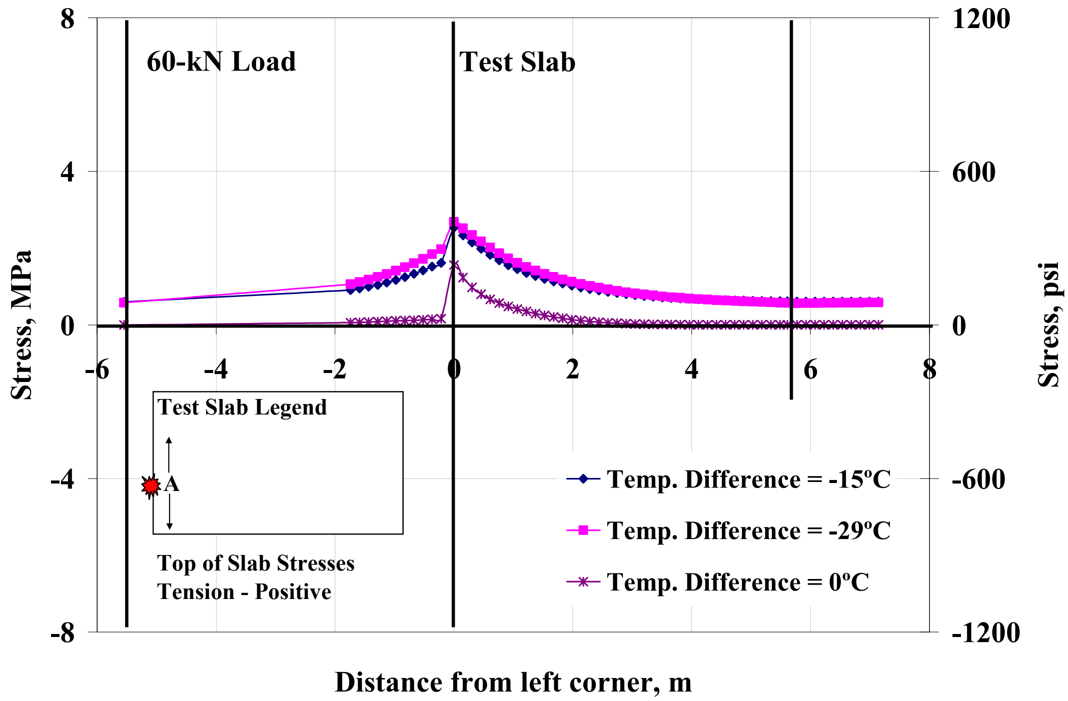

Figure 58. Influence diagram showing effect of 60-kN moving load on transverse stresses at the transverse joint (Section 524FD – 150 mm slab).

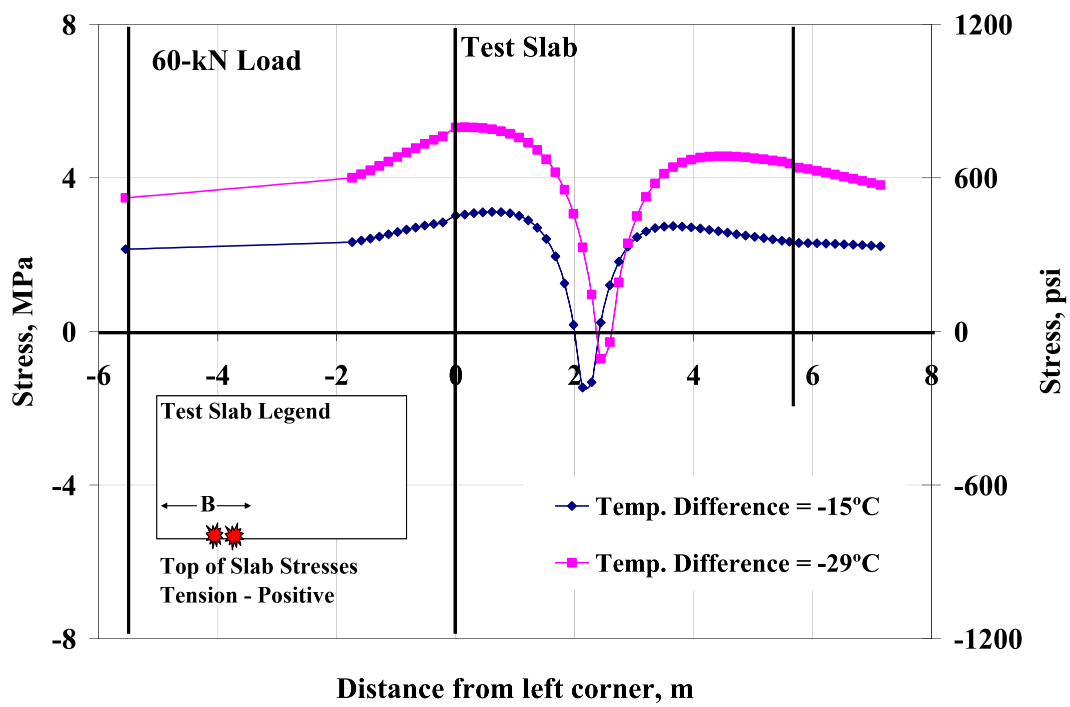

Figure 59. Influence diagram showing effect of 60-kN moving load on longitudinal stresses at the lane-shoulder joint (Section 524FD – 150 mm slab).

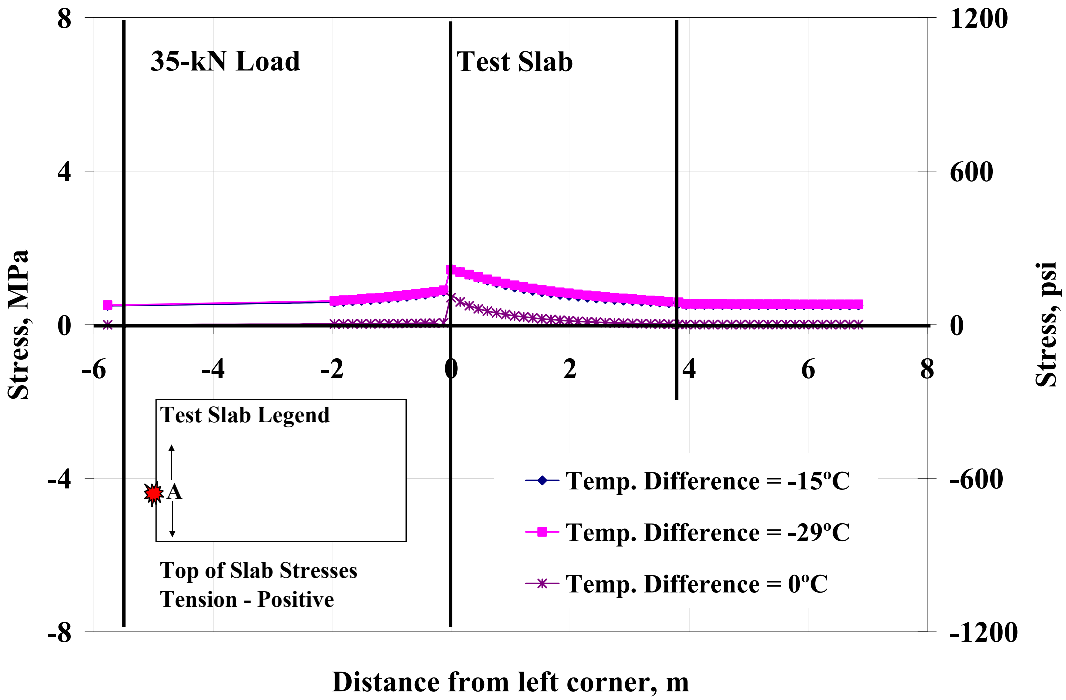

Figure 60. Influence diagram showing effect of 35-kN moving load on transverse stresses at the transverse joint (Section 530FD – 200 mm slab).

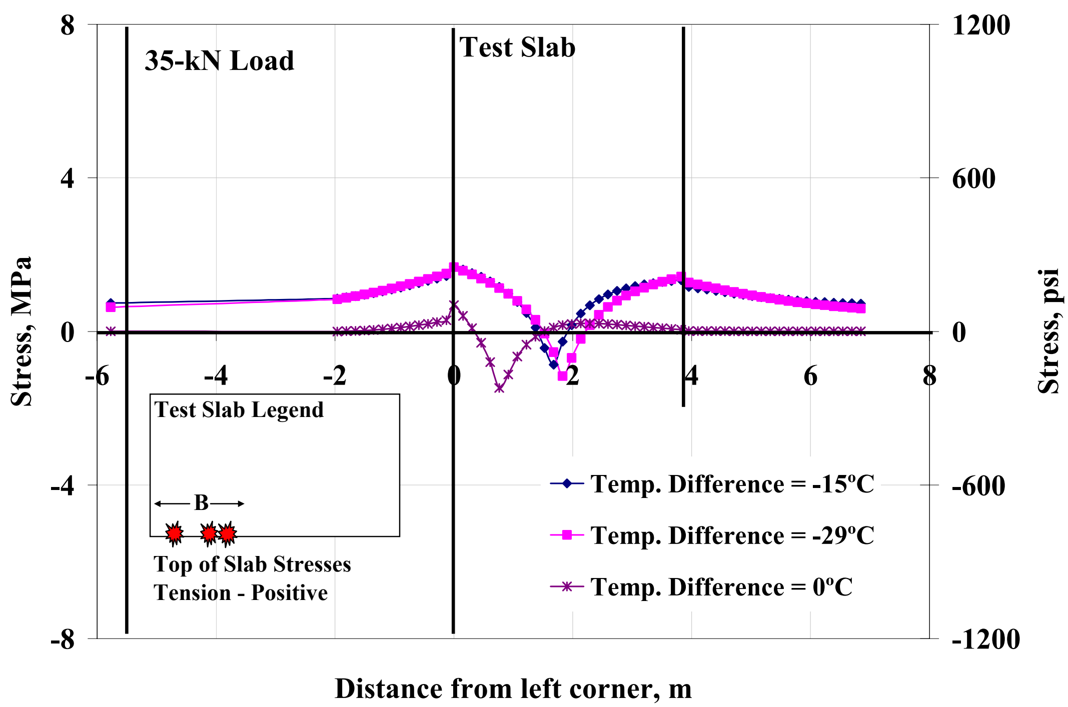

Figure 61. Influence diagram showing effect of 35-kN moving load on longitudinal stresses at the lane-shoulder joint (Section 530FD – 200 mm slab).

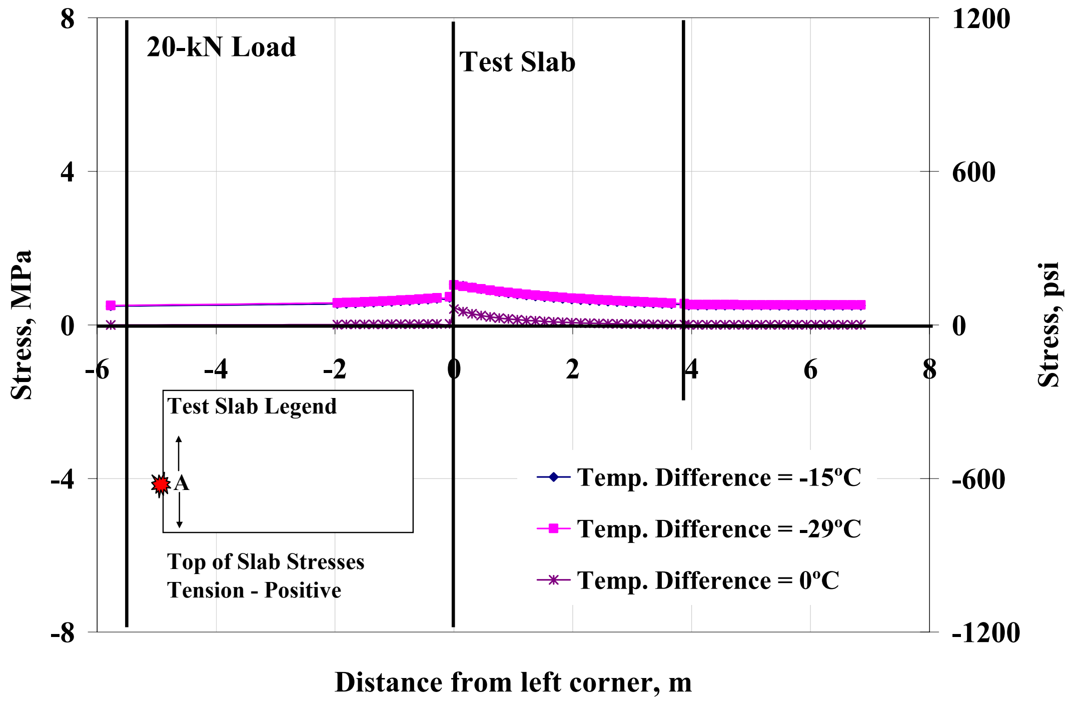

Figure 62. Influence diagram showing effect of 20-kN moving load on transverse stresses at the transverse joint (Section 530FD – 200 mm slab).

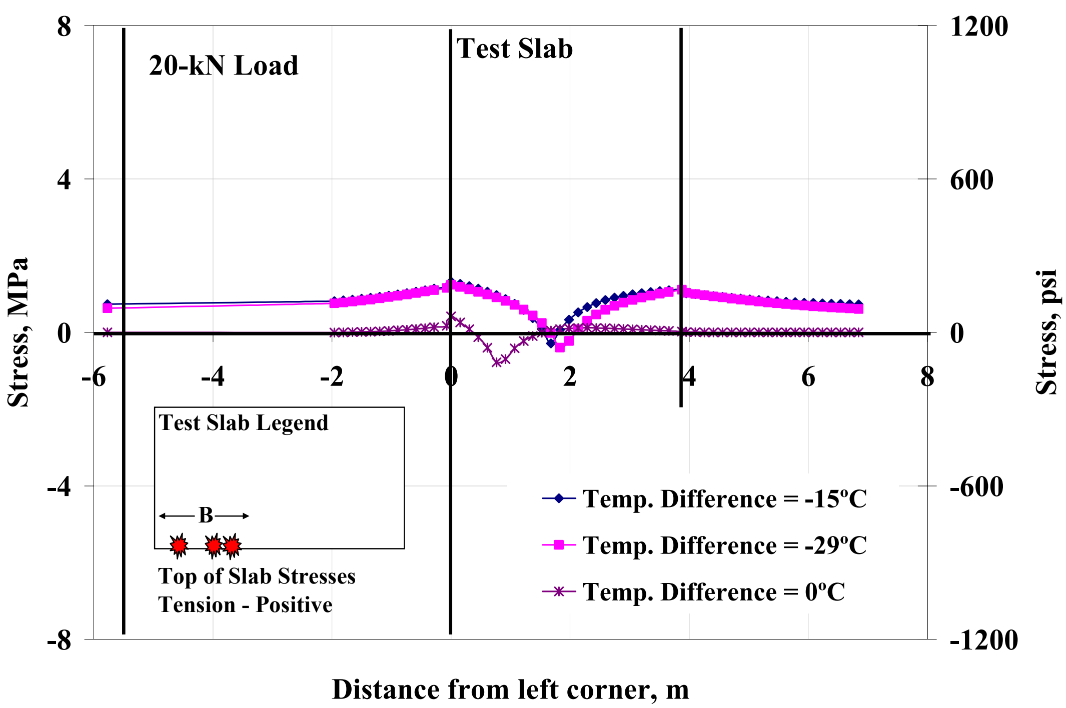

Figure 63. Influence diagram showing effect of 20-kN moving load on longitudinal stresses at the lane-shoulder joint (Section 530FD – 200 mm slab).

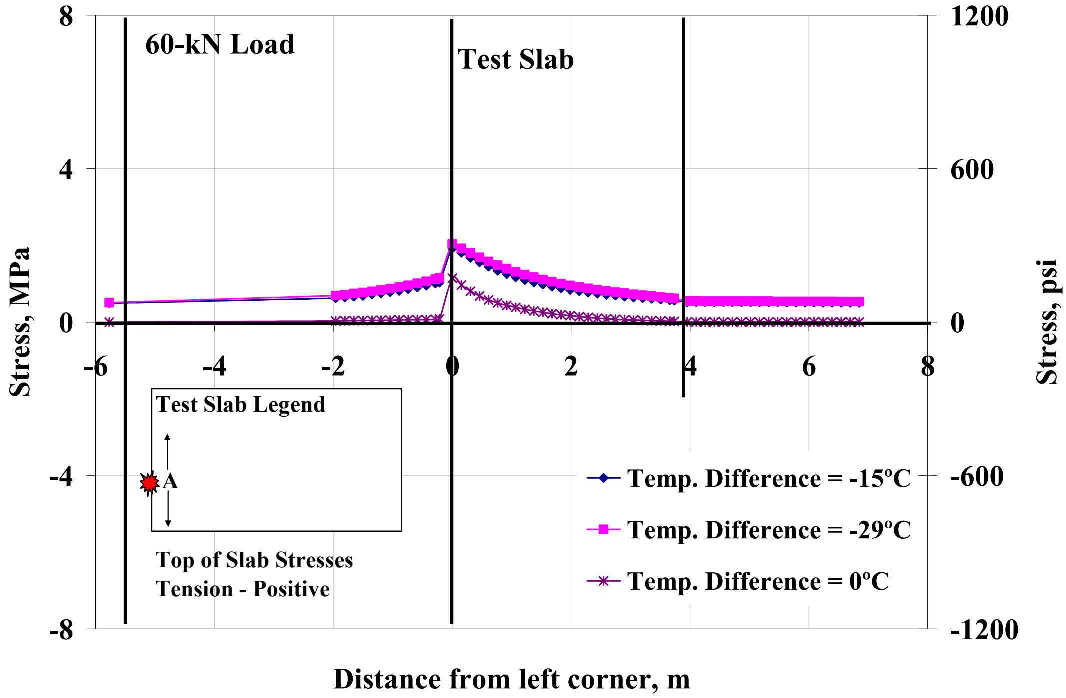

Figure 64. Influence diagram showing effect of 60-kN moving load on transverse stresses at the transverse joint (Section 530FD – 200 mm slab).

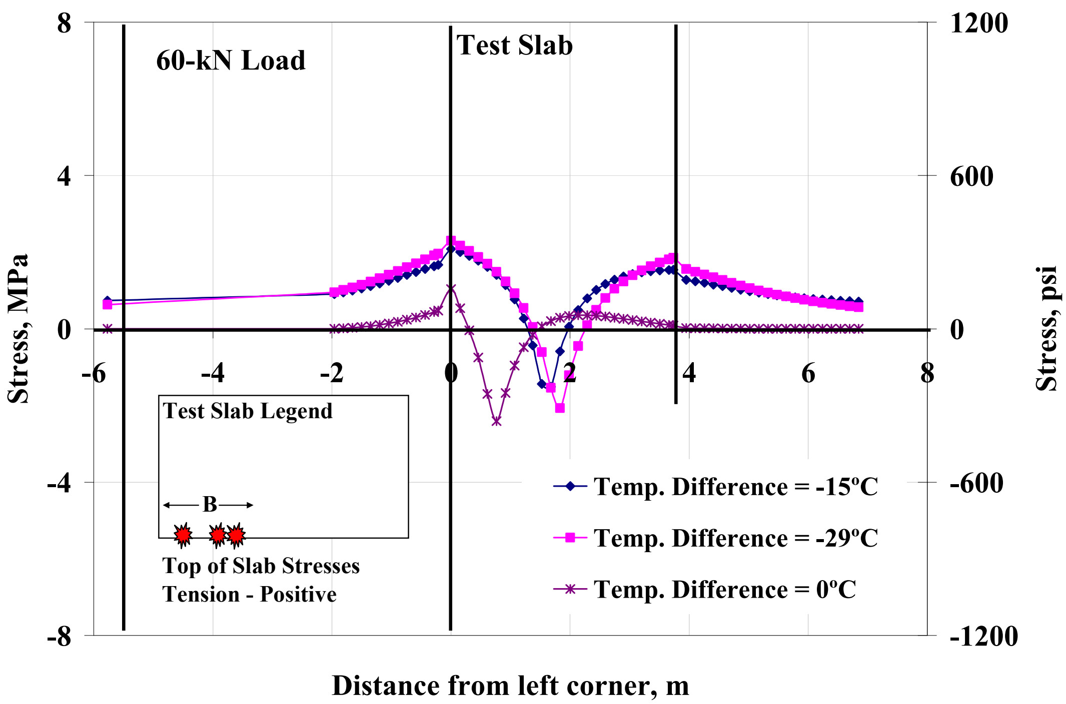

Figure 65. Influence diagram showing effect of 60-kN moving load on longitudinal stresses at the lane-shoulder joint (Section 530FD – 200 mm slab).

Table 10 **Influence Chart Analysis Summary for Slab Edge, Sections 520FD, 524FD, and 530FD**

Section	Load, kN	Temp. Grad., ºC	Slab Edge (B)				
			Peak Tensile Stress, MPa	Minimum Stress, MPa	Unloaded Slab Stress, MPa	Max. Stress Change, MPa	Stress Change Relative to Unloaded Slab, MPa
			P	M	U	P-M	P-U
520FD	35	-23	4.66	-1.89	3.03	6.56	1.63
		-12	2.80	-3.44	0.82	6.24	1.98
		0	1.93	-4.06	0.00	5.99	1.93
	20	-23	4.40	-0.57	3.03	4.96	1.36
		-12	2.23	-1.43	0.82	3.66	1.41
		0	1.23	-2.25	0.00	3.48	1.23
	60	-23	5.00	-4.39	3.03	9.39	1.97
		-12	3.69	-6.16	0.82	9.85	2.87
		0	2.63	-7.16	0.00	9.79	2.63
524FD	35	-29	4.84	0.79	3.48	4.04	1.36
		-15	2.90	-0.42	2.14	3.32	0.76
		0	0.98	-2.34	0.00	3.32	0.98
	20	-29	4.35	1.74	3.48	2.61	0.88
		-15	2.69	0.45	2.14	2.24	0.55
		0	0.62	-1.37	0.00	1.99	0.62
	60	-29	5.32	-0.71	3.48	6.03	1.84
		-15	3.11	-1.46	2.14	4.58	0.97
		0	1.47	-3.71	0.00	5.18	1.47
530FD	35	-29	1.67	-1.16	0.63	2.84	1.04
		-15	1.69	-0.87	0.74	2.56	0.96
		0	0.69	-1.47	0.00	2.16	0.69
	20	-29	1.24	-0.40	0.63	1.64	0.61
		-15	1.32	-0.29	0.74	1.61	0.59
		0	0.42	-0.78	0.00	1.20	0.42
	60	-29	2.30	-2.07	0.63	4.37	1.67
		-15	2.08	-1.52	0.74	3.60	1.35
		0	1.04	-2.41	0.00	3.44	1.04

Table 11 Influence Chart Analysis Summary for Transverse Joint at Sections 520FD, 524FD, and 530FD

Section	Load, kN	Temp. Grad., ºC	Transverse Joint (A)				
			Peak Tensile Stress, MPa	Minimum Stress, MPa	Unloaded Slab Stress, MPa	Max. Stress Change, MPa	Stress Change Relative to Unloaded Slab, MPa
			P	M	U	P-M	P-U
520FD	35	-23	4.04	1.30	1.30	2.74	2.74
		-12	3.02	0.80	0.80	2.22	2.22
		0	1.73	0.00	0.00	1.73	1.73
	20	-23	3.31	1.30	1.30	2.02	2.02
		-12	2.31	0.80	0.80	1.52	1.52
		0	1.04	0.00	0.00	1.04	1.04
	60	-23	4.72	1.30	1.30	3.43	3.43
		-12	4.01	0.80	0.80	3.21	3.21
		0	2.70	0.00	0.00	2.70	2.70
524FD	35	-29	1.87	0.57	0.58	1.30	1.29
		-15	2.04	0.60	0.60	1.43	1.43
		0	0.97	0.00	0.00	0.97	0.97
	20	-29	1.32	0.57	0.58	0.75	0.74
		-15	1.49	0.60	0.60	0.89	0.89
		0	0.58	0.00	0.00	0.58	0.58
	60	-29	2.69	0.56	0.58	2.12	2.11
		-15	2.53	0.60	0.60	1.93	1.93
		0	1.56	0.00	0.00	1.56	1.56
530FD	35	-29	1.43	0.50	0.50	0.93	0.93
		-15	1.46	0.49	0.49	0.97	0.97
		0	0.70	0.00	0.00	0.70	0.70
	20	-29	1.04	0.50	0.50	0.54	0.54
		-15	1.06	0.49	0.49	0.57	0.57
		0	0.41	0.00	0.00	0.41	0.41
	60	-29	2.04	0.50	0.50	1.53	1.53
		-15	1.92	0.49	0.49	1.43	1.43
		0	1.15	0.00	0.00	1.15	1.15

The Miner's hypothesis allows the summation of fatigue damage from loads of various magnitudes under various conditions. According to Miner's hypothesis, materials should fracture when the fatigue damage equals 1.0. However, observation shows that variability in material properties, environmental conditions, and load sequencing can result in fractures occurring at fatigue damage values at significantly less than or greater than 1.0.

5.6.2 Relationship between Stress-Strength Ratio and Load Repetitions

The stress ratio experienced by a concrete pavement has traditionally been assumed to be linearly related to the log of the number of load applications required to produce fatigue-related failure, where the stress ratio is the ratio of the combined tensile stress experienced by a loaded concrete pavement to the concrete modulus of rupture:

$$SR = \frac{\sigma}{MR} \tag{3}$$

where

SR	=	Stress ratio
σ	=	Total tensile stress due to traffic and curling at slab edge
MR	=	Modulus of rupture

5.6.3 Fatigue Models

Several fatigue curves for concrete beams have been developed using field and lab data that relate the stress ratio to the number of loads to failure. These include:

- Zero-Maintenance Design Fatigue Model (*11-13*)

$$\log N = 17.61 - 17.61 \cdot SR \quad \textbf{(4)}$$

where
N = Number of stress applications to failure for the given stress ratio SR

- Calibrated Mechanistic Design Fatigue Model (*14*)

$$\log N = \left[\frac{-SR^{-5.367}\log(1-P)}{0.0032}\right]^{0.2276} \quad \textbf{(5)}$$

where
P = Cracking probability

- ERES/COE Fatigue Model (*15*)

$$\log N = 2.13 \cdot SR^{-1.2} \quad \textbf{(6)}$$

- PCA Fatigue Model (*16*)

$$\log N = 11.737 - 12.077 \cdot SR \quad \textit{for } SR \geq 0.55 \quad \textbf{(7a)}$$

$$N = \left[\frac{4.2577}{SR - 0.4325}\right]^{3.268} \quad \textit{for } 0.45 < SR < 0.55 \quad \textbf{(7b)}$$

$$N = \textit{unlimited} \quad \textit{for } SR \leq 0.45 \quad \textbf{(7c)}$$

The log of number of allowable load applications for various fatigue models corresponding to damage of 1.0 as a function of stress ratio is shown in Figure 66.

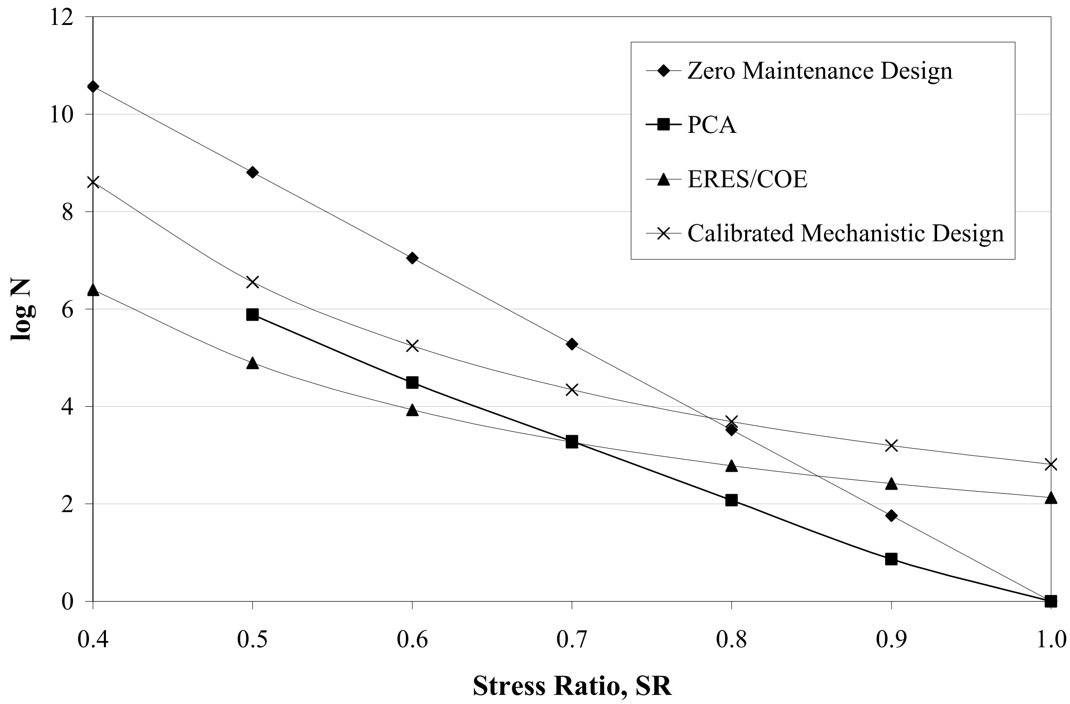

Figure 66. Number of allowable load applications to damage of 1.0 for various fatigue models.

5.7 Cumulative Damage for Sections

ISLAB2000 was used to calculate critical stresses at several locations on the South Tangent test slabs. The calculations were performed for each of the two-hour increments that thermocouple data was collected while loaded with the HVS. The ratio of the calculated stress to the slab strength is the stress ratio corresponding to each time increment. This stress ratio is used to calculate the allowable number of load applications to failure for that time increment using the fatigue models. The ratio of the actual number of HVS applications within the time increment to the calculated allowable number of load applications is the damage for that time increment. The damage for all time increments to failure (appearance of first crack) is summed at each of the stress locations. Cumulative fatigue damage as a function of number of applied loads for Section 523FD using the ERES/COE model is shown in Figure 67. Tables 12 through 14 show the

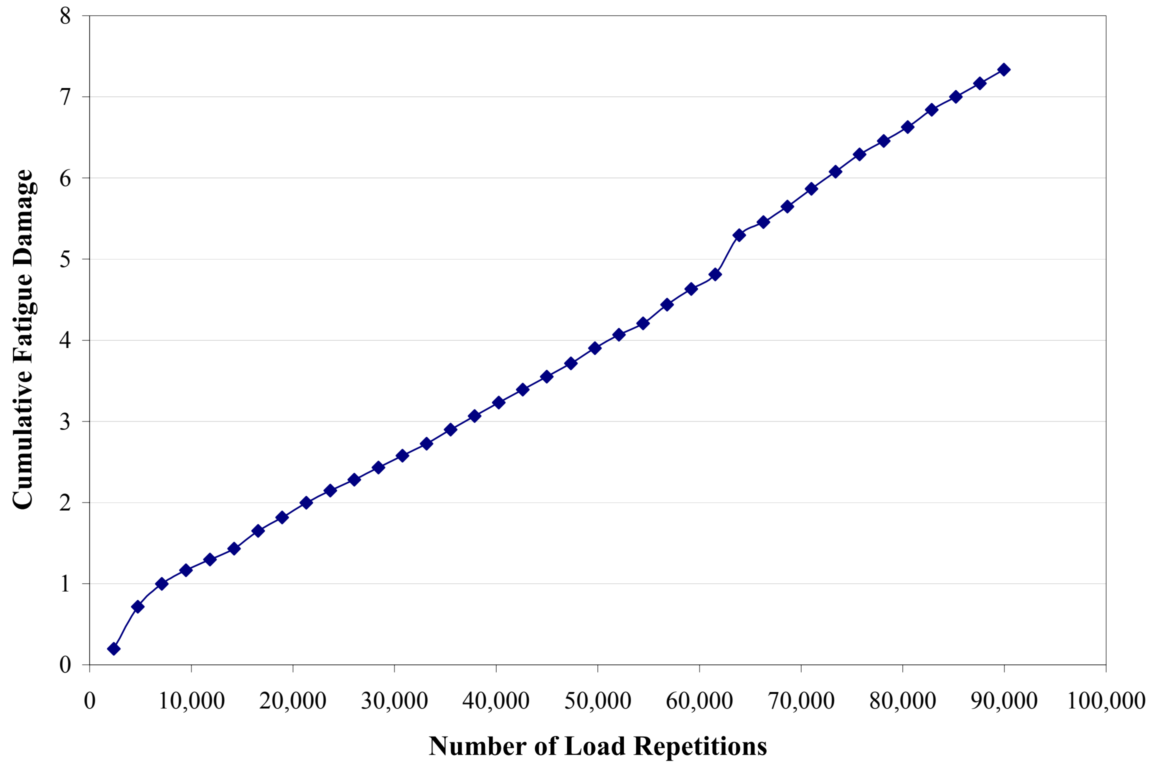

Figure 67. Cumulative fatigue damage calculated at transverse joint critical stress location for Section 523FD (45-kN load).

Table 12 Fatigue Damage to Failure Calculated using "Calibrated Mechanistic Design" Model

Section	Left Shoulder Joint	Left Transverse Joint	Right Shoulder Joint	Right Transverse Joint
520FD	0.384	0.316	0.380	0.323
523FD	18.592	0.324	19.642	0.117
524FD	23.038	0.080	22.263	0.179
525FD	0.008	0.003	0.006	0.006
527FD	0.007	0.033	0.016	0.010
528FD	0.003	0.001	0.004	0.002
529FD	0.062	0.010	0.021	0.038
530FD	0.023	0.001	0.010	0.007
531FD	0.000	0.007	0.002	0.003

Table 13 Fatigue Damage to Failure Calculated using “Zero-Maintenance” Model

Section	Left Shoulder Joint	Left Transverse Joint	Right Shoulder Joint	Right Transverse Joint
520FD	2.77E+00	1.30E+00	2.67E+00	1.40E+00
523FD	4.74E+01	4.80E-03	5.77E+01	1.11E-03
524FD	1.92E+02	6.24E-04	1.68E+02	1.98E-03
525FD	2.37E-04	4.23E-05	1.29E-04	1.50E-04
527FD	4.17E-05	2.04E-04	9.49E-05	5.64E-05
528FD	1.59E-05	4.80E-06	2.07E-05	1.05E-05
529FD	3.49E-04	5.82E-05	1.17E-04	2.08E-04
530FD	1.40E-04	1.74E-05	6.92E-05	5.42E-05
531FD	2.75E-06	4.04E-05	8.81E-06	1.38E-05

Table 14 Fatigue Damage to Failure Calculated using “ERES/COE” Model

Section	Left Shoulder Joint	Left Transverse Joint	Right Shoulder Joint	Right Transverse Joint
520FD	2.630	2.278	2.605	2.313
523FD	148.441	7.335	154.596	3.427
524FD	159.514	2.435	155.528	4.420
525FD	0.130	0.067	0.105	0.111
527FD	0.459	1.403	0.839	0.574
528FD	0.146	0.057	0.179	0.108
529FD	2.935	0.766	1.339	2.040
530FD	1.925	0.253	1.030	0.817
531FD	0.041	0.354	0.113	0.162

calculated fatigue damage at four critical locations on the slab using different fatigue models. For these computations, the peak stresses, P, were used.

A cumulative fatigue damage of 1.0 to failure is not expected for these sections for several reasons including:

- Fatigue model limitations and variability among models.
- Different testing conditions and method for calculating stresses compared to those used to develop the fatigue models.
- Miner’s hypothesis assumptions: linear damage accumulation, homogenous material, limited testing.

- Fatigue models developed for 1.0 to correspond to 50 percent of slabs cracking (given a large section with number of slabs). In the above analysis we are calculating fatigue damage for a single slab.

5.7.1 Concrete Fatigue Models

The differences in the allowable number of load repetitions among the presented fatigue models resulted in significant differences in the calculated cumulative damage. Fatigue models have been developed and calibrated based on several data sources, failure definitions, stress computations, and stress components. The "Calibrated Mechanistic Design" model was developed using Army Corp of Engineers (COE) field aircraft data and American Association of State Highway Officials (AASHO) Road Test data, with failure defined as 50 percent slab cracking. Load and temperature curling stresses were calculated at the slab edge using the finite element program, ILLI-SLAB. The "ERES/COE" model was developed using Corp of Engineers (COE) field aircraft data, with failure defined as 50 percent slab cracking. Load stresses calculated at the slab edge using the influence chart software, H-51, and reduced by a factor of 0.75 to account for load transfer and support conditions. The "Zero-Maintenance" model was develop using concrete beams, with failure defined as complete beam fracture. Load stresses were calculated at the bottom of the beam using the bending beam equation.

Application of a fatigue model without proper calibration can lead to an erroneous conclusion. Further complicating matters are the concrete material size and geometry, which are not considered directly in any of the existing fatigue models but have shown to be factors in the fatigue resistance of concrete.

5.7.2 Miner's Hypothesis Limiting Assumptions

Miner's hypothesis has been used extensively in concrete and asphalt fatigue analysis to account for variable stress states over time. Its ease of application in pavement design has prolonged its life. The main limitation of log N versus SR curves coupled with Miner's hypothesis lies in a phenomenological explanation of fatigue failure of concrete through the stress ratio. The stress ratio approach assumes the stress state in the concrete is constant over the entire concrete fatigue life, which disregards incremental damage or more accurately, crack propagation. This is not a valid assumption, since the previous load cycles damage the concrete, which in turn increases the subsequent stress states in the concrete material. This is why Miner's hypothesis is not sustainable and should not be expected to provide an intrinsic explanation for concrete fatigue failure. Furthermore, factors such as material homogeneity, endurance limit, variable load amplitude, loading rates and rest periods, stress history, and stress reversal are known to affect the fatigue life of concrete and yet cannot be accurately accounted for in a stress ratio / Miner's hypothesis approach.

Another deficiency of using Miner's hypothesis with fatigue damage models is that for new pavements, an initial damage of zero is assumed. Weak zones in the concrete resulting from factors such as drying shrinkage, poor mix characteristics, etc., are not considered. Although the test slabs did not have visual cracks prior to fatigue testing, several of the longer slabs on the test strip cracked prior to any load application.

5.8 Critical Stress Location

Table 15 shows the location of the critical peak stresses and the locations of the field observed cracks on the South Tangent sections. In the tables, longitudinal crack distances are measured in the transverse direction from the slab corner, transverse crack distances are

Table 15 Critical Stress Location and Actual Crack Location for South Tangent Test Sections

Section	Critical Stress Distance (m)	Observed Crack	Observed Crack Distance
520FD	1.0	Longitudinal	1.1
523FD	1.3, 2.0	Corner	1.6, 2.0
524FD	1.2, 2.2	Corner	1.6, 2.1
525FD	1.3, 1.4	Corner	1.7, 1.7
527FD	1.4	Longitudinal	1.5
528FD	1.5	Transverse	2.0
529FD	1.3, 1.5	Corner	1.7, 2.0
530FD	1.3, 1.4	Corner	1.4, 1.3
531FD	1.4, 1.4	Corner	1.7, 1.5

measured in the longitudinal direction from the nearest slab corner. Both longitudinal and transverse distances from the nearest slab corner are measured for corner breaks. As can be seen from the tables, the locations of the critical peak stresses calculated using ISLAB2000 correspond very well with the locations of the observed cracks. Note that the locations of the critical peak stresses are also typically the locations of the critical stress difference (peak loaded slab – unloaded slab). A plot of the calculated critical distance (location of peak stress) versus the actual crack location (on lane-shoulder joint and transverse joint) is shown in Figure 68. The plot suggests that although Miner's approach and cumulative damage using existing fatigue models cannot be used to predict the timing or number of load repetitions corresponding to slab cracking, it is possible to predict the location of the crack based on rolling wheel analysis and slab stresses.

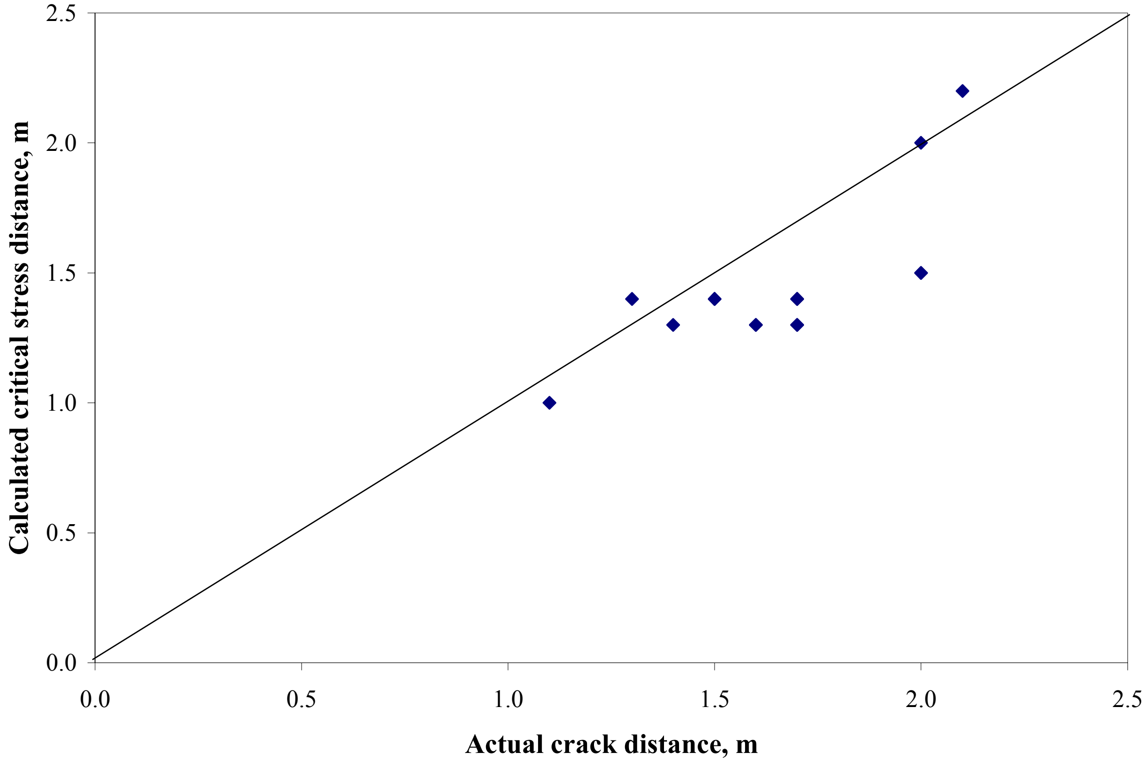

Figure 68. Plot of calculated critical stress location versus actual crack location measured from slab corner for South Tangent test sections.

6.0 CONCLUSIONS

The results of a preliminary analysis of effective built-in temperature difference and slab cracking at the South Tangent sections tested at Palmdale, California using the HVS is included in this report. A detailed analysis of the South Tangent sections will be performed again following the analysis of the North Tangent sections. Because the North Tangent has significantly more information and also includes sections with different designs (i.e., dowels, widened lane, tied shoulders), a better understanding of the cracking behavior of concrete pavements, particularly FSHCC slabs under the influence of an HVS load is expected after the North Tangent analysis.

As part of the South Tangent analysis, a preliminary investigation of the effective linear built-in temperature distribution due to a combination of construction curling and moisture warping was performed. The analysis showed that the effective linear built-in temperature differences of the FSHCC slabs are very high (particularly due to the large amount of surface moisture-related shrinkage) and can be of the order of 25-40ºC (45-70ºF). A detailed analysis of the North Tangent sections is required to confirm this result. This effective built-in temperature distribution can be highly nonlinear and can be approximated by a bilinear distribution. The bilinearity of the temperature distribution does not affect the slab deflections but significantly affects slab stresses.

A rolling wheel analysis in which the stress state of the slab under the influence of a moving wheel load was performed using a finite element program. The results of the rolling wheel analysis were inconclusive with regards to the stresses to be used (peak loaded slab stress, maximum loaded slab stress change, difference of peak loaded slab stress and unloaded slab stress). A primary reason for this is the fact that the built-in temperature distribution can be highly nonlinear and can considerably affect slab stresses. Following the analysis of the North

Tangent sections, the South Tangent sections will be reanalyzed using various bilinear temperature distributions. It is expected that most of the shrinkage in the slab occurs in the top 100-mm of the slab. This results in an approximately linear temperature distribution for the 100-mm nominal thickness slabs and a bilinear distribution for the thicker 150-mm and 200-mm nominal thickness slabs. Using such a distribution, the stress states are expected to be significantly different from those presented in this report. Such an analysis is expected to provide greater insight with regards to the stresses to be used in damage computations.

The results of the damage accumulation analysis shows that although it is possible to predict the location of the crack based on rolling wheel analysis and slab stresses, Miner's approach using current fatigue transfer functions cannot be used to predict the timing or number of load repetitions corresponding to slab cracking. The fatigue transfer functions need to be modified in order to be used in the analysis of the Palmdale slabs. This procedure will be developed for the North Tangent sections and will be calibrated and validated using the South Tangent data.

In addition, it is unclear as to what value of stress (peak loaded slab stress, maximum loaded slab stress change, difference of peak loaded slab stress and unloaded slab stress) and even what value of strength (full strength, reduced strength, increased strength) should be used in the analysis. One reason for this is that although cracks/microcracks in a slab originate at individual points, in order for the crack to be visible during a visual survey, it has to propagate along the length and the width of the slab. Thus the location of critical stress is constantly changing and moving as the crack propagates through the slab.

7.0 FUTURE WORK: NORTH TANGENT DATA ANALYSIS

Based on the South Tangent data analysis the following tasks will be performed on the North Tangent sections:

1. Develop a procedure to estimate built-in curl in concrete slabs.
2. Examine the influence of concrete pavement design features (dowel bars, widen lanes, concrete shoulders, slab thickness) on built-in curl.
3. Assess current procedures for calculating damage and predicting slab cracking.
4. Factor in the effects of nonlinearity of temperature and moisture gradients in the slab on damage and slab cracking.
5. Identify stress components affecting slab failure.
6. Account for shrinkage cracking and non-zero initial damage to the test slabs due to early age stresses and develop correction factors to modify stresses using fracture mechanics principles to model slab cracking.

Following the development of the procedure using the North Tangent data, the South Tangent sections will be reanalyzed and incorporated into a complete cracking model for the Palmdale slabs.

8.0 REFERENCES

1. CAL/APT Contract Team. *Test Plan for CAL/APT Goal LLPRS – Rigid Phase III.* California Department of Transportation. 1998.

2. Rao, S. and J. Roesler. *Analysis and Estimation of Effective Built-In Temperature Difference for North Tangent Slabs: Data analysis from the Palmdale, California Rigid Pavement Test Site.* Draft report prepared for the California Department of Transportation. Pavement Research Center, Institute of Transportation Studies, University of California Berkeley and University of California Davis. 2004.

3. Darter, M. I. *Design of Zero-Maintenance Plain Jointed Concrete Pavement, Volume I: Development of Design Procedure.* FHWA-RD-77-111. Federal Highway Administration. Washington, DC. 1977.

4. Darter, M. I. 1988. *A Comparison between Corps of Engineers and ERES Consultants, Inc. Rigid Pavement Design Procedures.* Technical Report Prepared for the United States Air Force SAC Command. Savoy, IL.

5. Darter, M. I., and E. J. Barenberg. *Zero-Maintenance Pavements: Results of Field Studies on the Performance Requirements and Capabilities of Conventional Pavement Systems.* Federal Highway Administration. FHWA-RD-76-105. Washington, DC. 1976.

6. Darter, M. I., and E. J. Barenberg. *Design of Zero-Maintenance Plain Jointed Concrete Pavement, Volume 1—Development of Design Procedures.* FHWA-RD-77-111. Washington, DC. 1977.

7. du Plessis, L., Bush, D., Jooste, F., Hung, D., Scheffy, C., Roesler, J., Popescu, L., and Harvey, J. *HVS Test Results on Fast-Setting Hydraulic Cement Concrete, Palmdale, California Test Sections, South Tangent.* Report Prepared for California Department of Transportation. Pavement Research Center, Institute of Transportation Studies, University of California Berkeley. 2002.

8. Hall, K.T., Darter, M. I., Hoerner, T. E., and Khazanovich, L. *LTPP Data Analysis—Phase I: Validation of Guidelines for k-Value Selection and Concrete Pavement Performance Prediction*. Technical Report FHWA-RD-96-198. 1997.

9. Heath, A. C., and Roesler, J. R. *Shrinkage and Thermal Cracking of Fast-Setting Hydraulic Cement Concrete Pavements in Palmdale, California.* Report Prepared for California Department of Transportation. Pavement Research Center, Institute of Transportation Studies, University of California Berkeley. 1999.

10. Heath, A.C., Roesler, J.R., and Harvey, J.T. “Quantifying Longitudinal, Corner and Transverse Cracking in Jointed Concrete Pavements.” Paper pre-print 00775, *Journal of the Transportation Research Board*, Washington, D.C., 25 pp. 2002.

11. Hiller, J. E. and Roesler, J. R. "Transverse Joint Analysis for use in Mechanistic-Empirical Design of Rigid Pavements." Paper pre-print 02-2426, *Journal of the Transportation Research Board*, Washington, D.C., 29 pp. 2002.

12. Miner, M. A. "Cumulative Damage in Fatigue." *Transactions, American Society of Mechanical Engineers*. Volume 67. A159-A164. 1945.

13. Packard, R. G. and S. D. Tayabji. "Mechanistic Design of Concrete Pavements to Control Joint Faulting and Subbase Erosion." Paper Presented at the International Seminar on Drainage and Erodability at the Concrete Slab-Subbase-Shoulder Interfaces. Paris, France. 1983.

14. Roesler, J. R., Scheffy, C. W., Ali, A., and Bush, D. *Construction, Instrumentation, and Testing of Fast-Setting Hydraulic Cement Concrete in Palmdale, California.* Report Prepared for California Department of Transportation. Pavement Research Center, Institute of Transportation Studies, University of California Berkeley. 1998.

15. Salsilli, R. A., E. J. Barenberg, and M. I. Darter. "Calibrated Mechanistic Design Procedure to Prevent Transverse Cracking of Jointed Plain Concrete Pavements." *Proceedings of the 5th International Conference on Concrete Pavement Design and Rehabilitation.* Purdue University. West LaFayette, IN. 1993.

16. Ullidtz, P. *ELCON: Evaluation of Layer Moduli and Overlay Design (ELMOD for Concrete)*. Dynatest Engineering A/S, Denmark. 1987.